HIGH SPEED VISCOUS
PLANE COUETTE-POISEUILLE FLOW STABILITY

A THESIS SUBMITTED TO
THE GRADUATE SCHOOL OF NATURAL AND APPLIED SCIENCES
OF
THE MIDDLE EAST TECHNICAL UNIVERSITY

BY

ALİ ASLAN EBRİNÇ

IN PARTIAL FULFILLMENT OF THE REQUIREMENTS FOR THE DEGREE OF

DOCTOR OF PHILOSOPHY

IN

THE DEPARTMENT OF MECHANICAL ENGINEERING
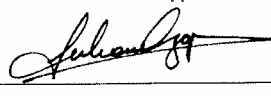

FEBRUARY 2004

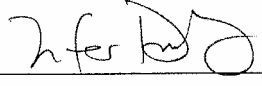Approval of the Graduate School of Natural and Applied Sciences

_____

Prof. Dr.Canan Özgen
Director

I certify that this thesis satisfies all the requirements as a thesis for the degree of Doctor of Philosophy.

_____

Prof. Dr.Kemal İder
Head of Department

This is to certify that we have read this thesis and that in our opinion it is fully adequate, in scope and quality, as a thesis for the degree of Doctor of Philosophy.

_____
Assoc.Prof.Dr.Serkan Özgen
Co-Supervisor

_____
Prof.Dr.Zafer Dursunkaya
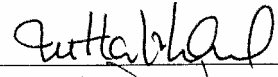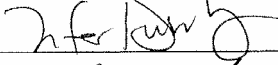Supervisor

Examining Committee Members
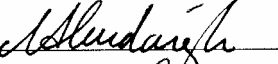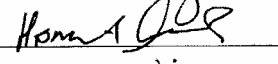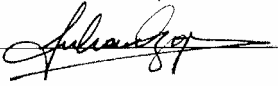
Prof.Dr.Haluk Aksel   _____

Prof.Dr.Zafer Dursunkaya   _____

Prof.Dr.Nafiz Alemdaroğlu   _____

Prof.Dr.Haşmet Türkoğlu   _____

Assoc.Prof.Dr.Serkan Özgen   _____

ABSTRACT

HIGH SPEED-VISCOUS
PLANE COUETTE-POISEUILLE FLOW STABILITY

Ebrinç, Ali Aslan

Ph.D., Department of Mechanical Engineering

Supervisor: Prof. Dr. Zafer Dursunkaya

Co-Supervisor: Assoc. Prof. Dr. Serkan Özgen

February 2004, 125 pages

The linear stability of high speed-viscous plane Couette and Couette-Poiseuille flows are investigated numerically. The conservation equations along with Sutherland's viscosity law are studied using a second-order finite difference scheme. The basic velocity and temperature distributions are perturbed by a small-amplitude normal-mode disturbance. The small-amplitude disturbance equations are solved numerically using a global method using QZ algorithm to find all the eigenvalues at finite Reynolds numbers, and the incompressible limit of these equations is investigated for Couette-Poiseuille flow. It is found that the instabilities occur, although the corresponding growth rates are often small. Two families of wave modes, Mode I (odd modes) and Mode II (even modes), were found to be unstable at finite Reynolds numbers, where Mode II is the dominant instability among the unstable modes for plane Couette flow. The most unstable mode for plane Couette – Poiseuille flow is Mode 0, which is not a member of the even modes. Both even and odd modes are acoustic modes created by acoustic reflections between a wall and a relative sonic

line. The necessary condition for the existence of such acoustic wave modes is that there is a region of locally supersonic mean flow relative to the phase speed of the instability wave. The effects of viscosity and compressibility are also investigated and shown to have a stabilizing role in all cases studied.

Couette-Poiseuille flow stability is investigated in case of a choked channel flow, where the maximum velocity in the channel corresponds to sonic velocity. Neutral stability contours were obtained for this flow as a function of the wave number, Reynolds number and the upper wall Mach number. The critical Reynolds number is found as 5718.338 for an upper wall Mach number of 0.0001, corresponding to the fully Poiseuille case.

Keywords: linear stability, eigenvalue, high speed-viscous flow, Couette flow, Poiseuille flow, QZ algorithm, critical Reynolds number

ÖZ

YÜKSEK HIZLI – VİSKOZ AKIŞKANIN
DÜZLEMSEL COUETTE-POISEUILLE AKIŞTAKİ KARARLILIĞI

Ebrinç, Ali Aslan

Doktora, Makina Mühendisliği Bölümü

Tez Yöneticisi: Prof. Dr.Zafer Dursunkaya

Ortak Tez Yöneticisi: Assoc. Prof.Dr. Serkan Özgen

Şubat 2004, 125 sayfa

Yüksek hızlı ve viskoz akışkanın doğrusal bir düzlemde Couette ve Couette – Poiseuille akış modellerindeki kararlılığı sayısal olarak incelenmiştir. Problem, ideal gaz denklemi ve Sutherland viskozite kanunu da kullanılarak ikinci dereceden sayısal denklemler halinde çözülmüştür.

Temel hız ve sıcaklık dağılımını kapsayan denklemler ufak genlikler kullanılarak normal mod metodu kapsamında uyarılmıştır. Ufak genlikli uyarılmış denklemler, tüm öz değerleri bulmak için QZ algoritması kullanılarak sonlu Reynolds sayılarında sayısal olarak çözülmüş ve bu denklemler yüksek hızlı Couette-Poiseuille akışı için incelenmiştir. Kararsızlıklar uyarılma genliğinin küçük olması durumunda da etkilerini sürdürmektedir. Kararsızlık modları, Mod I ve Mod II olarak iki ana gruba ayrılarak, sonlu Reynolds sayılarında da varlıklarını korumaktadırlar. Mod II, Couette akış için en kararsız olan moddur. Couette – Poiseuille akışta en kararsız Mod 0 olup, Couette akıştaki çift modlar sınıfından değildir. Her iki kararsızlık

modu, kanal içindeki gaz akış hızının dalga hızına göre sesten daha hızlı olduğu durumlarda; kanal içindeki gazın duvar ve göreceli ses çizgisi arasındaki akustik yansımalarından meydan gelmektedir. Kararsızlığı istikrarlı ve durağan hale getirmede gazın viskozite ve sıkıştırılabilirliğinin etkisi ayrıca incelenmiştir.

Maksimum akış hızı sonik olacak şekilde kanal içinde Couette – Poiseuille akış incelenmiştir. Nötr kararsızlık eğrileri; dalga sayısı, Reynolds sayısı ve üst duvardaki Mach sayısının fonksiyonu olarak elde edilmiştir. Kritik Reynolds sayısı üst duvar Mach sayısının 0.0001 olduğu tamamıyla gelişmiş Poiseuille akış için 5718.338 olarak hesaplanmıştır.

Anahtar Kelimeler: doğrusal kararlılık, özdeğer, yüksek hızlı – viskoz akış, Coutte akış, Poiseuille akış, QZ algoritması, kritik Reynolds sayısı

To my parents, my wife and daughter, *Melike.*

ACKNOWLEDGEMENTS

TABLE OF CONTENTS

LIST OF TABLES

TABLE

LIST OF FIGURES

FIGURES

LIST OF SYMBOLS

Superscripts

$'$ First order differentiation, $(....)' = \dfrac{d}{dy}$

$''$ Second order differentiation, $(....)'' = \dfrac{d^2}{dy^2}$

$*$ Dimensional quantities

$-$ Mean flow quantities

$\sim$ Dimensionless perturbation quantities

$\wedge$ Amplitude of dimensionless perturbation quantities

Subscripts

∞ Dimensional quantities evaluated at upper moving wall

w Dimensional quantities evaluated at lower stationary wall

o Dimensional mean flow terms

cr Critical values

r Recovery (in Chap.2)

r Real part of complex quantities

i Imaginary part of complex quantities

ref Reference

ch Channel

ij Eigenvalue coefficient matrix index

1 At crankcase

2 At combustion chamber

Greek Symbols

α Wave number in streamwise direction, $(\alpha = \alpha_r + i\alpha_i)$

β Wave number in spanwise direction, $(\beta = \beta_r + i\beta_i)$

Ψ	Generalized eigenvalue problem eigenvector
ρ	Density, (kg/m^3)
μ	Dynamic viscosity, (kg/ms)
ν	Kinematic viscosity, (m^2/s)
k	Thermal conductivity, (W/mK)
λ	Second coefficient of viscosity, $\lambda = -\dfrac{2}{3}\mu$
c	Complex propagation wave velocity for temporal stability, $(c = c_r + ic_i)$
c_r	Dimensionless phase speed
c_i	Dimensionless temporal amplification factor
ϖ	Temporal amplification rate, $\varpi = \alpha(c_r + ic_i)$
σ_i	Temporal growth rate, $\sigma_i = \alpha c_i$
τ	Dimensionless shear stress across the profile
λ	Wavelength (1/m)
δ	Boundary layer thickness (m)
γ	Ratio of specific heats at constant pressure to constant volume, (γ=1.4 for air)
Φ	Viscous heat dissipation
η	Dimensionless channel height in discretized computational domain
ξ	Harmonics of disturbance wave, $\xi = e^{i(\alpha x + \beta z - \alpha ct)}$

Dimensionless Groups

Re	Reynolds number, $\mathrm{Re} = \rho_\infty^* U_\infty^* h^* / \mu_\infty^*$
l_j	Viscosity group, $l_j = j + \dfrac{\lambda}{\mu}$ j = 0,1,2,3,....
M_w	Upper wall Mach number , $M_w = U_\infty^* / \sqrt{\gamma R T_\infty^*}$
Pr	Prandtl number, $\mathrm{Pr} = \dfrac{\mu_\infty^* c_p^*}{k_\infty^*}$

Alphanumeric Symbols

A	Piston ring gap flow cross-sectional area (m^2)

A, B, C	Coefficient matrices of eigenvalue problem
a_{sound}	Speed of sound at upper wall reference temperature (m/s)
C	Dimensionless constant for Sutherland's viscosity law, $C = \dfrac{S}{T_\infty^*}$
c_p	Specific heat constant at constant pressure, (J/kgK)
d	Equal step size of discretized channel height in RK formulation
g	Gravitational acceleration, ($g = 9.81 \text{ m/s}^2$)
h	Dimensional channel height, (m)
L	Piston ring gap length (m)
$\dot{m}$	Mean mass flow rate in the channel, (kg/s)
N	Node number in computational domain
p	Pressure, (Pa)
P	Pressure, (Pa), (in Ch 5)
q, Q	Velocity, temperature and pressure in linear stability analysis
R	Universal gas constant (R = 287 J/kgK for air)
r	Recovery factor, $r = \dfrac{T_w}{Tr}$
S	Dimensional constant for Sutherland's viscosity law, ($S = 110$ K)
T	Temperature , (K)
t	Time scale, (s)
u	Streamwise velocity component, (m/s)
U	Streamwise velocity component, (m/s), (in Ch. 2)
v	Velocity component normal to flow direction, (m/s)
V_{piston}	Piston speed (m/s)
w	Spanwise velocity component, (m/s)
W	Piston ring gap width (m)
x	Streamwise direction
y	Wall normal to flow direction
z	Spanwise direction

CHAPTER 1

INTRODUCTION

The subject of solving the emission problem has been under investigation over the past several years due to its adverse effect on environmental pollution. The loss of engine oil through the piston-cylinder assembly is a contributor to unburned and burned hydrocarbon emissions. With the implementation of stringent emissions standards, the hydrocarbon emissions due to fuels have radically decreased, paving the way for the engine oil to become a significant contributor to emissions. In an internal combustion engine (ICE), the processes leading to the formation of pollutants are complex and therefore experimental techniques are of widespread use in engine development. The oil flow through the piston-cylinder system has numerous flow passages and local volumes where engine oil can flow through and accumulate. Combustion gases also flow through the same passages and volumes resulting in a complex two-phase flow phenomenon. Due to this nature of the gas-oil flow and the difficulty of the testing and viewing the oil accumulation before and after the piston rings, experimental methods have been used in understanding the gross effects of design parameters on oil loss and developing engines with less oil consumption.

Engine oil is also a strong contributor to particulate formation in diesel engines. In addition, it influences the unburned hydrocarbon emissions of spark ignition engines because of the absorption/de-sorption phenomenon between the unburned fuel and the lubricating oil films. The mechanism of oil consumption in the ICE is complex and so far details have not been thoroughly understood.

In the study of engine oil loss, two sequential stages are defined; the oil rising and oil disappearing. Oil rising is used to define the ensemble of mechanisms that promote the transport of oil into the combustion chamber, whereas oil disappearing is related to phenomena that transform the oil into products carried out by the flow of exhaust gas, such as evaporation and combustion.
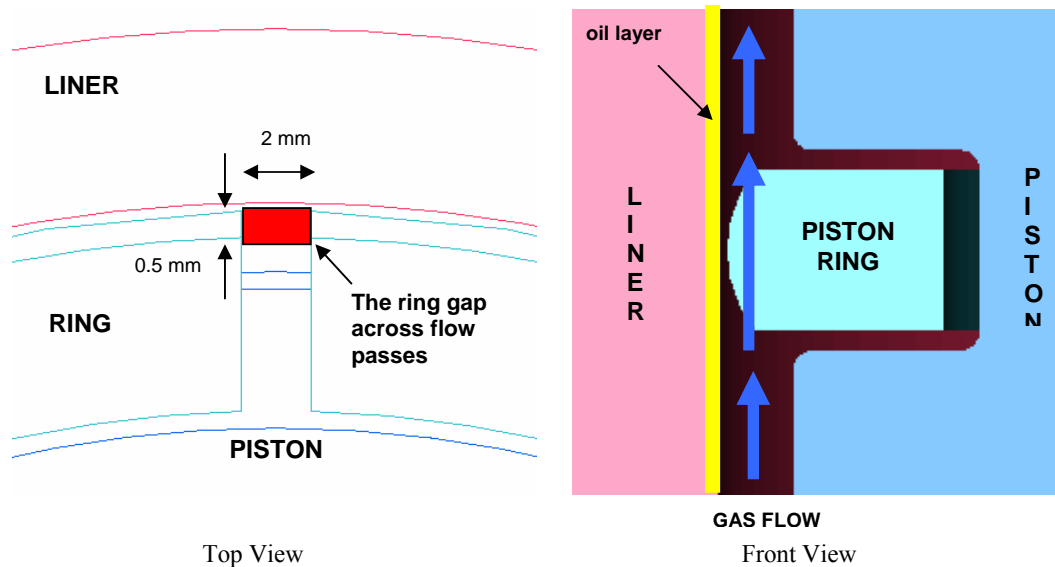
Figure 1.1. Piston ring end gap crosssection and geometry through the flow pass

There are three perceived paths for oil flow through the rings:

1. The oil flow as oil film between the piston ring and the cylinder liner
2. The oil flow through the ring end gaps
3. The oil flow through the ring groove

Geometry and dimension of the ring end gap through which engine oil flow occurs is shown in Figure 1.1. The driving forces that are generally considered responsible of flows are: The pressure difference between each ring, the inertia forces, and the transport of oil as fog or vapor in the gas stream. Most important mechanisms that causes the oil to rise in the combustion chamber are the flow between the liner and

ring and the transport of oil in the gas stream as vapor or fog. The mechanisms and the location of entrainment of oil to form a mist are currently unknown and no effective mathematical description of this phenomenon has so far been suggested.

Film coolers, falling film absorption towers, condensers, transportation of liquid vapor mixtures, boundary layers on aircraft wings, turbine blades and walls of a channel and pipe are examples of processes involving such two-phase flow problems. The same problem exists in the flow of hot combustion gases over the thin oil layer between the ring openings or gaps on the piston in ICEs.

If a gas is blown parallel to an oil film, a shearing force will be exerted on the liquid surface and cause the liquid to flow. This phenomenon exists in the flow system composed of the piston-liner volumes and the ring-liner flow passages of an ICE. The oil carried by the gas flow is transported to the combustion chamber of the engine. With increasing gas velocity, the shear force on the liquid film increases. At higher gas speeds, the liquid becomes unstable and surface waves will form. This leads to the removal of oil droplets from the oil film to be dispersed in the gas and carried to the combustion chamber.

The flow of gas and oil through the ring end gap were modeled by Karkaç [1] and the models for liquid entrainment into the gas flow were integrated to predict the oil loss into the gas. Three mechanisms of oil loss due to in cylinder components widely investigated are: 1) oil left on the cylinder surface and mixing with the combustion chamber content, 2) oil mixing with the blowby gases and transportation due to pressure gradient across the rings, 3) oil accumulated by the top compression ring due to the scraping of oil film on the cylinder. Oil backflow due to pressure gradient is the most effective path for oil loss and it was found that the oil film thickness affects the backflow oil consumption in the second and third land volumes in ICEs and the calculated oil loss values were 2-3 times greater than oil consumption encountered in operating engines.

The effect of oil film thickness on oil accumulation in the second land of ICEs has been experimentally studied by İçöz [2]. Backflow of engine oil suspended in combustion gases has a contribution to the oil consumption and hydrocarbon emission when the gas flows through the piston second land back into the combustion chamber. The piston-cylinder model assembled to measure the total oil accumulated in the modeled second land after a single piston stroke and the results compared to oil consumption in operating engines shown the oil accumulation in the second land could be the major contributor to oil consumption.

1.1. Problem Description

Under brake conditions of an engine, the pressure in the intake manifold becomes lower than the crankcase. When these conditions occur, lubricating oil is sucked from the crankcase through the piston clearances and ring gaps into the combustion chamber.
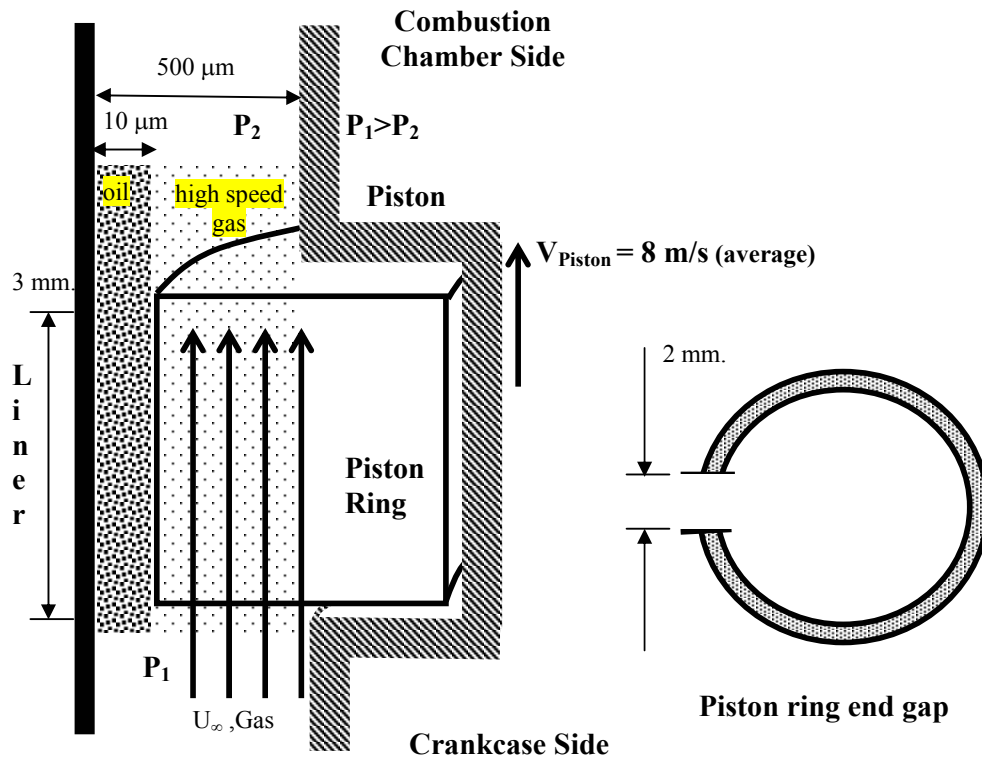
Figure 1.2. Schematic representation of flow across ring gap in dimensions

This oil flow from the sump to the combustion chamber through the piston ring belt causes an increase in oil consumption and an emission of exhaust smoke and oil mist.

The thin layer of oil film and on which gas flows between two parallel plates represents the basic geometry of the problem. To understand the entrainment of oil into the high-speed gas, it is necessary to investigate the stability of the oil and gas interface. The thickness and the velocity of the oil film moving on the stationary plate are small compared to the high-speed gas flow occurring above the oil film and regarding the high viscosity of oil compared to that of air, the oil layer behaves like a solid wall as far as the stability of the gas phase is concerned. Therefore, it is possible to study the stability of the high-speed gas flow only, and interpret the findings to apply to the gas-oil system. Although this approach simplifies the problem, the formulation does not compromise the physics and the omission of the oil layer in the analysis is not expected to have an effect on the magnitude of critical Reynolds number for the combined plane Couette-Poiseuille flow. This approach is justified by Özgen [3] who studied the characteristics of the instability of Newtonian and non-Newtonian fluid-air system for low speed flows and concluded that for the case of air flowing over a thin layer of liquid, there is negligible effect of thin liquid layer on the stability of the two-phase flow.
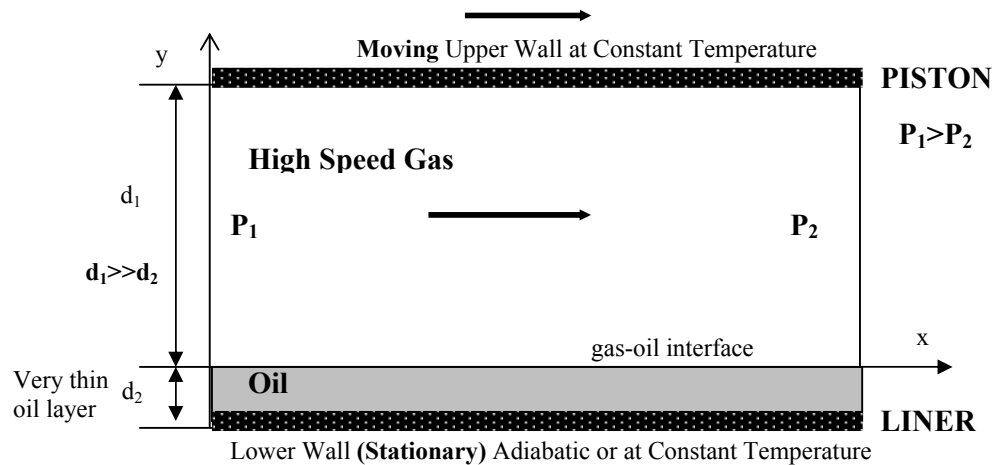
Figure.1.3 Configuration of physical problem in 2D

The fact that, the existence of a thin liquid layer has no contribution to the two-phase flow instability, simplifies and allows us to formulate the problem to a single layer gas flow in computational work. The flow geometry is given in Figure 1.3.

1.2. Basic Approach for Hydrodynamic Stability

Stability can be defined as the quality of being immune to small disturbances. In general, the disturbances need not necessarily be infinitesimally small in magnitude, but the concept of amplification is always implicit.

The stability of laminar flow has been one of the frequently pursued topics in fluid mechanics. The actual flow problem to be solved is highly idealized and flow is assumed to be parallel with velocity and temperature profiles changing in the flow direction and depending only on the distance from the wall and pressure drop in flow direction for Poiseuille flow. This builds up the basic flow concept of the stability calculations. Instability of the flow can occur due to disturbance of equilibrium of the forces acting on the system which are external, viscous and inertial forces. For compressible and viscous flows, viscosity, density, Mach number, wave propagation directions, wall cooling-heating and existence of wall confining the parallel flow have all effect on the stability. The transition to turbulence depends on perturbations due to surface roughness, sound source, the inherent perturbation in the downstream and other effects.

The theoretical investigations are based on the assumption that laminar flows are affected by small disturbances; for pipe flow, these disturbances originate at the inlet whereas for the boundary layer over a flat plate placed in a stream they are due to roughness on the solid surface or irregularities in the external flow. The stability theory is to follow up in time the behavior of such disturbances when they are imposed on the main flow and whether the disturbances increase or die out with time. If the disturbances decay with time, the main flow is considered stable; in contrast, if the disturbances amplify with time the main flow is unstable and the possibility of

transition to turbulence exists. Stability theory predicts the value of the critical Reynolds number, beyond which instability will exist for a prescribed main flow.

For plane incompressible viscous Couette flow, the flow is unconditionally stable at all Reynolds numbers. The viscosity is known to have a stabilizing effect on the flow. In case of the plane Poiseuille flow, the flow is stable at low Reynolds numbers.

The mathematical problem is the determination of the eigenvalues of the stability equation obtained from the governing conservation equations of mass, momentum and energy. It is the aim of the stability analysis to compute the phase velocity, rate of amplification and the wave number of all possible disturbances, in a given flow as a function of the relevant flow properties such as Reynolds and Prandtl numbers.

In natural phenomena, steady state solutions of flow systems have been observed to become unstable as a result of infinitesimal disturbances, which are always present. A common example is the formation of waves on bodies of water due to the action of wind. The common feature of an instability is that infinitesimal velocity or density perturbations are amplified and eventually grow to finite size in time and/or space. The growth of disturbances could be algebraic or exponential in nature. Typical instability analysis assumes an exponential growth, because it is expected that such a behavior would overwhelm any algebraic growth. However, algebraic analyses have been used in problems where exponential models do not match the experimental data. Infinitesimal disturbances are expected to be in the form of noise. The noise is infinitesimal, meaning that the amplitude thereof is small compared to any length scale of the problem.

1.3. Review of Previous Studies

A review of the abundant work published in the area of the waves and instability generated by shear flows shows that there exists many primary approaches for modeling of complex physical processes that occur over the liquid surface.

Behavior of instability waves on the interface has been the subject of many experimental and analytical studies in the past. In general, characteristics of surface instability can be analyzed in the framework of linear analysis.

In the literature, numerous investigators worked on this problem experimentally and numerically. Analysis of the incompressible viscous and/or inviscid stability problem based on the Orr-Sommerfeld equation has been widely presented in the literature. Experimental approaches are used to visualise the phenomena from the physical point of view to compare the numerical studies or to complete the solution.

Lees and Reshotko [4], studied on the stability of the compressible laminar boundary layer to infinitesimal disturbances assuming the two dimensional compressible laminar boundary layers to two dimensional subsonic disturbances and only simplest model of a compressible gas with constant specific heat, constant Prandtl number, viscosity a function of temperature. They concluded that the rate of conversion of energy from the mean flow to the disturbance flow through the action of viscosity in the vicinity of the wall increases with Mach number. Also the amplitude of inviscid pressure fluctuations for Mach number greater than 3 decreases with distance outward from the plate surface. The jump in magnitude of the Reynolds stress in the neighbourhood of the critical layer is greatly reduced. At the Mach number less than about 2, dissipation effects are minor, but extremely important at high Mach numbers. Finally the minimum critical Reynolds number for an insulated flat plate boundary layer decreases with increasing Mach number in the range of 0<M<3.

Lesen, Fox and Zien [5], investigated the inviscid stability of the laminar mixing of two parallel streams of a compressible fluid with respect to 3D wavy disturbances. They considered the Squire's method to decrease the incompressible 3D disturbances to be equivalent to a two dimensional one at a lower Re number. It is sufficient to consider 2D disturbances only. They focused on the influence of the Mach number of the flow and the angle of wave propagation on the stability characteristics of the laminar mixing of two streams of a compressible fluid. They considered the flow with subsonic disturbances due to the reason of supersonic disturbances, which are

often neglected in the stability calculations are less destabilizing then subsonic disturbances.

Brown [6], studied the compressible boundary layers. He pointed out for Mach numbers above 2 and 3 stability equations for compressible flow include a number of terms, involving the components of the mean boundary layer velocity component perpendicular to the surface (flat plate), which are not negligible, but those have been ignored in making parallel flow assumptions. He numerically solved stability equations including those surface perpendicular terms. He included the momentum equations in all three directions in his calculations instead of the usual two and concluded that there is an agreement between theory and experiment for both upper and lower branches of the neutral stability curve for both Mach number 2 and 5. After substitution of the three-dimensional form of perturbation component, in ~~to~~ the equations of motion, reduction to two-dimensional form by the Squire's theorem is accomplished. This results in a systems of eight first order differential equations and the solution is separated into two parts

Yih [7], considered the stability of superposed fluids of different viscosity in plane Couette and Poiseuille flow. The variation of viscosity in a fluid can cause the instability. He considered that both plane Poiseuille and plane Couette flows can be unstable although the Reynolds number is high. He recognised the plane Couette-Poiseuille flow of two superposed layers of fluids of different viscosity between two horizontal plates. He concluded that both plane Couette and Poiseuille flows can cause instability although the Reynolds number is small.

Blumen, Drazin and Billings [8], considered the linear stability of shear layer of an inviscid compressible fluid. It was shown by them that there was instability of two dimensional disturbances at all values of the Mach number, due to second unstable mode. This mode is supersonic, decays with distance from the shear layer and is not governed by the principle of exchange of stabilities. The shear layer is unstable to two-dimensional waves at each value of the Mach number. The occurrence of second mode is associated with a breakdown in the validity of the Mach number. They concluded that if a given flow is unstable to two-dimensional waves at zero

Mach number, it is unstable to three-dimensional waves at each value of the Mach number. A wave nearly perpendicular to the plane of compressible flow is equivalent to a two dimensional incompressible wave because smallness of effective basic velocity.

Blumen [9], studied on the stability of parallel shear flow of an inviscid compressible fluid by a linear analysis. It is shown that a subsonic neutral solution of the stability equation would be found where the basic flow is represented by the hyperbolic tangent velocity profile. Unstable eigenvalues, eigenfunctions and Reynolds stresses are determined by numerical values. He found an analytical neutral stability characteristics for a smoothly varying shear layer of an inviscid perfect gas at uniform temperature. He only considered the subsonic disturbances and instability was shown to exist for 0<M<1, when the Mach number M is based upon half the velocity difference across the shear layer.

Mack [10], described the stability problem for the compressible, viscous (and inviscid) laminar boundary layer. He described the stability problem as dealing with the flow which is parallel with specified velocity and temperature profile, having the only change depend on the distance from the wall. Disturbances are taken travelling in the form as sinusoidal waves. Amplification with respect to time only. Mathematical problem is shaped to determine the eigenvalues of the stability equations at same Reynolds number, such as, the phase velocity, rate of amplification and the wave number of all possible disturbances. Asymptotic method is used to evaluate those theories to approach the stability problem. Solution of the laminar boundary layer equations cover the Mach number range from 0.4 to 5.0. Pressure gradient is taken to be zero to keep the simplicity of ordinary differential equation.

Djordjevic and Redekopp [11], studied the linear stability of inviscid, compressible shear flow. Relative Mach number, $|U_0 - c|$, which is the important parameter for characterizing the disturbance in parallel shear flow is taken as by them. They introduced that for subsonic flows over the entire flow domain stability modes are the modifications of vorticity modes for incompressible limit. They obtained the

specific neutral solutions for both a shear layer. Also unstable solutions are calculated for both streamwise and oblique distributions in the shear layer flow.

Glatzel [12], investigated the structure of normal modes in viscous compressible plane Couette flow. Two different modes of spectrum are defined as being the viscous modes which obtain finite phase velocities by the mechanism of mode pairing and the sonic modes whose phase velocity becomes distorted in the supersonic regime. Both mode pairing of viscous modes and distortion of the phase velocity of sonic modes are caused by the shear. Combined effect of viscosity and compressibility is studied treating the simplest case of plane Couette flow. The perturbation equation is considered to the simple differential equation for the pressure perturbation. Viscosity stabilizes at sufficiently small Reynolds number but for such cases like plane Poiseuille flow it leads to an instability at high Reynolds numbers.

Zhuang, Dimotakis and Kubota [13], investigated the inviscid stability with respect to supersonic disturbances of a spatially growing plane mixing layer inside parallel flow guide walls using linear stability analysis. The shear layer flow considered as inviscid and formed by the same gases in the two streams. The mean flow is treated as parallel. Their purpose was to give a description of how the instability characteristics of the shear layer are affected by the flow guide walls and by the distance between the walls. Concluding that the existence of the walls makes the shear layer more unstable and keeps the maximum amplification rates from reaching an asymptotically small values for supersonic convective Mach numbers, but no such an effect can be seen for subsonic convective Mach numbers. For supersonic convective Mach numbers they found the maximum amplification rates of the shear layers approach an asymptotic value and this maximum amplification rate increased to its maximum value and decreases as the distance between the walls decreases continuously.

Malik [14], compared the various numerical methods for the solution of laminar stability equations for compressible boundary layers. He discussed both the global and the local eigenvalue methods for temporal stability analysis. Global methods are

used to compute all the eigenvalues of the discretised system and in local methods both purification and computation of the associated eigenfunctions take place. The discretization methods that Malik applied are second order finite difference method, second order finite difference method with fourth order accurate two-point compact difference scheme, Chebyshev spectral collocation method and multi-domain spectral collocation method. All these methods belong to the class of methods called boundary value method. He presented the eigenvalues up to Mach number 10, hypersonic range taking the effect of increase of Mach number brings out the deterioration of spectral method due to outward movement of the critical layer. Elimination of this problem is accomplished by using multi-domain spectral collocation method for better accuracy.

Malik [14] concluded up with the compressible analogue of the known incompressible Orr-Sommerfeld equation which is a coupled set of five ordinary differential equations. The set of equations are one second order energy equation, three second order momentum equation and one first order continuity equation. Reduction of those system of second order ordinary differential equation is possible using the approach by Less and Lin (1946). Numerical methods are described that perfect gas equations are applicable. Malik take into account of Sutherland's formula for the viscosity with temperature dependence as $\mu = 2.227 * 10^{-8} \dfrac{T^{1/2}}{1 + 198.6/T}$ lb - sec / ft^2.

Malik used two different methods to solve the compressible linear stability problem as an Initial value theorem and boundary value problem. He described the advantages and disadvantages of both methods which are based upon Chebyshev spectral-tau approach. Initial value problem (IVM) consists of constructing independent initial value problems whose solutions satisfy the eight order set of differential equations and conditions at the free-stream boundary. Main advantage of IVM is the minimal computer memory requirement and their capacity to adjust the integration to local conditions. Disadvantage of this method is the requirement of a good guess of the eigenvalues. For boundary value method,(BVM), the differential equations are reduced to linear algebric equations using either a finite-difference discretization or a spectral representation. Main advantage of this method is their ability to yield eigenvalues when no knowledge of the instability is available for the problem of

interest. Disadvantage of this is the high demand on computational resources both memory and time. As the Mach number increases, the critical layer moves away from the wall towards the edge of the boundary layer. Therefore Chebyshev spectral methods may not be a natural choice for hypersonic boundary layer stability.

Yih [15] investigated wave formation on a thin liquid layer used by de-icing airplane wings by studying the stability of air flow which is compressible and viscous over a liquid coated flat plate at zero angle of incidence. In his physical model, the ratio of the viscosity of the liquid to that of air is very high and the Re number based on the liquid depth and air viscosity is of the order of a few thousand. Yih obtained two formulas for the growth rate and phase velocity of the gravity effect and surface tension as being Froude number, F and S, respectively. Viscosity difference has the dominant effect in Yih's instability model because it induces a jump in the velocity gradient.

Duck, Erlebacher and Hussaini [16], investigated the linear stability of compressible plane Couette flow. Firstly, they treated the basic velocity and temperature distribution perturbation by a small amplitude normal mode disturbance. After disturbance equations they handled at finite Reynolds number those equations are solved numerically and they investigated the inviscid limit of those equations. They included the viscosity to slow the effect of it on calculations and it has stability role in all cases they investigated. Also investigated by them the cases where the wave speed of the disturbances approached the velocity of walls. The effect of imposing radiation type boundary conditions on the upper (moving) wall is investigated to yield the results common to both unbounded and bounded flows. They showed that the details of the mean flow profile have a profound effects on the stability of the flow. They studied the linear inviscid and viscous stability of compressible Couette flow using realistic compressible flow models. The viscosity coefficients are computed by the Sutherlands law with a constant Prandtl number of 0.72. using numerically generated solutions for the basic flow. They calculated the inviscid stability modes of compressible Couette flow. The inviscid stability characteristics of the bounded Couette flow was found to be quite different from that of the unbounded boundary layers. For the viscous instability of compressible Couette

flow, analysed the effects of viscosity on the stability by asymptotic analysis. Viscosity was found to play a stabilising role for the unstable modes. They also obtained the spectra of viscous eigenmodes numerically from the linearized full Navier-Stokes equations for the viscous stability at finite Reynolds numbers. Although the viscous unstable modes were expected to exist at high Reynolds numbers, no evidence of unstable modes was found in theirs numerical solutions.

Hu and Zhong [17] studied the viscous linear stability of supersonic using two global methods to solve the linear stability equation. Flow for a perfect gas is governed by Sutherland viscosity law. Those methods they introduced are a fourth order finite difference method and a spectral collocation method. They found two wave modes to be unstable at finite Reynolds number. Those modes are acoustic modes created by sustained acoustic reflections between a wall and a relative sonic line when the mean flow in the local region is supersonic with respect to the wave velocities. Effects of compressibility, three dimensionality, wall cooling on the two wave families are also studied. For hypersonic bounded flows such as plane Couette flow they expected that the stability properties will be different from those of the unbounded compressible boundary layers because of the combined effects of the upper and lower walls. In addition the effects of viscosity on the stability of compressible Couette flow were examined by comparing the viscous results with the inviscid stability results obtained by Duck et al.[16].

South and Hooper [18], studied on the linear stability of two-fluid plane Poiseuille flow in two dimensions, concentrating on transient growth and its dependence on the viscosity and depth ratio. They concentrated on the hydrodynamic stability of shear flows of two superposed fluids on the behaviour of the interfacial mode. Interfacial mode is due to the viscosity and/or density jump across the interface and the proximity of the boundary walls. The stability equations for two-fluid flows admit an infinite number of discrete eigenvalues and eigenmodes and the interfacial mode is usually the leading eigenmode. The flow consists of two immiscible, incompressible Newtonian fluids of equal density, one on top of the other between two horizontal plates. Surface tension is to be zero.

Özgen, Degrez and Sarma [19], investigated the two fluid flow, in which a gas boundary layer shears a second fluid that is bounded by the wall and the shearing fluid. They solved the eigenvalue problem governing the linear stability of the configuration using an efficient shooting search method. In shooting method, two asymptotic solutions for the eigenfunctions are constructed at the edge of boundary layer and Orr-Sommerfeld number is integrated towards the wall. They categorised the stability modes due to two fluid interface in two modes such as Tollmien-Schlichting (hard) and Yih (soft) modes. They determined the effects of viscosity and density stratifications, thickness of the bounded fluid, gravity, surface tension and non- Newtonian character of lower fluid and concluded that Yih mode is very sensitive to viscosity stratification and for highly viscous liquid layer single layer behaviour is to be seen easily. Results on the parameters can be outlined as surface tension has stabilising effect for short waves for interfacial modes, but they experienced more complex effect for hard mode. Gravity has destabilizing effect for low and moderate values of the density stratification but has stabilizing effect for higher values.

CHAPTER 2

GOVERNING EQUATIONS

2.1. Flow Description and Objectives

The objectives of the present study are to understand the effects of viscosity, temperature, compressibility and density on the stability of high speed parallel shear flows. The flow geometry is sketched in Figure 2.1.
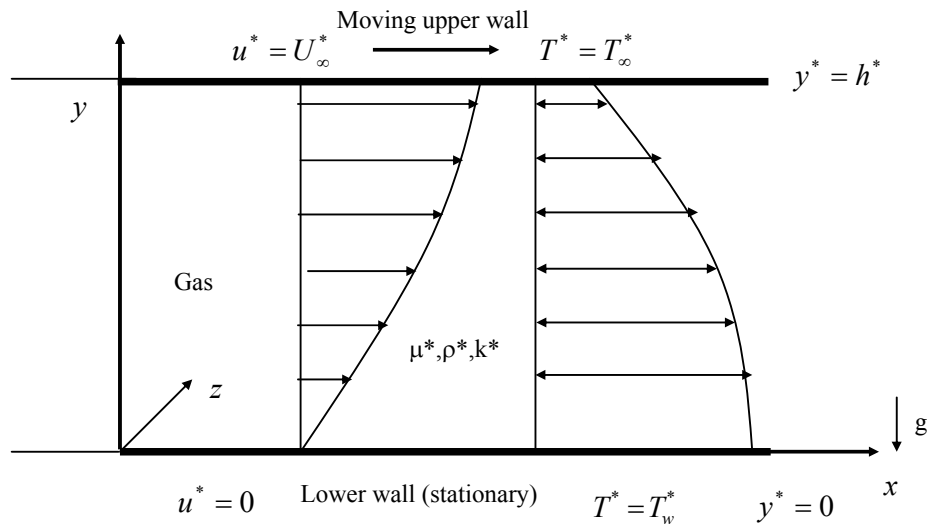
Figure 2.1. Flow geometry for the compressible Couette flow in a channel

Gas flow is considered as viscous and compressible and in the meantime assumed to be parallel and fully developed. Velocity and temperature profiles are functions of vertical distance only. The linearized disturbances are in the form of travelling *sine*

waves whose amplification is with respect to time, not with respect to distance travelled in the flow direction. The mathematical problem is to determine the eigenvalues of the stability equations, *i.e.*, for given boundary layer profiles to compute at some Reynolds number, the phase velocity, rate of amplification and the wave number of all possible disturbances. The stability of a shear layer of an inviscid compressible and viscous incompressible fluid are all classical problems of fluid mechanics, which has attracted the attention of some distinguished scientists of earlier generations. However, the linear stability of compressible flows is considerably less understood than corresponding incompressible flows.

2.2. Governing Equations of Mean Plane Couette Flow

2.2.1. Basic flow velocity, temperature and related profiles

The laminar gas flow assumption across the channel is used and proved in Appendix A for a flow media similar with the slit at piston-ring gap. Also for a gas flow developing in a channel obeying the Poiseuille flow conditions is calculated as fully developed and laminar.

Velocity $u(y)$, temperature $T(y)$, dynamic viscosity $\mu(T)$ and thermal conductivity $k(T)$ of the basic flow are all initially calculated to perform the stability analysis. Flow is assumed to be nearly parallel and in z – direction there is no flow although z – momentum equation is taken into account for stability formulation to have full sets of equation. But at further stability calculations, z – momentum equation was again discarded from the calculations set to save computational time. Eliminating the equation made no difference on the results are seen due to all z – momentum components being either zero or being negligibly small.

For the high speed viscous Couette flow, a solution to the governing equations is sought.

The dimensionless form of the continuity equation is given as

$$\frac{\partial \rho}{\partial t} + \frac{\partial (\rho u)}{\partial x} + \frac{\partial (\rho v)}{\partial y} = 0 . \tag{2.1}$$

Here we assume that the appropriate dimensional timescale of $O(h^{*}/U_{\infty}^{*})$ is used to nondimensionalize the time.

The momentum equations are then written in dimensionless form by nondimensionalizing the pressure by $\rho_{\infty}^{*} R T_{\infty}^{*}$ instead of the conventional $\rho_{\infty}^{*} U_{\infty}^{*2}$ for the incompressible flow, Duck [16].

$$\rho\left[\frac{\partial u}{\partial t} + u\frac{\partial u}{\partial x} + v\frac{\partial u}{\partial y}\right] = -\frac{1}{\gamma M_{w}^{2}}\frac{\partial P}{\partial x} + \frac{1}{\mathrm{Re}}\left\{\frac{\partial}{\partial x}\left[2\mu\frac{\partial u}{\partial x} + \lambda \nabla . u\right] + \frac{\partial}{\partial y}\left[\mu(\frac{\partial u}{\partial y} + \frac{\partial v}{\partial x})\right]\right\},$$

$$\tag{2.2}$$

$$\rho\left[\frac{\partial v}{\partial t} + u\frac{\partial v}{\partial x} + v\frac{\partial v}{\partial y}\right] = -\frac{1}{\gamma M_{w}^{2}}\frac{\partial P}{\partial y} + \frac{1}{\mathrm{Re}}\left\{\frac{\partial}{\partial y}\left[2\mu\frac{\partial v}{\partial y} + \lambda \nabla . u\right] + \frac{\partial}{\partial x}\left[\mu(\frac{\partial u}{\partial y} + \frac{\partial v}{\partial x})\right]\right\}$$

$$\tag{2.3}$$

The dimensionless form of energy equation is:

$$\begin{aligned}
&\rho\left[\frac{\partial T}{\partial t} + u\frac{\partial T}{\partial x} + v\frac{\partial T}{\partial y}\right] - (\frac{\gamma-1}{\gamma})\left[\frac{\partial P}{\partial t} + u\frac{\partial P}{\partial x} + v\frac{\partial P}{\partial y}\right] \\
&= \frac{1}{\mathrm{Re}}\left\{\frac{\partial}{\partial y}\left[\frac{\mu}{\mathrm{Pr}}\frac{\partial T}{\partial y}\right] + \frac{\partial}{\partial x}\left[\frac{\mu}{\mathrm{Pr}}(\frac{\partial T}{\partial x})\right]\right\} \\
&+ \frac{2\mu(\gamma-1)M_{w}^{2}}{\mathrm{Re}}\left[(\frac{\partial u}{\partial x})^{2} + (\frac{\partial v}{\partial y})^{2} + \frac{1}{2}(\frac{\partial u}{\partial y} + \frac{\partial v}{\partial x})^{2} + \frac{\lambda}{2\mu}(\frac{\partial u}{\partial x} + \frac{\partial v}{\partial y})^{2}\right]
\end{aligned} \tag{2.4}$$

Viscosity is a function of the temperature and obeys the Sutherland's viscosity law.

The continuity equation can be used to show that the velocity in y – direction is zero. Then the mean flow only function of y, $i.e.$,

$$u = U_o(y) \qquad T = T_o(y) \qquad \mu = \mu_o(y) \qquad k = k_o(y).$$ (2.5)

After simplification of Equations (2.2) and (2.4), one can get the x – momentum and energy equations in dimensionless form as

$$\frac{\partial}{\partial y}(\mu_o \frac{\partial U_o}{\partial y}) = 0,$$ (2.6)

$$\frac{\partial}{\partial y}\left[\frac{\mu_o}{\Pr}\frac{\partial T_o}{\partial y}\right] + (\gamma - 1)M_w^2\mu_o(\frac{\partial U_o}{\partial y})^2 = 0$$ (2.7)

and the boundary conditions for the solution of Equations (2.6) and (2.7) are

$$U_o(0) = 0 \qquad U_o(1) = 1$$ (2.8)

$$T_o(0) = T_w \qquad T_o(1) = 1$$ (2.9)

It follows from Equation (2.6) that the shear stress, τ, is constant through the profile, $i.e.$,

$$\tau = \mu_o \frac{\partial U_o}{\partial y} = \text{constant.}$$ (2.10)

The energy equation may then be written in the form

$$\frac{\partial}{\partial y}\left[\frac{\mu_o}{\Pr}\frac{\partial T_o}{\partial y} + (\gamma - 1)M_w^2\tau(\frac{\partial U_o}{\partial y})\right] = 0,$$ (2.11)

Integrating once and rearranging the terms

19

$$\frac{\partial T_o}{\partial y} + \frac{Pr}{\mu_o}(\gamma - 1)M_w^2 \tau(\frac{\partial U_o}{\partial y}) = 0 \qquad (2.12)$$

or $\qquad \frac{\partial T_o}{\partial y} + \frac{Pr}{\mu_o}(\gamma - 1)M_w^2(\mu_o \frac{\partial U_o}{\partial y})\frac{\partial U_o}{\partial y} = 0.$ $\qquad (2.13)$

Cancelling viscous terms and integrating once more

$$T_o + Pr(\gamma - 1)M_w^2 \frac{U_o^2}{2} + C = 0. \qquad (2.14)$$

is obtained.

After the application of boundary conditions to above relation, one can get

$$T_w = 1 + \frac{Pr}{2}(\gamma - 1)M_w^2, \qquad (2.15)$$

$$r = \frac{T_w}{T_r} \qquad (2.16)$$

In this study, r is taken as unity giving out the lower wall temperature is equal to the lower wall recovery temperature. If the effect of lower wall cooling/heating is to be investigated, then the ratio will differ from unity.

Starting from the Equation (2.7) and integrating twice, C_1 and C_2 are the integration constants and to be evaluated using

$$T_o = \int -\frac{Pr}{\mu_o}(\gamma - 1)M_w^2 \tau U_o dy + \int \frac{Pr}{\mu_o} C_1 dy + C_2. \qquad (2.17)$$

In this problem the shear stress is constant and rearranging the expression for shear stress, $\tau = \mu_o \frac{dU_o}{dy}$, to obtain viscosity

$$\frac{1}{\mu_o} = \frac{\frac{dU_o}{dy}}{\tau}.$$ (2.18)

When substituted in Equation (2.17),

$$T_o = \int -\frac{\text{Pr}}{\mu_o}(\gamma-1)M_w^2\mu_o\frac{dU_o}{dy}U_o dy + \int \frac{\text{Pr}}{\tau}\frac{dU_o}{dy}C_1 dy + C_2$$ (2.19)

μ_o to give

$$T_o = -\frac{\text{Pr}}{2}(\gamma-1)M_w^2 U_o^2 + C_1\frac{\text{Pr}}{\tau}U_o + C_2$$ (2.20)

Applying the boundary conditions to determine constants, C_1 and C_2.

$$T_o = -\frac{\text{Pr}}{2}(\gamma-1)M_w^2 U_o^2 + \frac{\text{Pr}}{\tau}(\frac{\tau}{\text{Pr}}(1+\frac{1}{2}\text{Pr}(\gamma-1)M_w^2 - T_w))U_o + T_w$$ (2.21)

$$T_o = T_r\left[r + (1-r)U_o - (1-\frac{1}{T_r})U_o^2\right].$$ (2.22)

Equation (2.22) gives the temperature distribution in flow field.

From constant shear stress one can write an expression for the derivative of the velocity as $\frac{dU_o}{dy} = \frac{\tau}{\mu_o}$, and then introducing Sutherland's law of viscosity,

$$\frac{dU_o}{dy} = \frac{\tau}{T_o^{3/2}}\frac{(T_o+C)}{(1+C)},$$ (2.23)

$$\frac{dU_o}{dy} = \tau \frac{\left(T_r\left[r + (1-r)U_o - (1-\frac{1}{T_r})U_o^2\right] + C\right)}{\left(T_r\left[r + (1-r)U_o - (1-\frac{1}{T_r})U_o^2\right]\right)^{3/2}(1+C)}. \tag{2.24}$$

The energy and x – momentum equations define the problem. The shear stress τ is not known *a priori* and must be determined as a part of iterative solution process. The mean pressure gradient is constant or zero. To determine the velocity gradient an iterative process is used. An estimate to the value of τ is made and this estimate is used in a 4th order Runga - Kutta (RK) scheme to integrate Equation (2.24) from $y = 0$ to $y = 1$, using the shooting method. The result of the integration at the upper wall is used in a Newton - Raphson iterative scheme to estimate a better guess for the shear stress, and the process is repeated until convergence to the velocity boundary condition at the upper wall. The coefficients of the 4th order Runga - Kutta method are:

$$k_1 = f(x_i, y_i),$$

$$k_2 = f(x_i + \frac{1}{2}d, y_i + \frac{1}{2}dk_1),$$

$$k_3 = f(x_i + \frac{1}{2}d, y_i + \frac{1}{2}dk_2),$$

$$k_4 = f(x_i + d, y_i + dk_3), \tag{2.25}$$

and velocity at the node is

$$U_o(i+1) = U_o(i) + \frac{1}{6}d(k_1 + 2k_2 + 2k_3 + k_4). \tag{2.26}$$

In Figure 2.2 the curves show the comparison of basic flow solutions using the method of 4th order RK and the explicit solution of momentum-energy equations employing Sutherland's viscosity rule for zero pressure gradient. Curves in Figure 2.3 are again the basic flow solutions for different wall Mach numbers.
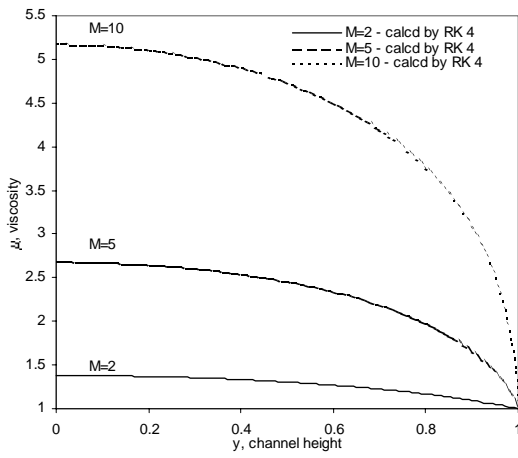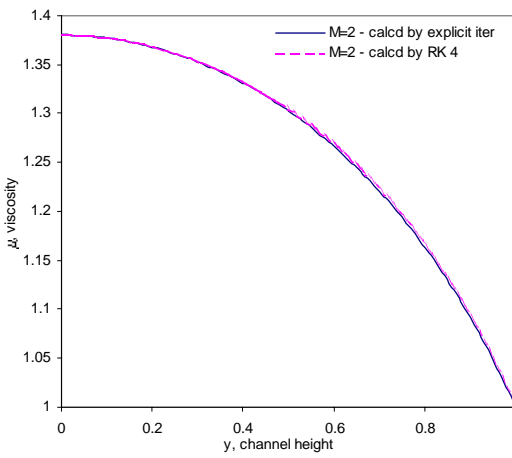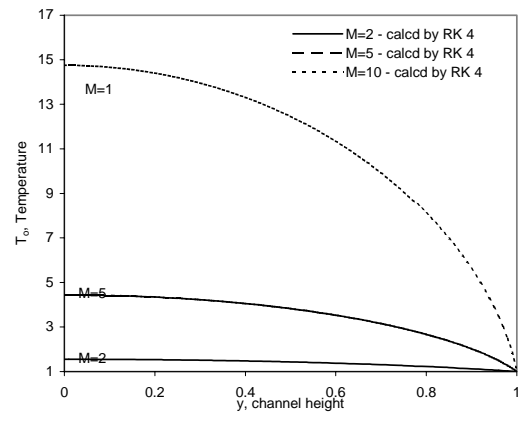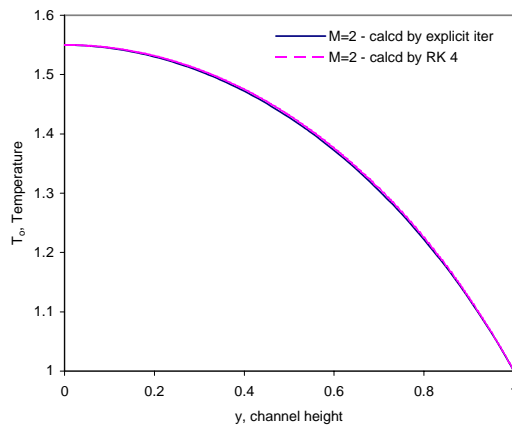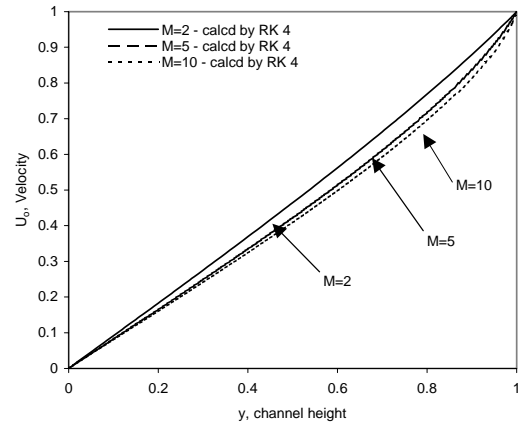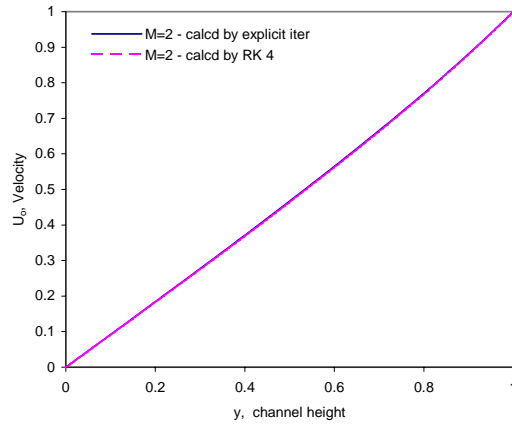
Figure 2.2. 4th order R-K and explicit
solution at zero pressure gradient

Figure 2.3. Velocity, temperature and viscosity
profiles for $M_w = 2$, 5 and 10

2.2.2. Derivatives of Mean Flow Velocity and Temperature

The equations for the linear stability analysis contain the first and second order derivatives of temperatures. In this section expressions for these quantities will be developed.

Analytically using the Equation (2.6) states the constant shear across the channel height and introducing Sutherland's viscosity law, one can get the velocity derivative

$$\frac{dU_o}{dy} = \frac{\tau}{T_o^{3/2}} \frac{(T_o + C)}{(1 + C)} \, , \tag{2.27}$$

$$\frac{dU_o}{dy} = \tau \frac{\left(T_r \left[r + (1-r)U_o - (1-\frac{1}{T_r})U_o^2 \right] + C \right)}{\left(T_r \left[r + (1-r)U_o - (1-\frac{1}{T_r})U_o^2 \right] \right)^{3/2} (1 + C)} \, . \tag{2.28}$$

Similarly $\frac{d^2U_o}{dy^2}$ is determined by simple algebra.

The temperature derivative which is needed in the generalized eigenvalue problem is determined as

$$\frac{dT_o}{dy} = T_r \left[(1-r) - 2(1-\frac{1}{T_r})U_o \right] \frac{dU_o}{dy} \, . \tag{2.29}$$

2.2.3. Derivatives of Mean Flow Viscosity and Thermal Conductivity

Sutherland's viscosity law is used to represent the variation of viscosity with temperature in dimensional form, $\frac{\mu_o^*}{\mu_\infty^*} = (\frac{T_o^*}{T_\infty^*})^{3/2} \frac{(T_\infty^* + S)}{(T_o^* + S)}$. In dimensionless form, the

24

viscosity variation can be written as a function of temperature in the form of

$$\mu_o = (T_o)^{3/2} \frac{(1+C)}{(T_o+C)}.$$

Hence

$$\frac{d\mu_o}{dT_o} = \frac{3}{2} T_o^{1/2} (\frac{1+C}{T_o+C}) - T_o^{3/2} \frac{(1+C)}{(T_o+C)^2}.$$
(2.30)

Simplifying the relation as

$$\frac{d\mu_o}{dT_o} = \frac{3}{2} \frac{\mu_o}{T_o} - \frac{\mu_o}{(T_o+C)},$$
(2.31)

and

$$\frac{d^2\mu_o}{dT_o^2} = \frac{3}{2} \frac{(\frac{d\mu_o}{dT_o} T_o - \mu_o)}{T_o^2} - \frac{(\frac{d\mu_o}{dT_o}(T_o+C) - \mu_o)}{(T_o+C)^2}.$$
(2.32)

Key's law of thermal conductivity of a gas defined in dimensional form is given as by Mack [20]

$$k_o(y) = 0.6325 \frac{\sqrt{T_o}}{1+(\frac{245.4}{T_o}).10^{\frac{-12}{T_o}}} \; cal/cm-\sec.^o C \text{ for } T_o > 80K,$$
(2.33)

$$k_o(y) = (0.222964x10^{-6})T_o \; cal/cm-\sec.^o C \text{ for } T_o \leq 80K,$$
(2.34)

or simply

$$k_o = \frac{\mu_o c_{po}}{\Pr}.$$
(2.35)

Thermal conductivity, k_o, is related to the Pr number and in this study for the dimensionless mean flow, the thermal conductivity, k_o, is made equal to the

kinematic viscosity as $k_o = \mu_o$, assuming the $\Pr \leq 1$ and dimensionless mean specific heat at constant pressure, c_{po}, is constant for air.

Then the derivatives of thermal conductivity assuming $k_o = \mu_o$,

$$\frac{dk_o}{dy} = \frac{d\mu_o}{dy} = \frac{(1+C)\left[\frac{3}{2}T_o^{1/2}\frac{dT_o}{dy}(T_o+C) - \frac{dT_o}{dy}T_o^{3/2}\right]}{(T_o+C)^2}, \qquad (2.36)$$

$$\frac{d^2k_o}{dy^2} = (1+C)\frac{\left[\begin{array}{l}\left\{\begin{array}{l}\left(\frac{3}{2}\frac{1}{2}T_o^{-1/2}\frac{dT_o}{dy}\right)\frac{dT_o}{dy}(T_o+C) + \frac{3}{2}T_o^{1/2}\frac{d^2T_o}{dy^2}(T_o+C) \\ +\frac{3}{2}T_o^{1/2}\frac{dT_o}{dy}\frac{dT_o}{dy} - \left(\frac{d^2T_o}{dy^2}T_o^{3/2} + \frac{dT_o}{dy}\left(\frac{3}{2}T_o^{1/2}\frac{dT_o}{dy}\right)\right)\end{array}\right\}(T_o+C)^{3/2} \\ -\left\{2(T_o+C)\frac{dT_o}{dy}\left[\frac{3}{2}T_o^{1/2}\frac{dT_o}{dy}(T_o+C) - \frac{dT_o}{dy}T_o^{3/2}\right]\right\}\end{array}\right]}{(T_o+C)^4},$$

$$(2.37)$$

and

$$\frac{dk_o}{dT_o} = \frac{d\mu_o}{dT_o} = \frac{3}{2}\left(\frac{\mu_o}{T_o}\right) - \left(\frac{\mu_o}{T_o+C}\right). \qquad (2.38)$$

2.3. Governing Equations of Perturbation Flow

Considering two-dimensional disturbances for the lowest limit of stability is sufficient and approved by Squire's theorem, three-dimensional form of the compressible viscous equations of motion is considered having a potential capacity in case of three-dimensional disturbances. The Squire theorem states that when the mean flow velocities in $y-$ and $z-$ directions are zero, the lowest value of the critical Reynolds number occurs when $\beta = 0$. The equation governing a three-dimensional oscillation is the same as that of a two-dimensional oscillation except the wave

number, β, and other terms for the z – momentum equation. If α and β are real, the presence of β raises the viscosity. The minimum Reynolds number for instability is higher for an oblique wave than for a pure two-dimensional wave.(Betchov and Criminale [21])

Here, in the stability calculations two-dimensional disturbances are considered and the wave number, β in z – direction taken to be zero. Here are the set of equations of motion, continuity, energy, equation of state and Sutherland's rule of viscosity for viscous compressible ideal gases in dimensional form, respectively, are as given below in Equations (2.39-2.45).

$$\rho^* \left[\frac{\partial u^*}{\partial t^*} + u^* \frac{\partial u^*}{\partial x^*} + v^* \frac{\partial u^*}{\partial y^*} + w^* \frac{\partial u^*}{\partial z^*} \right]$$
$$= -\frac{\partial P^*}{\partial x^*} + \frac{\partial}{\partial x^*} \left[\mu^* (2\frac{\partial u^*}{\partial x^*} - \frac{2}{3}(\frac{\partial u^*}{\partial x^*} + \frac{\partial v^*}{\partial y^*} + \frac{\partial w^*}{\partial z^*})) \right], \qquad (2.39)$$
$$+ \frac{\partial}{\partial y^*} \left[\mu^* (\frac{\partial v^*}{\partial x^*} + \frac{\partial u^*}{\partial y^*}) \right] + \frac{\partial}{\partial z^*} \left[\mu^* (\frac{\partial w^*}{\partial x^*} + \frac{\partial u^*}{\partial z^*}) \right]$$

$$\rho^* \left[\frac{\partial v^*}{\partial t^*} + u^* \frac{\partial v^*}{\partial x^*} + v^* \frac{\partial v^*}{\partial y^*} + w^* \frac{\partial v^*}{\partial z^*} \right] = -\frac{\partial P^*}{\partial y^*} + \frac{\partial}{\partial x^*} \left[\mu^* (\frac{\partial v^*}{\partial x^*} + \frac{\partial u^*}{\partial y^*}) \right]$$
$$+ \frac{\partial}{\partial y^*} \left[\mu^* (2\frac{\partial v^*}{\partial y^*} - \frac{2}{3}(\frac{\partial u^*}{\partial x^*} + \frac{\partial v^*}{\partial y^*} + \frac{\partial w^*}{\partial z^*})) \right] + \frac{\partial}{\partial z^*} \left[\mu^* (\frac{\partial w^*}{\partial y^*} + \frac{\partial v^*}{\partial z^*}) \right] - g^* \qquad (2.40)$$

$$\rho^* \left[\frac{\partial w^*}{\partial t^*} + u^* \frac{\partial w^*}{\partial x^*} + v^* \frac{\partial w^*}{\partial y^*} + w^* \frac{\partial w^*}{\partial z^*} \right] = -\frac{\partial P^*}{\partial z^*} + \frac{\partial}{\partial x^*} \left[\mu^* (\frac{\partial w^*}{\partial x^*} + \frac{\partial u^*}{\partial z^*}) \right]$$
$$+ \frac{\partial}{\partial y^*} \left[\mu^* (\frac{\partial w^*}{\partial y^*} + \frac{\partial v^*}{\partial z^*}) \right] + \frac{\partial}{\partial z^*} \left[\mu^* (2\frac{\partial w^*}{\partial z^*} - \frac{2}{3}(\frac{\partial u^*}{\partial x^*} + \frac{\partial v^*}{\partial y^*} + \frac{\partial w^*}{\partial z^*})) \right] \qquad (2.41)$$

$$\frac{\partial \rho^*}{\partial t^*} + \frac{\partial(\rho^* u^*)}{\partial x^*} + \frac{\partial(\rho^* v^*)}{\partial y^*} + \frac{\partial(\rho^* w^*)}{\partial z^*} = 0, \qquad (2.42)$$

$$\rho * c_p * \left[\frac{\partial T *}{\partial t *} + u * \frac{\partial T *}{\partial x *} + v * \frac{\partial T *}{\partial y *} + w * \frac{\partial T *}{\partial z *} \right]$$

$$= \frac{\partial}{\partial x *}(k * \frac{\partial T *}{\partial x *}) + \frac{\partial}{\partial y *}(k * \frac{\partial T *}{\partial y *}) + \frac{\partial}{\partial z *}(k * \frac{\partial T *}{\partial z *}) , \qquad (2.43)$$

$$+ \frac{\partial P *}{\partial t *} + u * \frac{\partial P *}{\partial x *} + v * \frac{\partial P *}{\partial y *} + w * \frac{\partial P *}{\partial z *} + \Phi *$$

where

$$\Phi * = 2\mu * \left[\begin{array}{c} (\frac{\partial u *}{\partial x *})^2 + (\frac{\partial v *}{\partial y *})^2 + (\frac{\partial w *}{\partial z *})^2 \\ + \frac{1}{2}(\frac{\partial v *}{\partial x *} + \frac{\partial u *}{\partial y *})^2 + \frac{1}{2}(\frac{\partial w *}{\partial y *} + \frac{\partial v *}{\partial z *})^2 + \frac{1}{2}(\frac{\partial u *}{\partial z *} + \frac{\partial w *}{\partial x *})^2 - \frac{1}{3}(\nabla . V *) \end{array} \right] .$$

$$P* = \rho * R * T * \qquad (2.44)$$

From Schlichting [22], Sutherland's law for the viscosity is given by Equation (2.45)

$$\frac{\mu *}{\mu_\infty *} = (\frac{T *}{T_\infty *})^{3/2} \frac{T_\infty * + S_1 *}{T * + S_1 *} \qquad (2.45)$$

The flow area is in micro dimensions and the effect of gravity is negligible.

Newtonian perfect fluid between two parallel planes is confined between $y* = 0$ and $y* = h*$ assuming the fully developed flow in $x -$ direction and the calculations for fully developed flow are shown in Appendix A.

In case of parallel flow assumption, the flow parameters are function of $y*$ only, *i.e.*, $u* = u*(y*)$, $w* = w*(y*)$, $T* = T*(y*)$, $\mu* = \mu*(y*)$, $k* = k*(y*)$ and normal component of the mean velocity is zero, $v* = 0$.

Cartesian coordinate system and the following scaling factors are used in non-dimensionalization of the conservation equations. Length scale is the channel height,

h^*, velocity scale is the velocity at the upper moving wall, U_∞^*. Density ρ_∞^*, viscosity μ_∞^* and conductivity k_∞^* are all at the reference temperature of 288 K for upper wall, pressure is nondimensionalized by $\rho_\infty^* U_\infty^{*\,2}$ and the time scale by $\dfrac{h^*}{U_\infty^*}$. All other variables are nondimensionalized by their corresponding values on the upper wall. The dimensionless variables are represented by the same symbol as those used for the dimensional variables but without the asterisk, *.

In the next step, we separate the flow into steady mean and unsteady small fluctuations:

$$u = \bar{u}(y) + \tilde{u}(x,y,z,t) \qquad v = \bar{v}(y) + \tilde{v}(x,y,z,t) \qquad w = \bar{w}(y) + \tilde{w}(x,y,z,t)$$

$$P = \bar{P}(y) + \tilde{P}(x,y,z,t) \qquad T = \bar{T}(y) + \tilde{T}(x,y,z,t) \qquad \rho = \bar{\rho}(y) + \tilde{\rho}(x,y,z,t)$$

$$\mu = \bar{\mu}(y) + \tilde{\mu}(x,y,z,t) \qquad \lambda = \bar{\lambda}(y) + \tilde{\lambda}(x,y,z,t) \qquad k = \bar{k}(y) + \tilde{k}(x,y,z,t)$$

In the subsequent discussion we drop the bars from the mean flow terms for simplicity and then cause any confusion in the subsequent analysis.

The introduction of fluctuating and mean flow terms into the dimensionless $x-$ momentum equation results in the following:

$$(\rho + \tilde{\rho})\left[\frac{\partial(u+\tilde{u})}{\partial t} + (u+\tilde{u})\frac{\partial(u+\tilde{u})}{\partial x} + (v+\tilde{v})\frac{\partial(u+\tilde{u})}{\partial y} + (w+\tilde{w})\frac{\partial(u+\tilde{u})}{\partial z}\right]$$

$$= -\frac{\partial(P+\tilde{P})}{\partial x} + \frac{1}{Re}\left(\begin{array}{l} \dfrac{\partial}{\partial x}\left[(\mu+\tilde{\mu})(2\dfrac{\partial(u+\tilde{u})}{\partial x} - \dfrac{2}{3}(\dfrac{\partial(u+\tilde{u})}{\partial x} + \dfrac{\partial(v+\tilde{v})}{\partial y} + \dfrac{\partial(w+\tilde{w})}{\partial z})\right] \\[4mm] + \dfrac{\partial}{\partial y}\left[(\mu+\tilde{\mu})(\dfrac{\partial(v+\tilde{v})}{\partial x} + \dfrac{\partial(u+\tilde{u})}{\partial y})\right] \\[4mm] + \dfrac{\partial}{\partial z}\left[(\mu+\tilde{\mu})(\dfrac{\partial(w+\tilde{w})}{\partial x} + \dfrac{\partial(u+\tilde{u})}{\partial z})\right] \end{array}\right),$$

$$(2.46)$$

$y-$ and $z-$ momentum equations after the nondimensionalization takes the similar form of $x-$ momentum equation. Continuity and energy equations and finally equation of state are following in Equations (2.47-2.49):

$$\frac{\partial(\rho+\tilde{\rho})}{\partial t}+\frac{\partial\left[(\rho+\tilde{\rho})(u+\tilde{u})\right]}{\partial x}+\frac{\partial\left[(\rho+\tilde{\rho})(v+\tilde{v})\right]}{\partial y}+\frac{\partial\left[(\rho+\tilde{\rho})(w+\tilde{w})\right]}{\partial z}=0 \quad (2.47)$$

$$(\rho+\tilde{\rho})\left[\frac{\partial(T+\tilde{T})}{\partial t}+(u+\tilde{u})\frac{\partial(T+\tilde{T})}{\partial x}+(v+v)\frac{\partial(T+\tilde{T})}{\partial y}+(w+\tilde{w})\frac{\partial(T+\tilde{T})}{\partial z}\right]$$

$$=\frac{1}{\mathrm{Re\,Pr}}\left(\frac{\partial}{\partial x}\left[(k+\tilde{k})\frac{\partial(T+\tilde{T})}{\partial x}\right]+\frac{\partial}{\partial y}\left[(k+\tilde{k})\frac{\partial(T+\tilde{T})}{\partial y}\right]+\frac{\partial}{\partial z}\left[(k+\tilde{k})\frac{\partial(T+\tilde{T})}{\partial z}\right]\right)$$

$$+(\gamma-1)M_w^2\left(\frac{\partial(P+\tilde{P})}{\partial t}+(u+\tilde{u})\frac{\partial(P+\tilde{P})}{\partial x}+(v+\tilde{v})\frac{\partial(P+\tilde{P})}{\partial y}+(w+\tilde{w})\frac{\partial(P+\tilde{P})}{\partial z}\right)$$

$$+(\gamma-1)\frac{M_w^2}{\mathrm{Re}}\ 2(\mu+\tilde{\mu})\left[\begin{array}{l}(\frac{\partial(u+\tilde{u})}{\partial x})^2+(\frac{\partial(v+\tilde{v})}{\partial y})^2+(\frac{\partial(w+\tilde{w})}{\partial z})^2\\[2mm]+\frac{1}{2}\left(\frac{\partial(v+\tilde{v})}{\partial x}+\frac{\partial(u+\tilde{u})}{\partial y}\right)^2\\[2mm]+\frac{1}{2}\left(\frac{\partial(w+\tilde{w})}{\partial y}+\frac{\partial(v+\tilde{v})}{\partial z}\right)^2\\[2mm]+\frac{1}{2}\left(\frac{\partial(u+\tilde{u})}{\partial z}+\frac{\partial(w+\tilde{w})}{\partial x}\right)^2\\[2mm]-\frac{1}{3}(\frac{\partial(u+\tilde{u})}{\partial x}+\frac{\partial(v+\tilde{v})}{\partial y}+\frac{\partial(w+\tilde{w})}{\partial z})\end{array}\right] \quad (2.48)$$

and equation of state for ideal gas:

$$\gamma M_w^2(P+\tilde{P})=(\rho+\tilde{\rho})(T+\tilde{T}) \quad (2.49)$$

Throughout the nondimensionalisation of the equations, we have groups of constants as follows:

$$\frac{1}{\mathrm{Re}} = (\frac{U_\infty^*}{h^{*2}})(\frac{h^* \mu_\infty^*}{\rho_\infty^* U_\infty^{*2}}) = \frac{\mu_\infty^*}{\rho_\infty^* U_\infty^* h^*},$$

$$\mathrm{Pr} = \frac{\mu_\infty^* c_p^*}{k_\infty^*},$$

$$\frac{1}{\mathrm{Pr}\,\mathrm{Re}} = \frac{h^*}{c_p^* \rho_\infty^* U_\infty^* T_\infty^*} \cdot \frac{k_\infty^* T_\infty^*}{h_\infty^2} = \frac{k_\infty^*}{c_p^* \mu_\infty^*} \cdot \frac{\mu_\infty^*}{\rho_\infty^* h^* U_\infty^*},$$

$$(\gamma - 1)M_w^{\,2} = \frac{h^*}{c_p^* \rho_\infty^* U_\infty^* T_\infty^*} \cdot \frac{\rho_\infty^* U_\infty^{*3}}{h^*} = \frac{U_\infty^{*2}}{c_p^* T_\infty^*} = \frac{U_\infty^{*2}}{(\dfrac{RT_\infty^*}{\gamma - 1})} = (\gamma - 1)\frac{U_\infty^{*2}}{\gamma RT_\infty^*},$$

$$\frac{1}{\mathrm{Re}} \cdot (\alpha - 1)M_w^{\,2} = (\mu_\infty^* \frac{U_\infty^{*2}}{h^{*2}}) \frac{h^*}{c_p^* \rho_\infty^* U_\infty^* T_\infty^*} = \frac{\mu_\infty^*}{h^* \rho_\infty^* U_\infty^*} \cdot \frac{U_\infty^{*2}}{c_p^* T_\infty^*},$$

$$M_w^2 = \frac{U_\infty^{*2}}{a_{sound}^2}.$$

When compared with the mean flow, the perturbations are small, therefore, quadratic fluctuating terms such as $\tilde{u}\dfrac{\partial \tilde{u}}{\partial x} << U\dfrac{\partial \tilde{u}}{\partial x}$ can be neglected.

One can get the simplified x – momentum equation in linearized form as follows:

$$\rho(\frac{\partial \tilde{u}}{\partial t} + u\frac{\partial \tilde{u}}{\partial x} + \tilde{u}\frac{\partial u}{\partial x} + v\frac{\partial \tilde{u}}{\partial y} + \tilde{v}\frac{\partial u}{\partial y} + w\frac{\partial \tilde{u}}{\partial z} + \tilde{w}\frac{\partial u}{\partial z}) + \tilde{\rho}(u\frac{\partial u}{\partial x} + v\frac{\partial u}{\partial y} + w\frac{\partial u}{\partial z})$$

$$= -\frac{\partial \tilde{P}}{\partial x} + \frac{1}{\mathrm{Re}} \left(\begin{array}{l} \dfrac{\partial}{\partial x}\left[\mu(2(\dfrac{\partial \tilde{u}}{\partial x} - \dfrac{1}{3}(\dfrac{\partial \tilde{u}}{\partial x}) - \dfrac{1}{3}\dfrac{\partial \tilde{v}}{\partial y} - \dfrac{1}{3}\dfrac{\partial \tilde{w}}{\partial z}) \right] + \dfrac{\partial}{\partial x}\left[\tilde{\mu}(2(\dfrac{\partial u}{\partial x} - \dfrac{1}{3}(\dfrac{\partial u}{\partial x}) - \dfrac{1}{3}\dfrac{\partial v}{\partial y} - \dfrac{1}{3}\dfrac{\partial w}{\partial z}) \right] \\ + \dfrac{\partial}{\partial y}\left[\mu(\dfrac{\partial \tilde{v}}{\partial x} + \dfrac{\partial \tilde{u}}{\partial y}) \right] + \dfrac{\partial}{\partial y}\left[\tilde{\mu}(\dfrac{\partial v}{\partial x} + \dfrac{\partial u}{\partial y}) \right] + \dfrac{\partial}{\partial z}\left[\mu(\dfrac{\partial \tilde{w}}{\partial x} + \dfrac{\partial \tilde{u}}{\partial z}) \right] + \dfrac{\partial}{\partial z}\left[\tilde{\mu}(\dfrac{\partial w}{\partial x} + \dfrac{\partial u}{\partial z}) \right] \end{array} \right)$$

having simplification on viscosity terms,

$$\rho(\frac{\partial \tilde{u}}{\partial t} + u\frac{\partial \tilde{u}}{\partial x} + \tilde{u}\frac{\partial u}{\partial x} + v\frac{\partial \tilde{u}}{\partial y} + \tilde{v}\frac{\partial u}{\partial y} + w\frac{\partial \tilde{u}}{\partial z} + \tilde{w}\frac{\partial u}{\partial z}) + \tilde{\rho}(u\frac{\partial u}{\partial x} + v\frac{\partial u}{\partial y} + w\frac{\partial u}{\partial z})$$

$$= -\frac{\partial \widetilde{P}}{\partial x} + \frac{1}{\text{Re}} \left(\begin{array}{l} \frac{\partial}{\partial x}\left[\mu(l_2 \frac{\partial \tilde{u}}{\partial x} + l_0 \frac{\partial \tilde{v}}{\partial y} + l_0 \frac{\partial \tilde{w}}{\partial z}) + \tilde{\mu}(l_2 \frac{\partial u}{\partial x} + l_0 \frac{\partial v}{\partial y} + l_0 \frac{\partial w}{\partial z}) \right] \\ + \frac{\partial}{\partial y}\left[\mu(\frac{\partial \tilde{v}}{\partial x} + \frac{\partial \tilde{u}}{\partial y}) + \tilde{\mu}(\frac{\partial v}{\partial x} + \frac{\partial u}{\partial y}) \right] + \frac{\partial}{\partial z}\left[\mu(\frac{\partial \tilde{w}}{\partial x} + \frac{\partial \tilde{u}}{\partial z}) + \tilde{\mu}(\frac{\partial w}{\partial x} + \frac{\partial u}{\partial z}) \right] \end{array} \right), \quad (2.50)$$

where

$$l_1 = 1 + \frac{(-\frac{2}{3}\mu_\infty)}{\mu_\infty} = \frac{1}{3},$$

$$l_2 = 2 + \frac{(-\frac{2}{3}\mu_\infty)}{\mu_\infty} = \frac{4}{3},$$

$$l_0 = 0 + \frac{(-\frac{2}{3}\mu_\infty)}{\mu_\infty} = -\frac{2}{3},$$

therefore the remaining $y-$ and $z-$ momentum, continuity and energy equations become as follows, respectively:

$$\left[\rho(\frac{\partial \tilde{v}}{\partial t} + u\frac{\partial \tilde{v}}{\partial x} + \tilde{u}\frac{\partial v}{\partial x} + v\frac{\partial \tilde{v}}{\partial y} + \tilde{v}\frac{\partial v}{\partial y} + w\frac{\partial \tilde{v}}{\partial z} + \tilde{w}\frac{\partial v}{\partial z}) + \tilde{\rho}(u\frac{\partial v}{\partial x} + v\frac{\partial v}{\partial y} + w\frac{\partial v}{\partial z}) \right]$$

$$= -\frac{\partial \widetilde{P}}{\partial y} + \frac{1}{\text{Re}} \left\{ \begin{array}{l} \frac{\partial}{\partial x}\left[\mu(\frac{\partial \tilde{u}}{\partial y} + \frac{\partial \tilde{v}}{\partial x}) + \tilde{\mu}(\frac{\partial u}{\partial y} + \frac{\partial v}{\partial x}) \right] \\ + \frac{\partial}{\partial y}\left[\mu(l_0 \frac{\partial \tilde{u}}{\partial x} + l_2 \frac{\partial \tilde{v}}{\partial y} + l_0 \frac{\partial \tilde{w}}{\partial z}) + \tilde{\mu}(l_0 \frac{\partial u}{\partial x} + l_2 \frac{\partial v}{\partial y} + l_0 \frac{\partial w}{\partial z}) \right] \\ + \frac{\partial}{\partial z}\left[\mu(\frac{\partial \tilde{v}}{\partial z} + \frac{\partial \tilde{w}}{\partial y}) + \tilde{\mu}(\frac{\partial v}{\partial z} + \frac{\partial w}{\partial y}) \right] \end{array} \right\}, \quad (2.51)$$

$$\left[\rho(\frac{\partial \tilde{w}}{\partial t} + u\frac{\partial \tilde{w}}{\partial x} + \tilde{u}\frac{\partial w}{\partial x} + v\frac{\partial \tilde{w}}{\partial y} + \tilde{v}\frac{\partial w}{\partial y} + w\frac{\partial \tilde{w}}{\partial z} + \tilde{w}\frac{\partial w}{\partial z}) + \tilde{\rho}(u\frac{\partial w}{\partial x} + v\frac{\partial w}{\partial y} + w\frac{\partial w}{\partial z}) \right]$$

$$= -\frac{\partial \widetilde{P}}{\partial z} + \frac{1}{\text{Re}} \left\{ \begin{array}{l} \frac{\partial}{\partial x}\left[\mu(\frac{\partial \tilde{w}}{\partial x} + \frac{\partial \tilde{u}}{\partial z}) + \tilde{\mu}(\frac{\partial w}{\partial x} + \frac{\partial u}{\partial z}) \right] + \frac{\partial}{\partial y}\left[\mu(\frac{\partial \tilde{v}}{\partial z} + \frac{\partial \tilde{w}}{\partial y}) + \tilde{\mu}(\frac{\partial v}{\partial z} + \frac{\partial w}{\partial y}) \right] \\ + \frac{\partial}{\partial z}\left[\mu(l_0 \frac{\partial \tilde{u}}{\partial x} + l_0 \frac{\partial \tilde{v}}{\partial y} + l_2 \frac{\partial \tilde{w}}{\partial z}) + \tilde{\mu}(l_0 \frac{\partial u}{\partial x} + l_0 \frac{\partial v}{\partial y} + l_2 \frac{\partial w}{\partial z}) \right] \end{array} \right\}, \quad (2.52)$$

$$\frac{\partial \tilde{\rho}}{\partial t} + \rho \frac{\partial \tilde{u}}{\partial x} + \tilde{u} \frac{\partial \rho}{\partial x} + \tilde{\rho} \frac{\partial u}{\partial x} + u \frac{\partial \tilde{\rho}}{\partial x} + \rho \frac{\partial \tilde{v}}{\partial y} + \tilde{v} \frac{\partial \rho}{\partial y}$$

$$+ \tilde{\rho} \frac{\partial v}{\partial y} + v \frac{\partial \tilde{\rho}}{\partial y} + \rho \frac{\partial \tilde{w}}{\partial z} + \tilde{w} \frac{\partial \rho}{\partial z} + \rho \frac{\partial \tilde{w}}{\partial z} + \tilde{\rho} \frac{\partial w}{\partial z} + w \frac{\partial \tilde{\rho}}{\partial z} = 0$$

(2.53)

$$\rho \left[\frac{\partial \tilde{T}}{\partial t} + u \frac{\partial \tilde{T}}{\partial x} + \tilde{u} \frac{\partial T}{\partial x} + v \frac{\partial \tilde{T}}{\partial y} + \tilde{v} \frac{\partial T}{\partial y} + w \frac{\partial \tilde{T}}{\partial z} + \tilde{w} \frac{\partial T}{\partial z} \right] + \tilde{\rho} \left[\frac{\partial T}{\partial t} + u \frac{\partial T}{\partial x} + v \frac{\partial T}{\partial y} + w \frac{\partial T}{\partial z} \right]$$

$$= \frac{1}{\Pr \text{Re}} \left\{ \frac{\partial}{\partial x} (k \frac{\partial \tilde{T}}{\partial x} + \tilde{k} \frac{\partial T}{\partial x}) + \frac{\partial}{\partial y} (k \frac{\partial \tilde{T}}{\partial y} + \tilde{k} \frac{\partial T}{\partial y}) + \frac{\partial}{\partial z} (k \frac{\partial \tilde{T}}{\partial z} + \tilde{k} \frac{\partial T}{\partial z}) \right\}$$

$$+ (\gamma - 1) M_w^2 \left\{ \frac{\partial \tilde{P}}{\partial t} + u \frac{\partial \tilde{P}}{\partial x} + \tilde{u} \frac{\partial P}{\partial x} + v \frac{\partial \tilde{P}}{\partial y} + \tilde{v} \frac{\partial P}{\partial y} + w \frac{\partial \tilde{P}}{\partial z} + \tilde{w} \frac{\partial P}{\partial z} \right\}$$

$$+ (\gamma - 1) M_w^2 \frac{\mu}{\text{Re}} \left\{ \begin{array}{l} 2 l_2 (\frac{\partial u}{\partial x} \frac{\partial \tilde{u}}{\partial x} + \frac{\partial v}{\partial y} \frac{\partial \tilde{v}}{\partial y} + \frac{\partial w}{\partial z} \frac{\partial \tilde{w}}{\partial z}) \\[4pt] + 2 l_0 \left[\frac{\partial u}{\partial x} (\frac{\partial \tilde{v}}{\partial y} + \frac{\partial \tilde{w}}{\partial z}) + \frac{\partial v}{\partial y} (\frac{\partial \tilde{u}}{\partial x} + \frac{\partial \tilde{w}}{\partial z}) + \frac{\partial w}{\partial z} (\frac{\partial \tilde{u}}{\partial x} + \frac{\partial \tilde{v}}{\partial y}) \right] \\[4pt] + 2 (\frac{\partial \tilde{u}}{\partial y} + \frac{\partial \tilde{v}}{\partial x}) (\frac{\partial u}{\partial y} + \frac{\partial v}{\partial x}) + 2 (\frac{\partial \tilde{v}}{\partial z} + \frac{\partial \tilde{w}}{\partial y}) (\frac{\partial v}{\partial z} + \frac{\partial w}{\partial y}) + 2 (\frac{\partial \tilde{u}}{\partial z} + \frac{\partial \tilde{w}}{\partial x}) (\frac{\partial u}{\partial z} + \frac{\partial w}{\partial x}) \end{array} \right\}.$$

$$+ (\gamma - 1) M_w^2 \frac{\tilde{\mu}}{\text{Re}} \left\{ \begin{array}{l} l_2 \left[(\frac{\partial u}{\partial x})^2 + (\frac{\partial v}{\partial y})^2 + (\frac{\partial w}{\partial z})^2 \right] + 2 l_0 \left[\frac{\partial u}{\partial x} \frac{\partial v}{\partial y} + \frac{\partial w}{\partial z}) + \frac{\partial u}{\partial x} \frac{\partial w}{\partial z} + \frac{\partial w}{\partial z} \frac{\partial v}{\partial y} \right] \\[4pt] + (\frac{\partial u}{\partial y} + \frac{\partial v}{\partial x})^2 + (\frac{\partial v}{\partial z} + \frac{\partial w}{\partial y})^2 + (\frac{\partial u}{\partial z} + \frac{\partial w}{\partial x})^2 \end{array} \right\}$$

(2.54)

The fluctuating component of equation of state, Equation (2.49), is given as $\tilde{\rho} = \gamma M_w^2 \frac{\tilde{P}}{T} - \rho \frac{\tilde{T}}{T}$ and the mean component is derived as $\gamma M_w^2 P = \rho T$. Due to boundary layer assumption for each plane, P is constant across the layer and is equal to $1/(\gamma M_w^2)$. In that case $\rho = 1/T$ and then the fluctuating component simplifies to $\tilde{\rho} = \gamma M_w^2 \frac{\tilde{P}}{T} - \frac{\tilde{T}}{T^2}$ and is substituted in equations having density fluctuation term, $\tilde{\rho}$.

In all the above equations there are also fluctuating components of viscosity and thermal conductivity which are also functions of temperature as $\tilde{\mu} = \frac{d\mu}{dT} \tilde{T}$, $\tilde{\lambda} = \frac{d\lambda}{dT} \tilde{T}$, $\tilde{k} = \frac{dk}{dT} \tilde{T}$ and to be inserted into the equations before the normal mode stability analysis.

Introducing all simplifying terms obtained into the equations covered, one can get the summary of the equations ready to perturbation analysis.

x – component:

$$\frac{1}{T}\left(\frac{\partial \tilde{u}}{\partial t} + u\frac{\partial \tilde{u}}{\partial x} + \tilde{v}\frac{\partial u}{\partial y} + w\frac{\partial \tilde{u}}{\partial z}\right)$$

$$= -\frac{\partial \tilde{P}}{\partial x} + \frac{\mu}{Re}\left\{ \begin{array}{l} l_2\dfrac{\partial^2 \tilde{u}}{\partial x^2} + l_1\left(\dfrac{\partial^2 \tilde{v}}{\partial x \partial y} + \dfrac{\partial^2 \tilde{w}}{\partial x \partial z}\right) + \left(\dfrac{\partial^2 \tilde{v}}{\partial y \partial x} + \dfrac{\partial^2 \tilde{u}}{\partial y^2}\right) + \dfrac{1}{\mu}\dfrac{d\mu}{dT}\dfrac{dT}{dy}\left(\dfrac{\partial \tilde{v}}{\partial x} + \dfrac{\partial \tilde{u}}{\partial y}\right) \\[2ex] + \dfrac{1}{\mu}\dfrac{d\mu}{dT}\left(\dfrac{d^2u}{dy^2}\tilde{T} + \dfrac{du}{dy}\dfrac{\partial \tilde{T}}{\partial y}\right) + \dfrac{1}{\mu}\dfrac{d^2\mu}{dT^2}\dfrac{dT}{dy}\dfrac{du}{dy}\tilde{T} + \dfrac{\partial^2 \tilde{w}}{\partial z \partial x} + \dfrac{\partial^2 \tilde{u}}{\partial z^2} \end{array} \right\}, \qquad (2.55)$$

y – component:

$$\frac{1}{T}\left(\frac{\partial \tilde{v}}{\partial t} + u\frac{\partial \tilde{v}}{\partial x} + w\frac{\partial \tilde{v}}{\partial z}\right) =$$

$$-\frac{\partial \tilde{P}}{\partial y} + \frac{\mu}{Re}\left\{ \begin{array}{l} \dfrac{\partial^2 \tilde{v}}{\partial x^2} + l_1\left(\dfrac{\partial^2 \tilde{u}}{\partial x \partial y} + \dfrac{\partial \tilde{w}}{\partial y \partial z}\right) + l_2\dfrac{\partial^2 \tilde{v}}{\partial y^2} + \dfrac{\partial^2 \tilde{v}}{\partial z^2} + \dfrac{1}{\mu}\dfrac{d\mu}{dT}\left(\dfrac{\partial \tilde{T}}{\partial x}\dfrac{du}{dy} + \dfrac{\partial \tilde{T}}{\partial z}\dfrac{dw}{dy}\right) \\[2ex] + \dfrac{1}{\mu}\dfrac{d\mu}{dT}\dfrac{dT}{dy}\left[l_0\left(\dfrac{\partial \tilde{u}}{\partial x} + \dfrac{\partial \tilde{w}}{\partial z}\right) + l_2\dfrac{\partial \tilde{v}}{\partial y}\right] + l_2\dfrac{\partial \tilde{v}}{\partial y} \end{array}\right\}, \qquad (2.56)$$

z – component:

$$\frac{1}{T}\left(\frac{\partial \tilde{w}}{\partial t} + u\frac{\partial \tilde{w}}{\partial x} + \tilde{v}\frac{\partial w}{\partial y} + w\frac{\partial \tilde{w}}{\partial z}\right) = -\frac{\partial \tilde{P}}{\partial z}$$

$$+ \frac{\mu}{Re}\left\{ \begin{array}{l} \dfrac{\partial^2 w}{\partial x^2} + l_1\left(\dfrac{\partial^2 u}{\partial x \partial z} + \dfrac{\partial^2 \tilde{v}}{\partial y \partial z}\right) + \dfrac{\partial^2 \tilde{w}}{\partial y^2} + l_2\dfrac{\partial^2 \tilde{w}}{\partial z^2} + \dfrac{1}{\mu}\dfrac{d\mu}{dT}\dfrac{dT}{dy}\left(\dfrac{\partial \tilde{v}}{\partial z} + \dfrac{\partial \tilde{w}}{\partial y}\right) \\[2ex] + \dfrac{1}{\mu}\dfrac{d\mu}{dT}\left(\dfrac{d^2w}{dy^2}\tilde{T} + \dfrac{dw}{dy}\dfrac{\partial \tilde{T}}{\partial y}\right) + \dfrac{1}{\mu}\dfrac{d^2\mu}{dT^2}\dfrac{dT}{dy}\dfrac{dw}{dy}\tilde{T} \end{array}\right\}. \qquad (2.57)$$

Continuity equation after cancellation of the terms due to mean flow variables becomes,

$$\frac{\gamma M_w^2}{T}\frac{\partial \widetilde{P}}{\partial t} - \frac{1}{T^2}\frac{\partial \widetilde{T}}{\partial t} + \frac{1}{T}\frac{\partial \widetilde{u}}{\partial x} + u(\frac{\gamma M_w^2}{T}\frac{\partial \widetilde{P}}{\partial x} - \frac{1}{T^2}\frac{\partial \widetilde{T}}{\partial x}) + \frac{1}{T}\frac{\partial \widetilde{v}}{\partial y}$$

$$-\frac{1}{T^2}\frac{dT}{dy}\widetilde{v} + \frac{1}{T}\frac{\partial \widetilde{w}}{\partial z} + w(\frac{\gamma M_w^2}{T}\frac{\partial P}{\partial z} - \frac{1}{T^2}\frac{\partial \widetilde{T}}{\partial z}) = 0 \qquad (2.58)$$

Finally, energy equation becomes,

$$\frac{1}{T}\left[\frac{\partial \widetilde{T}}{\partial t} + u\frac{\partial \widetilde{T}}{\partial x} + \widetilde{v}\frac{\partial T}{\partial y} + w\frac{\partial \widetilde{T}}{\partial z}\right] = (\gamma-1)M_w^2\left\{\frac{\partial \widetilde{P}}{\partial t} + u\frac{\partial \widetilde{P}}{\partial x} + w\frac{\partial \widetilde{P}}{\partial z}\right\}$$

$$+\frac{k}{\Pr \mathrm{Re}}\left\{\begin{array}{l}\dfrac{\partial^2 \widetilde{T}}{\partial x^2} + \dfrac{\partial^2 \widetilde{T}}{\partial y^2} + \dfrac{\partial^2 \widetilde{T}}{\partial z^2} + \dfrac{1}{k}\dfrac{dk}{dT}\dfrac{dT}{dy}\dfrac{\partial \widetilde{T}}{\partial y} \\[2mm] + (\dfrac{1}{k}\dfrac{dk}{dT}\dfrac{d^2 T}{dy^2} + \dfrac{1}{k}\dfrac{d^2 k}{dT^2}(\dfrac{dT}{dy})^2)\widetilde{T} + \dfrac{1}{k}\dfrac{dk}{dT}\dfrac{dT}{dy}\dfrac{\partial \widetilde{T}}{\partial y}\end{array}\right\} \qquad (2.59)$$

$$(\gamma-1)M_w^2\frac{\mu}{\mathrm{Re}}\left\{2(\frac{\partial \widetilde{u}}{\partial y} + \frac{\partial \widetilde{v}}{\partial x})(\frac{du}{dy}) + 2(\frac{\partial \widetilde{v}}{\partial z} + \frac{\partial \widetilde{w}}{\partial y})(\frac{dw}{dy}) + \frac{1}{\mu}\frac{d\mu}{dT}((\frac{\partial u}{\partial y})^2 + (\frac{\partial w}{\partial y})^2)\right\}$$

2.4. Linear Stability Analysis

The linear stability equation is based on a normal mode analysis of the linearized perturbation equations of the three-dimensional Navier-Stokes equations. In normal mode analysis, small disturbances are resolved into modes which may be treated separately because each satisfies the linear system. The linear stability theory formulas presented in this study are valid for general compressible flows with parallel steady flow fields.

The linear stability is considered for high speed viscous combined plane Couette-Poiseuille flow confined between finite parallel walls located at $y^* = 0$ (lower wall) and $y^* = h^*$ (upper wall) and in Figure 2.4 graphical representation of this geometry can be seen.

Each flow variable is assumed to consist of a mean part and infinitesimally small perturbations. Utilizing normal mode analysis the perturbations are expressed in Fourier series. The resulting disturbance equations are linear partial differential equations in the variables *x, y, z* and *t*.

35
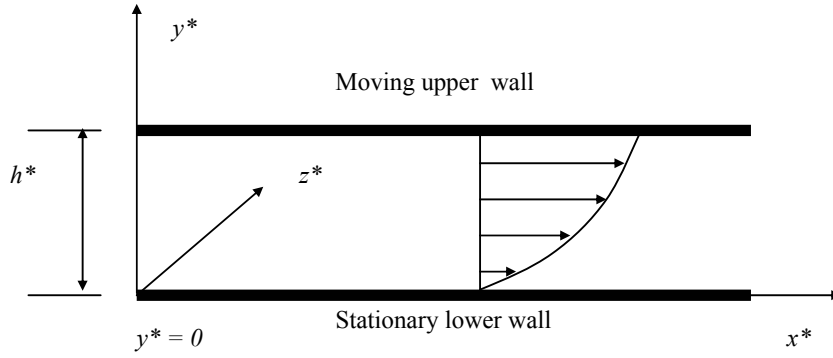
Figure 2.4. Flow geometry for the compressible Couette Flow in a channel

The disturbance equations are linear and the coefficients are functions of y only. Then the separation of variables using normal modes (*i.e.*, exponential solutions in terms of the independent variables) resulting in the ordinary differential equations can be used as in Equation (2.60).

One possible normal mode is the single wave and is excited in harmonic way as:

$$q(x,y,z,t) = \overline{Q}(x,y,z) + \tilde{q}(x,y,z,t)$$

$$\tilde{q}(x,y,z,t) = \hat{Q}(y)e^{i(\alpha x + \beta z - \varpi t)}$$

(2.60)

The frequency $\varpi = \alpha c$, the real part of c is the dimensionless phase speed, c_r, and the imaginary part is the temporal amplification factor, c_i. Disturbances are classified according to normal mode analysis in which are either amplified, neutral, or damped.

The term α is real for the temporal stability formulation and represented as $\alpha = 2\pi / \lambda$, where λ is the wavelength. The amplitude functions only depend on the normal direction for a parallel flow.

2.4.1. Spatial and temporal stability

Considering 2-D disturbances, stability is classified in two parts as spatial and temporal related to growth in space and in time, respectively.

2.4.1.1. Spatial Stability

The local normal mode is given by Equation (2.60). Introducing $\alpha = \alpha_r + i\alpha_i$ and taking ϖ as real, it can be written as

$$\tilde{q}(x,y,t) = \hat{Q}(y)e^{-\alpha_i x}e^{i(\alpha_r x - \varpi t)},$$ (2.61)

The spatial growth rate is given by $-\alpha_i$ for reasons stated as

where

$$\alpha_i < 0 \text{ unstable amplified disturbances,}$$

$$\alpha_i = 0 \text{ neutrally stable,}$$

$$\alpha_i > 0 \text{ stable damped disturbances.}$$

The eigenvalue problem is represented by $\alpha = f(\varpi, \text{Re})$ where f is complex map. The phase speed is defined as $c = \dfrac{\varpi}{\alpha_r}$. The spatial eigenvalue α appears nonlinearly in the governing equations, so they are not suitable to global analysis using the generalized eigenvalue approach. The nonlinearity in α arises from the viscous $\dfrac{d^2\hat{u}}{dx^2}$ terms. Since the instability in high Mach number flows inviscid in nature, the contribution from the viscous terms relatively small. The idea is to drop the α^2 term in the global eigenvalue search.

2.4.1.2. Temporal Stability

The local normal modes are as in the Equation (2.60) but α is real and positive while frequency ω is complex. Therefore, wave velocity, $c = c_r + ic_i$ is complex. Then normal modes is written as

$$\tilde{q}(x, y, t) = \hat{Q}(y)e^{(\alpha c_i t)}e^{i\alpha(x - c_r t)},\qquad (2.62)$$

where

$$c_i > 0 \text{ unstable amplified disturbances,}$$

$$c_i = 0 \text{ neutrally stable,}$$

$$c_i < 0 \text{ stable damped disturbances.}$$

The eigenvalue problem is represented as $c = f(\alpha, \text{Re})$ where f is complex map. Since the eigenvalue, c, appears linearly in temporal eigenvalue problems, most of the stability calculations are concentrated on the temporal generalized eigenvalue problem.

In this study only the temporal eigenvalue problem is solved and all the concentration is just focused on the real α and complex c values, *i.e.*, c_r and c_i.

2.5. Method of Normal Modes and Generalized Eigenvalue Problem

The linear stability analysis is based on normal mode analysis of the linearized perturbation equations of the three-dimensional Navier-Stokes equations. In the normal mode analysis for the linear disturbances, the fluctuations of flow quantities are assumed to be represented by harmonic waves of the following form in three dimensions.

$$\tilde{u}, \tilde{v}, \tilde{w}, \tilde{p}, \tilde{T} = \left[\hat{u}(y), \hat{v}(y), \hat{w}(y), \hat{p}(y), \hat{T}(y)\right]\xi \qquad (2.63)$$

where $\xi = e^{i(\alpha x + \beta z - \varpi t)}$ is the perturbation term which shows the harmonic wave behaviour. The real part of the ϖ, represents the frequency of the disturbance modes while the imaginary part of ϖ represents the temporal amplification rate of disturbances.

Therefore, introducing the perturbation terms into Equations (2.55-2.59) and differentiating with respect to *y*.

x – component:

$$\frac{1}{T}(\hat{u}(-\varpi i)\xi + u\hat{u}(i\alpha)\xi + \hat{v}\xi u' + w\hat{u}(i\beta)\xi)$$

$$= -\hat{P}(i\alpha)\xi + \frac{1}{\text{Re}}\,\mu\left\{ \begin{array}{l} l_2\hat{u}(i\alpha)^2\xi + l_1(\hat{v}'(i\alpha)\xi + \hat{w}(i\beta)(i\alpha)\xi) + \hat{u}''\xi \\[2mm] + \dfrac{1}{\mu}\dfrac{d\mu}{dT}\dfrac{dT}{dy}(\hat{u}'\xi + \hat{v}(i\alpha)\xi) + \dfrac{1}{\mu}\dfrac{d\mu}{dT}(\dfrac{d^2u}{dy^2}\hat{T}\xi + \dfrac{du}{dy}\hat{T}'\xi) \\[2mm] + \dfrac{1}{\mu}\dfrac{d^2\mu}{dT^2}\dfrac{dT}{dy}\dfrac{du}{dy}\hat{T}\xi + \hat{u}(i\beta)^2\xi \end{array} \right\}, \qquad (2.64)$$

y – component:

$$\frac{1}{T}(\hat{v}(-\varpi i)\xi + u\hat{v}(i\alpha)\xi + w\hat{v}(i\beta)\xi)$$

$$= -\hat{P}'\xi + \frac{1}{\text{Re}}\,\mu\left\{ \begin{array}{l} \hat{v}(i\alpha)^2\xi + l_1(\hat{u}'(i\alpha)\xi + \hat{w}'(i\beta)\xi) + l_2\hat{v}'\xi + \hat{v}(i\beta)^2\xi \\[2mm] + \dfrac{1}{\mu}\dfrac{d\mu}{dT}(\hat{T}(i\alpha)\xi\dfrac{du}{dy} + \hat{T}(i\beta)\dfrac{dw}{dy}) \\[2mm] + \dfrac{1}{\mu}\dfrac{d\mu}{dT}\dfrac{dT}{dy}[l_0(\hat{u}(i\alpha)\xi + \hat{w}(i\beta)\xi) + l_2(\hat{v}'\xi)] \end{array} \right\}, \qquad (2.65)$$

z – component:

$$\frac{1}{T}(\hat{w}(-\varpi i)\xi + u\hat{w}(i\alpha)\xi + \hat{v}\xi\frac{\partial w}{\partial y} + w\hat{w}(i\beta)\xi)$$

$$= -\hat{P}(i\beta)\xi + \frac{1}{\mathrm{Re}}\mu\left\{\begin{array}{l}\hat{w}(i\alpha)^2\xi + l_1(\hat{u}(i\alpha)(i\beta)\xi + \hat{v}'(i\beta)\xi) + \hat{w}''\xi + l_2\hat{w}(i\beta)^2\xi \\[2mm] + \frac{1}{\mu}\frac{d\mu}{dT}\frac{dT}{dy}(\hat{v}\xi + \hat{v}(i\beta)\xi) \\[2mm] + \frac{1}{\mu}\frac{d\mu}{dT}(\frac{d^2w}{dy^2}\hat{T}\xi + \frac{dw}{dy}\hat{T}'\xi) + \frac{1}{\mu}\frac{d^2\mu}{dT^2}\frac{dT}{dy}\frac{du}{dy}\hat{T}\xi\end{array}\right\}, \qquad (2.66)$$

continuity :

$$\frac{\gamma M_w^2}{T}(\hat{P}(-i\varpi)\xi) - \frac{1}{T^2}\hat{T}(-i\omega)\xi + \frac{1}{T}\hat{u}(i\alpha)\xi$$

$$+ u(\frac{\gamma M_w^2}{T}\hat{P}(i\alpha)\xi - \frac{1}{T^2}\hat{T}(i\alpha)\xi) + \frac{1}{T}\hat{v}'\xi - \frac{1}{T^2}\frac{dT}{dy}\hat{v}\xi, \qquad (2.67)$$

$$+ \frac{1}{T}\hat{w}(i\beta)\xi + w(\frac{\gamma M_w^2}{T}\hat{P}(i\beta)\xi - \frac{1}{T^2}\hat{T}(i\beta)\xi) = 0$$

energy :

$$\frac{1}{T}\left[\hat{T}(-i\varpi)\xi + u\hat{T}(i\alpha)\xi + \hat{v}\xi\frac{\partial T}{\partial y} + w\hat{T}(i\beta)\xi\right]$$

$$= (\gamma-1)M_w^2\left[\hat{P}(-i\varpi)\xi + u\hat{P}(i\alpha)\xi + w\hat{P}(i\beta)\xi\right]$$

$$+ \frac{k}{\mathrm{Re}\,\mathrm{Pr}}\left[\begin{array}{l}\hat{T}(i\alpha)^2\xi + \hat{T}''\xi + \hat{T}(i\beta)^2\xi + \frac{1}{k}\frac{dk}{dT}\frac{dT}{dy}\hat{T}'\xi \\[2mm] + (\frac{1}{k}\frac{dk}{dT}\frac{d^2T}{dy^2} + \frac{1}{k}\frac{d^2k}{dT^2}(\frac{dT}{dy})^2)\hat{T}\xi + \frac{1}{k}\frac{dk}{dT}\frac{dT}{dy}\hat{T}'\xi\end{array}\right] \qquad (2.68)$$

$$+ (\gamma-1)M_w^2\frac{\mu}{\mathrm{Re}}\left[\begin{array}{l}2\frac{du}{dy}(\hat{u}'\xi + \hat{v}(i\alpha)\xi) + 2\frac{dw}{dy}(\hat{v}(i\beta)\xi + \hat{w}'\xi) \\[2mm] + \frac{1}{\mu}\frac{d\mu}{dy}((\frac{du}{dy})^2 + (\frac{dw}{dy})^2)\end{array}\right]$$

cancelling ξ's from both sides of each equation and rearranging the terms showing the differentiation with respect to y.

x − component becomes:

$$\hat{u}\left[\frac{1}{T}(-\varpi i + ui\alpha + wi\beta) - \frac{1}{\text{Re}}\mu((l_2(i\alpha)^2 + +(i\beta)^2))\right]$$
$$+\hat{v}\left[\frac{1}{T}u' - \frac{1}{\text{Re}}\mu(\frac{1}{\mu}\frac{d\mu}{dT}\frac{dT}{dy})(i\alpha)\right] + \hat{w}\left[-\frac{1}{\text{Re}}\mu(i\beta)(i\alpha)\right] + \hat{u}'\left[-\frac{1}{\text{Re}}\mu(\frac{1}{\mu}\frac{d\mu}{dT}\frac{dT}{dy})\right],$$
$$+\hat{v}'\left[-\frac{1}{\text{Re}}\mu l_1(i\alpha)\right] + \hat{u}''\left[-\frac{1}{\text{Re}}\mu\right] + \hat{T}\left[-\frac{1}{\text{Re}}\mu(\frac{1}{\mu}\frac{d\mu}{dT}\frac{d^2u}{dy^2} + \frac{1}{\mu}\frac{d^2\mu}{dT^2}\frac{dT}{dy}\frac{du}{dy})\right]$$
$$+\hat{T}'\left[-\frac{1}{\text{Re}}\mu(\frac{1}{\mu}\frac{d\mu}{dT}\frac{d^2u}{dy^2} + \frac{1}{\mu}\frac{d\mu}{dT}\frac{du}{dy})\right] + \hat{P}[i\alpha] = 0$$

(2.69)

y − component:

$$\hat{u}\left[-\frac{1}{\text{Re}}\mu(\frac{1}{\mu}\frac{d\mu}{dT}\frac{dT}{dy}l_0(i\alpha))\right] + \hat{v}\left[\frac{1}{T}(-\varpi i + ui\alpha + wi\beta) - \frac{1}{\text{Re}}\mu((i\alpha)^2 + (i\beta)^2)\right]$$
$$+\hat{w}\left[-\frac{1}{\text{Re}}\mu(\frac{1}{\mu}\frac{d\mu}{dT}\frac{dT}{dy})(i\beta)\right] + \hat{u}'\left[-\frac{1}{\text{Re}}\mu(l_1(i\alpha))\right] + \hat{v}'\left[-\frac{1}{\text{Re}}\mu(\frac{1}{\mu}\frac{d\mu}{dT}\frac{dT}{dy}l_2) + \right]$$
$$+\hat{w}'\left[-\frac{1}{\text{Re}}\mu(i\beta)\right] + \hat{v}''\left[-\frac{1}{\text{Re}}\mu(l_2)\right] + \hat{T}\left[-\frac{1}{\text{Re}}\mu(\frac{1}{\mu}\frac{d\mu}{dT}\frac{du}{dy}(i\alpha) + \frac{1}{\mu}\frac{d\mu}{dT}\frac{dw}{dy}(i\beta))\right] + \hat{P}' = 0$$

,(2.70)

z − component:

$$\hat{u}\left[-\frac{1}{\text{Re}}\mu(l_1(i\alpha)(i\beta))\right] + \hat{v}\left[-\frac{1}{\text{Re}}\mu(\frac{1}{\mu}\frac{d\mu}{dT}\frac{dT}{dy})(i\beta) + \frac{1}{T}(\frac{\partial w}{\partial y})\right]$$
$$+\hat{w}\left[-\frac{1}{\text{Re}}\mu(l_2(i\beta)^2 + (i\alpha)^2) + \frac{1}{T}((-\varpi i + u(i\alpha) + w(i\beta)))\right]$$
$$+\hat{v}'\left[-\frac{1}{\text{Re}}\mu(l_1(i\beta))\right] + \hat{w}'\left[-\frac{1}{\text{Re}}\mu(\frac{1}{\mu}\frac{d\mu}{dT}\frac{dT}{dy})\right] + \hat{w}''\left[-\frac{1}{\text{Re}}\mu\right]$$
$$+\hat{T}\left[-\frac{1}{\text{Re}}\mu(\frac{1}{\mu}\frac{d\mu}{dT}\frac{d^2w}{dy^2} + \frac{1}{\mu}\frac{d^2\mu}{dT^2}\frac{dT}{dy}\frac{dw}{dy})\right] + \hat{T}'\left[-\frac{1}{\text{Re}}\mu(\frac{1}{\mu}\frac{d\mu}{dT}\frac{dw}{dy})\right] + \hat{P}(i\beta) = 0$$

,   (2.71)

continuity:

$$
\begin{aligned}
&\hat{u}\left[\frac{1}{T}(i\alpha)\right]+\hat{v}\left[-\frac{1}{T^2}\frac{dT}{dy}\right]+\hat{w}\left[\frac{1}{T}(i\beta)\right]+\hat{v}'\left[\frac{1}{T}\right]\\
&+\hat{T}\left[(-\frac{1}{T^2}(-i\varpi)-u\frac{1}{T^2}(i\alpha)-w\frac{1}{T^2}(i\beta))\right]\\
&+\hat{P}\left[(\frac{\gamma M_w^2}{T}(-i\varpi)+u\frac{\gamma M_w^2}{T}(i\alpha)+w\frac{\gamma M_w^2}{T}(i\beta))\right]=0
\end{aligned}
\qquad (2.72)
$$

energy:

$$
\begin{aligned}
&\hat{v}\left[\frac{1}{T}(\frac{\partial T}{\partial y})-(\gamma-1)M^2\frac{\mu}{\mathrm{Re}}(i\alpha)-2\frac{dw}{dy}(i\beta)\right]+\hat{u}'\left[-(\gamma-1)M^2\frac{\mu}{\mathrm{Re}}2\frac{du}{dy}\right]\\
&+\hat{w}'\left[-(2\frac{dw}{dy})\right]\\
&+\hat{T}\left[\begin{array}{l}\frac{1}{T}(-i\varpi+u(i\alpha)+w(i\beta))\\[6pt]-\frac{k}{\mathrm{Re}\,\mathrm{Pr}}\left\{(i\alpha)^2+(i\beta)^2+\frac{1}{k}\frac{dk}{dT}\frac{d^2T}{dy^2}+\frac{1}{k}\frac{d^2k}{dT^2}(\frac{dT}{dy})^2\right\}\end{array}\right]\\
&+\hat{T}'\left[-\frac{k}{\mathrm{Re}\,\mathrm{Pr}}(\frac{1}{k}\frac{dk}{dT}\frac{dT}{dy}+\frac{1}{k}\frac{dk}{dT}\frac{dT}{dy})\right]+\hat{T}''\left[-\frac{k}{\mathrm{Re}\,\mathrm{Pr}}\right]\\
&-(\gamma-1)M^2\frac{\mu}{\mathrm{Re}}\frac{1}{\mu}\frac{d\mu}{dT}\left[(\frac{du}{dy})^2+(\frac{dw}{dy})^2\right]=0
\end{aligned}
\qquad (2.73)
$$

Linear disturbances satisfying all of the equations results in the generalized eigenvalue problem shown as in Malik [14]

$$
(\mathbf{A}D^2+\mathbf{B}D+\mathbf{C})\Psi_i=0 ,
\qquad (2.74)
$$

where Ψ_i is the five element vector defined by $(\hat{u},\hat{v},\hat{P},\hat{T},\hat{w})^{tr}$ and $\mathbf{A}$, $\mathbf{B}$ and $\mathbf{C}$ which are $(5N+1)x(5N+1)$ matrices of functions of $\alpha,\beta,\omega,\mathrm{Re}$ and M_w. In Equation (2.74) D and D^2 are the first and second derivatives of corresponding eigenvector according to y as follows:

$$D = \frac{d}{dy}, \quad D^2 = \frac{d^2}{dy^2}.$$

A, **B** and **C** matrices are in the form of square matrix and represented in Appendix C.

$$\mathbf{A} = \begin{bmatrix} 1 & 0 & 0 & 0 & 0 \\ 0 & 1 & 0 & 0 & 0 \\ 0 & 0 & 0 & 0 & 0 \\ 0 & 0 & 0 & 1 & 0 \\ 0 & 0 & 0 & 0 & 1 \end{bmatrix}_{5X5} ,$$

$$\mathbf{B} = \begin{bmatrix} B_{11} & B_{12} & B_{13} & B_{14} & B_{15} \\ B_{21} & B_{22} & B_{23} & B_{24} & B_{25} \\ B_{31} & B_{32} & B_{33} & B_{34} & B_{35} \\ B_{41} & B_{42} & B_{43} & B_{44} & B_{45} \\ B_{51} & B_{52} & B_{53} & B_{54} & B_{55} \end{bmatrix}_{5X5} ,$$

$$\mathbf{C} = \begin{bmatrix} C_{11} & C_{12} & C_{13} & C_{14} & C_{15} \\ C_{21} & C_{22} & C_{23} & C_{24} & C_{25} \\ C_{31} & C_{32} & C_{33} & C_{34} & C_{35} \\ C_{41} & C_{42} & C_{43} & C_{44} & C_{45} \\ C_{51} & C_{52} & C_{53} & C_{54} & C_{55} \end{bmatrix}_{5X5} ,$$

The coefficients $\mathbf{B}_{ij}$ and $\mathbf{C}_{ij}$ (i=1,5, j=1,5) are given Appendix C. The disturbance waves are three-dimensional in general. Two-dimensional disturbance modes correspond to a special case of $\beta = 0$. We are interested in two-dimensional basic flow, then the velocity component $w(y)$ may be set to zero in the coefficient matrix in Appendix C.

The boundary conditions for the Equation (2.74) are imposing the isothermal wall temperature at the upper wall. The lower wall assumes either isothermal or adiabatic wall boundary conditions.

43

$$y* = 0 \qquad \Psi_1 = \Psi_2 = \Psi_4 = \Psi_5 = 0 \text{ or } \frac{d\Psi_4}{dy} = 0,$$

$$y* = h* \qquad \Psi_1 = \Psi_2 = \Psi_4 = \Psi_5 = 0. \tag{2.75}$$

Temperature perturbations are assumed to vanish at the solid wall boundaries. In case of isothermal condition for the lower wall, the temperature condition at $y* = 0$ is replaced by $\Psi_4(0) = 0$. Due to high frequency disturbances where the temperature fluctuations do not penetrate deep into the solid wall boundary due to thermal inertia of the solid body, one may replace the isothermal lower wall condition, $\Psi_4 = 0$, with adiabatic $\frac{d\Psi_4(0)}{dy} = 0$.

Equations (2.74) and (2.75) constitute the homogeneous boundary value problem and the main scope is to determine the relation between the α, β, Re, M_w and ϖ that satisfies the system which constitutes a generalized eigenvalue problem.

$$\varpi = \varpi(\alpha, \beta, M_w, Re). \tag{2.76}$$

CHAPTER 3

NUMERICAL APPROACH

3.1. Numerical Method

In order to implement a numerical solution, the computational domain, η, is divided into grids with equal spacing and the physical properties of the fluid are evaluated at the grid points in y – direction.

The differential equations are discretized using $O(h^2)$ finite difference formulae, in the form

$$
\begin{aligned}
&f_1 \mathbf{A}_i \left[\frac{\Psi_{i+1} - 2\Psi_i + \Psi_{i-1}}{\Delta \eta^2} \right] + k_1 \left[(f_2 \mathbf{A}_i + f_3 \mathbf{B}_i)(\frac{\Psi_{i+1} - \Psi_{i-1}}{2\Delta \eta}) \right] + \mathbf{C}_i \Psi_i \\
&+ k_2 \left[f_3 \mathbf{B}_i (\frac{\Psi_{i+1/2} - \Psi_{i-1/2}}{\Delta \eta}) + \mathbf{C}_i (\frac{\Psi_{i+1/2} + \Psi_{i-1/2}}{2}) \right] = 0 \qquad (i = 1..N\text{-}1)
\end{aligned}
\qquad (3.1)
$$

First order continuity equation is shown as

$$
f_3 \mathbf{B}_{i+1/2} \frac{\Psi_{i+1} - \Psi_i}{\Delta \eta} + \mathbf{C}_{i+1/2} \Psi_{i+1/2} = 0 \qquad (i = 0..N\text{-}1) \qquad (3.2)
$$

The terms $\mathbf{A}_i$, $\mathbf{B}_i$, $\mathbf{C}_i$ are the coefficients of stability equations and are given in Appendix C.

Upper Wall (Moving PISTON)

$y = h$ N   _____ $\eta = 1$

N-1/2   - - - - - - - - - - - - - - - - -

N-1   _____

i+1   _____

i+1/2   - - - - - - - - - - - - - - - - - $\hat{P}$

i   _____ $\hat{u}, \hat{v}, \hat{T}, \hat{w}$

i-1/2   - - - - - - - - - - - - - - - - - $\hat{P}$

3/2   - - - - - - - - - - - - - - - - -

1   _____   full nodes

1/2   - - - - - - - - - - - - - - - - -   half nodes

$y = 0$ y

0

    x Lower Wall (Stationary CYLINDER LINER) $\eta = 0$
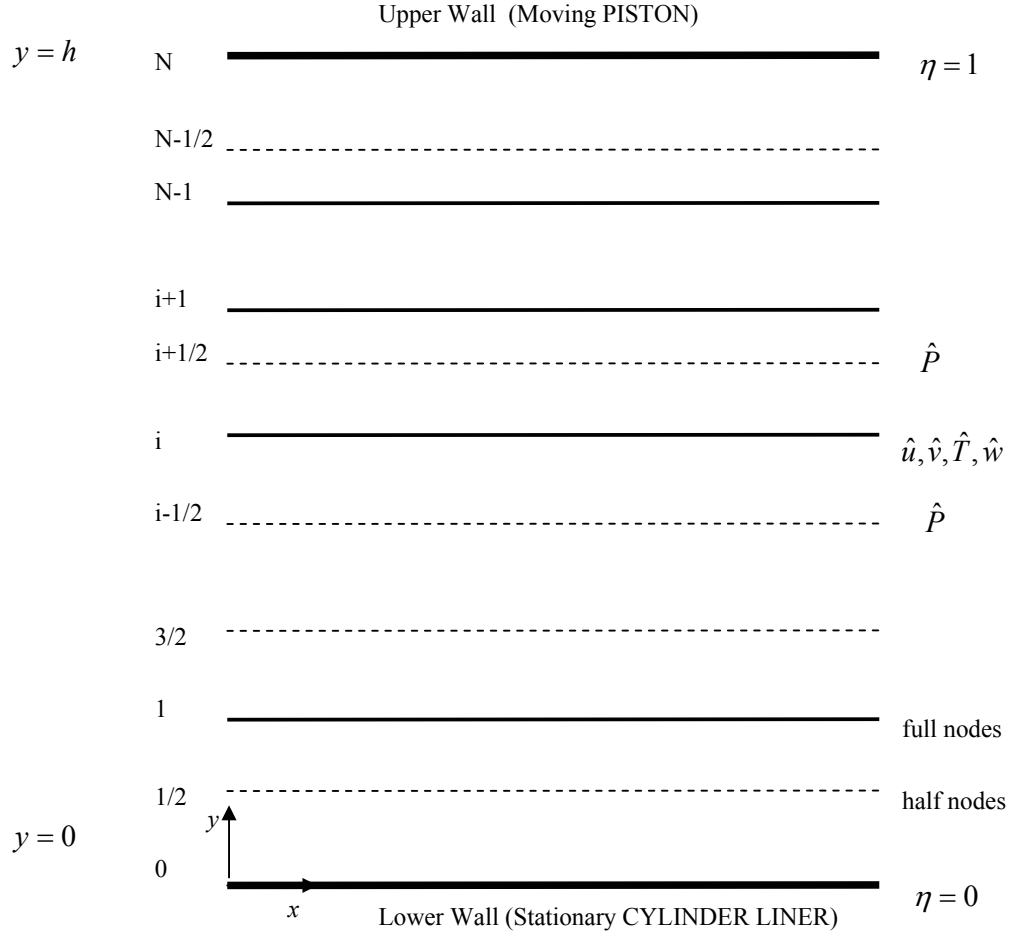
Figure 3.1. Representation of staggered grid used for 2FD discretization (Malik [14])

Nondimensionalized channel height, $0 \leq y \leq h$ is mapped onto the computational domain $0 \leq \eta \leq 1$ by using the following nonlinear transformation

$$y = \frac{a\eta}{b - \eta},$$ (3.3)

where $b = 1 + \dfrac{a}{h}$. Here h is the channel height where the flow conditions are satisfied. The term a is the scaling parameter chosen to optimize the accuracy of the calculations. Here we use $a = \dfrac{hy_i}{(h - 2y_i)}$ which puts the half of the grid point used for

discretization between $y = 0$ and $y = y_i$. The mapping given above clusters the grid points near the walls but in this study, $y_i = \dfrac{h}{2}$ is chosen such that the grid points are all equally spaced in the channel.

The vector Ψ_i is the one corresponding to Ψ at $\eta = i/N$ and has components u_i, v_i, P_i, T_i and w_i.

Also

$$k_1 = 1 \text{ and } k_2 = 0 \text{ are valid for } u_i, v_i, T_i, w_i,$$
$$k_1 = 0 \text{ and } k_2 = 1 \text{ are valid for only } P_i.$$

The parameters f_1, f_2 and f_3 are the weighting factors determining the responsibility of coefficients of eigenvectors in the discretized equations according to grid clustering map encountered and given as

$$f_1 = \frac{(b-\eta)^4}{b^2 a^2},$$

$$f_2 = -\frac{2(b-\eta)^3}{b^2 a^2},$$

$$f_3 = \frac{(b-\eta)^2}{ba}.$$

Since, the value of $y_i = \dfrac{h}{2}$ is encountered in the grid clustering, the values of f_1, f_2 f_3 are calculated as $f_1 = 1$, $f_2 = 0$ and $f_3 = 1$.

Due to the staggered mesh generation there is no need to have artificial pressure boundary condition. The three momentum and energy equations are written at full nodes. The pressure information for those equations at full nodes is obtained from the former and latter neighbour half nodes at which continuity equation is written.

The total number of full nodes encountered is N and the total number of half nodes is N+1. For each full node there exist 4 equations and 1 equation is written at each half nodes. Then the total number of equations written at both full and half nodes is 5N+1. Equation (2.74) with the boundary conditions in Equation (2.75) represent the 5N+1 equations and 5N+1 unknowns to be solved simultaneously.

The discretization of the governing equations reduces the system to generalized eigenvalue problem as

$$\mathbf{A}\Psi = \varpi \mathbf{B}\Psi \tag{3.4}$$

where ϖ is the eigenvalue and in the form of $\varpi = \alpha(c_r + ic_i)$. Real part of the ω, $\mathrm{Re}(\varpi)$, represents the frequency of the disturbance modes, while the imaginary part, $\mathrm{Im}(\varpi)$, represents the temporal amplification rate of disturbances. The term, Ψ is the discrete representation of the eigenfunction. $\mathbf{A}$ and $\mathbf{B}$ are the square coefficient matrices of the stability equations. The matrices are complex and therefore are composed of real and imaginary submatrices. The matrix $\mathbf{A}$ can be depicted as $\mathbf{A}=\mathbf{A}_r+i\mathbf{A}_i$, where $\mathbf{A}_r$ and $\mathbf{A}_i$ are the real and the imaginary part of $\mathbf{A}$, respectively. Similarly, the matrix $\mathbf{B}$ is represented as $\mathbf{B}=\mathbf{B}_r+i\mathbf{B}_i$, where $\mathbf{B}_i$ and $\mathbf{B}_r$ are the real and the imaginary part of $\mathbf{B}$, respectively.

Although the matrix $\mathbf{A}$ contains the coefficients without frequency information but has wave number, α, the matrix $\mathbf{B}$ includes neither frequency nor wave number information.

$$(\mathbf{A}_r + i\mathbf{A}_i)\Psi = \alpha(c_r + ic_i)(\mathbf{B}_r + i\mathbf{B}_i)\Psi \tag{3.5}$$

In this problem, all the elements of the real part of matrix $\mathbf{B}$ are zero, *i.e.*, $\mathbf{B}_r = 0$

IMSL and Eispack *QZ algorithms* were used for the solution of the generalized eigenvalue problem as stated in the Equation (3.5).

The details of the *QZ algorithm* is given in Moler and Stewart [23]. The double precision complex subroutines used as solver are DGVLCG and DWRCRN for IMSL; CQZHES and CQZVAL for Eispack libraries.
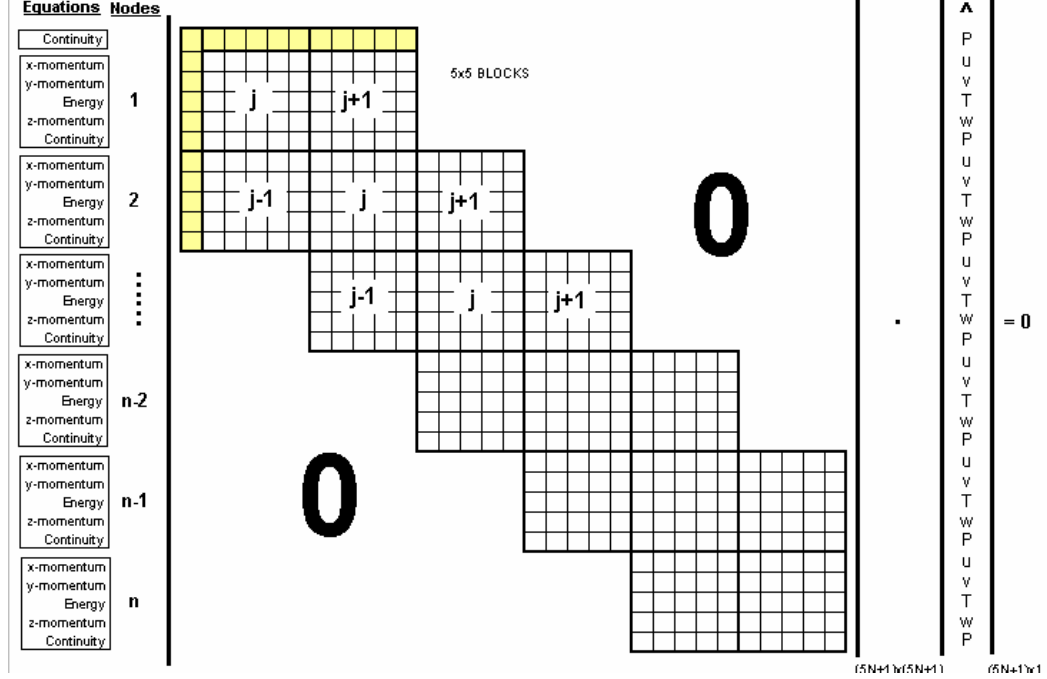

Figure 3.2. Block tridiagonal representation of solution matrix basis for generalized eigenvalue problem using 2nd order finite difference method.

$$\left([\mathbf{A_r}]_{(5N+1)(5N+1)} + i[\mathbf{A_i}]_{(5N+1)(5N+1)}\right)[\mathbf{\Psi}]_{(5N+1)}$$

$$= \alpha c.\left([\mathbf{B_r}]_{(5N+1)(5N+1)} + i[\mathbf{B_i}]_{(5N+1)(5N+1)}\right)[\mathbf{\Psi}]_{(5N+1)}$$

(3.6)

The coefficients of stability equations calculated at each grid point are substituted in the matrices of $\mathbf{A}_r$, $\mathbf{A}_i$, $\mathbf{B}_r$ and $\mathbf{B}_i$ each in the form of general block tridiagonal solution matrix as shown in the Figure 3.2.

49

In this study global eigenvalue search method is employed and in Table 3.1 computational CPU times for the search of global eigenvalues and mean flow solution are shown with respect to the grid points used. The global methods are usually computationally more expensive, but they have the advantage of obtaining the whole set of eigenvalues and eigenfunctions at the same time.

Table 3.1. Pentium 4, CPU 2.4 GHz, Ram 2 Gb time to find eigenvalues by the 2nd order Finite Difference Method

Grid Size	Time for basic flow solution (sec)	Time for Eigenvalue search (sec)
99	7	7
149	14	22
199	12	54
249	10	113
299	11	287
349	9	511
399	9	896

The number of eigenvalues and eigenfunctions thus obtained is proportional to the number of grid points used. On the other hand, the local methods are limited to solving single set of eigenvalue and eigenfunction only but they are usually more computationally efficient than global methods.

CHAPTER 4

VALIDATION OF NUMERICAL METHOD

4.1. Supersonic Plane Couette Flow

Plane Couette flow is the simple flow geometry which is initially treated to validate the code comparing the results in the literature. The stability of plane Couette flow is a standard problem in fluid mechanics and so far either viscous incompressible or inviscid compressible flows have been considered. The stability of incompressible Couette flow has been studied extensively and shown to be stable to linear disturbances. Mack [20] found that there is a new family of multiple higher instability wave modes in supersonic boundary layers. Acoustics instability wave modes similar to the higher modes in compressible boundary layers have also been found in supersonic jets and mixing layers. The existence of walls has a strong effect on the acoustic instability waves in the bounded compressible flows. For validation of the code, Malik [14] and Hu and Zhong [17] are taken as a reference for the comparison of the results of plane Couette flow at Mach numbers 2, 5 and 10.

4.1.1. Validation of the Results and Numerical Accuracy

The linear stability code which solves the generalized eigenvalue problem using the second order finite difference method is first validated by comparing the results to those obtained by Malik [14] and Hu and Zhong [17] for the linear stability of plane Couette flow for compressible and viscous boundary layer.

The flow conditions for the test case are compressible boundary layer over a flat plate with zero pressure gradient at $M_w = 2.5$, $Re = 3000$, $T_o^* = 600^o R$ and $\dfrac{T_w}{T_r} = 1$.

The methods used by Malik [14] are a second order finite difference (2FD) method, a fourth order compact finite difference (4CD) scheme, a single domain spectral collocation (SDSP) method and a multi domain spectral collocation (MDSP) method. For each scheme Malik [14] used first a global method to compute all of the eigenvalues of the discretized system and used a local method to purify the solution and its eigenfunctions. For global methods a guess for the eigenvalue is not required. In a local method, a guess for the eigenvalue is required. Only the eigenvalue which is located in the neighborhood of the guessed value is computed using iterative techniques such as Newton's method.

According to Hu and Zhong [17] better accuracy is obtained both using global and local methods than those obtained only by global method for the same grid points. The methods used by Hu and Zhong [17] are fourth order finite difference global (4FD) method and spectral collocation (SC) method. Hu and Zhong [17] used global eigenvalue search technique employing more grid points to catch the same accuracy as Malik [14].

Table 4.1. The eigenvalue solutions of complex frequency ω for the temporal linear stability of a compressible boundary layer ($M_w = 2.5$, $Re = 3000$, $T_o^* = 600^o R$ and $\dfrac{T_w}{T_r} = 1$, $\alpha = 0.06$ and $\beta = 0.1$ (Hu and Zhong [17])

Methods	Grids	Re(ϖ)	Im(ϖ)
4CD (Malik [14])	61	0.0367321	0.0005847
SDSP (Malik [14])	61	0.0367339	0.0005840
MDSP (Malik [14])	61	0.0367340	0.0005840
SC (Hu and Zhong [17])	100	0.0367337	0.0005840
4FD (Hu and Zhong [17])	100	0.0367338	0.0005845
2FD (present study)	149	0.0355836	0.0005687

In our calculations global method is used and the accuracy of the solution compared to the literature findings are in agreement as shown in Tables 4.1 and 4.2.

The linear stability computations of compressible Couette flow are also validated by comparing the viscous results of Duck *et al*. [16] for the cases of small Mach and small Reynolds numbers. Figures 4.1 and 4.2 show the eigenvalue distribution for $M_w = 2.0$, $\text{Re} = 2x10^5$, $\alpha = 0.1$ and $\beta = 0$.

Table. 4.2. The eigenvalue solutions of wave speed c for compressible Couette flow using spectral method with three sets of grids. The flow conditions are $M_w = 2.0$, $\text{Re} = 2x10^5$, $\alpha = 0.1$ and $\beta = 0$ (Hu and Zhong [17])

Grids	Method	c_r	c_i
		Mode I	
100 (Hu and Zhong [17])	Spectral	1.213695119859	-0.011585118523
200 (Hu and Zhong [17])	Spectral	1.213695119817	-0.011585118448
300 (Hu and Zhong [17])	Spectral	1.213695119854	-0.011585118558
100 (present study)	2FD	1.203594853239	-0.010254316025
200 (present study)	2FD	1.208357023254	-0.010485769412
250 (present study)	2FD	1.209258428513	-0.010958475215
		Mode II	
100 (Hu and Zhong [17])	Spectral	-0.291572925106	-0.013821128462
200 (Hu and Zhong [17])	Spectral	-0.291572925140	-0.013821128536
300 (Hu and Zhong [17])	Spectral	-0.291572925108	-0.013821128457
100 (present study)	2FD	-0.292425810686	-0.013576244212
200 (present study)	2FD	-0.292387596412	-0.013553618857
250 (present study)	2FD	-0.292058574690	-0.013685524863

Recovery factor, r, used is taken to be unity specifying the lower wall recovery temperature is equal to the lower wall temperature for adiabatic conditions. Recovery factor different than unity makes the "Y" shaped dispersion of eigenvalues in $c_r - c_i$ plane to be shifted completely to the left and right in c_r axis according to the value of r reference to Figure 4.1. Hu & Zhong [17] has shown the that "Y"

shaped dispersion, the lower branch is clustered around the $c_r = 0.5$ line. In our case, shift of dispersion of lower part of "Y" shape to the left shows the lower wall temperature is not equal to the upper wall reference temperature. The 0.5 line on the c_r axis shows the equality of upper and lower wall temperatures.
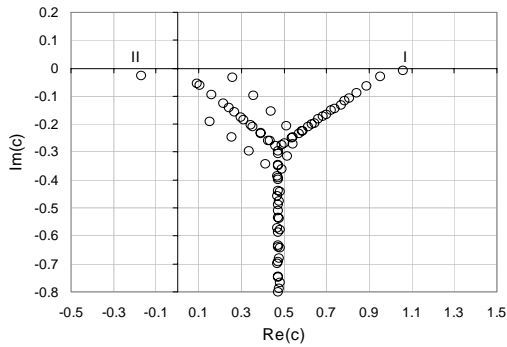

Figure 4.1. Phase velocity spectrum of compressible Couette flow at $M_w = 2.0$, $Re = 2x10^5$ and $\alpha = 0.1$ using 101 grid points
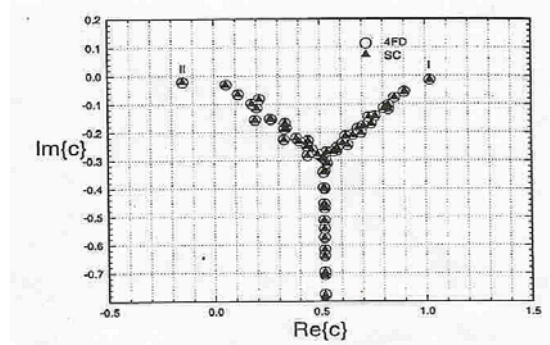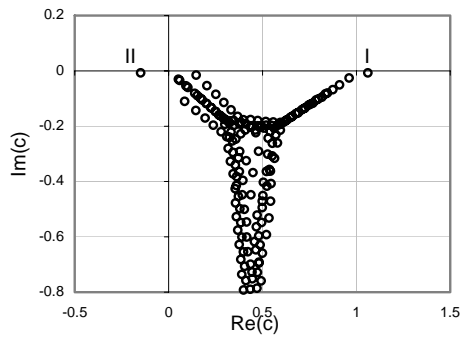

Figure 4.2. Phase velocity spectrum of compressible Couette flow at $M_w = 2.0$, $Re = 2x10^5$ and $\alpha = 0.1$ using 100 grid points. (Hu & Zhong [14])

Figure 4.3. Phase velocity spectrum of compressible Couette Flow at $M_w = 5.0$, $Re = 5x10^6$ and $\alpha = 0.1$ using 199 grid points.
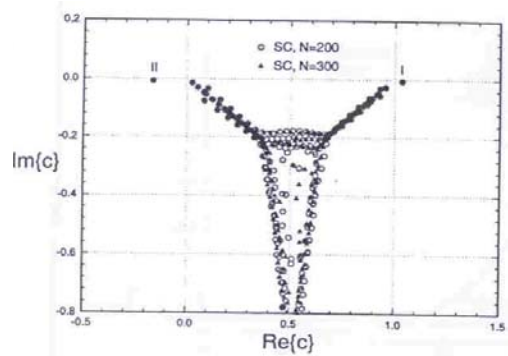

Figure 4.4.   Phase velocity spectrum of compressible   Couette   Flow   at $M_w = 5.0$, $Re = 5x10^6$ and $\alpha = 0.1$ using 200 & 300 grid points using spectral methods (Hu & Zhong [17])
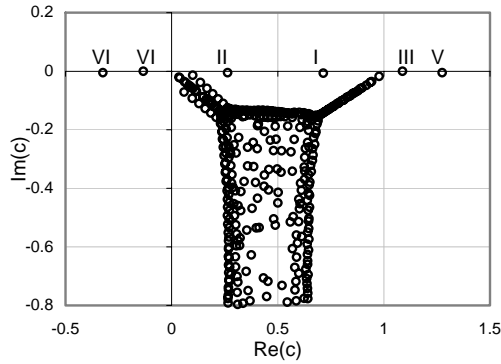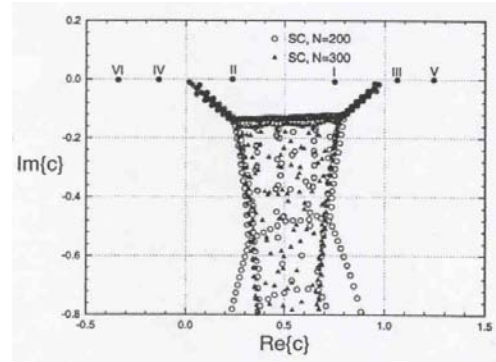
54

Figure 4.5. Phase velocity spectrum of compressible Couette Flow at $M_w = 5.0$, $\text{Re} = 5x10^5$ and $\alpha = 3.5$ using 201 grid points

Figure 4.6. Phase velocity spectrum of compressible Couette Flow at $M_w = 5.0$, $\text{Re} = 5x10^5$ and $\alpha = 3.5$ using 200 & 300 grid points. (Hu and Zhong [17])

In general, $\text{Re}(c)$ and $\text{Im}(c)$ represent c_r and c_i of eigenvalue spectrum, respectively. Figures 4.3 and 4.4 are the comparisons of phase velocity spectrum of compressible Couette flow at $M_w = 5.0$, $\text{Re} = 5x10^6$ and $\alpha = 0.1$ using 199 grid points.

In Figures 4.5 and 4.6, the phase velocity spectrum of compressible Couette flow at $M_w = 5.0$, $\text{Re} = 5x10^5$ and $\alpha = 3.5$ using 201 grid points. SC method with 300 grid points shows better accuracy and distribution of eigenvalues.

Basic flow solutions are very effective on the results and the accuracy of the results is very sensitive to assumptions made on viscosity. For the determination of velocity and temperature profile, Sutherland's viscosity law is employed as done by Hu and Zhong [17] and Malik [14].

4.1.2. Acoustics Wave Modes

Duck et al. [16] have studied the inviscid stability of supersonic Couette flow and found that there are two families of wave modes.

Those wave modes are determined as odd (Mode I, III, etc) and even (Mode II, IV, etc) wave modes. They showed that both families of modes are neutrally stable when $c_r > 1$ (for odd modes) or $c_r < 0$ (for even modes). They found that when $0 < c_r < 1$, both even and odd modes are no longer stable for compressible viscous Couette flow.

In general, odd modes are stable with finite damping but even modes are unstable and mode II has the largest growth rate among the even modes. The necessary condition for the existence of type of acoustic modes is that there is a region of locally supersonic flow relative to the phase speed of the instability wave.

Even Modes: II, IV, VI …(Re(.c)>0)   Odd Modes: I, III, V …(Re(.c)<1
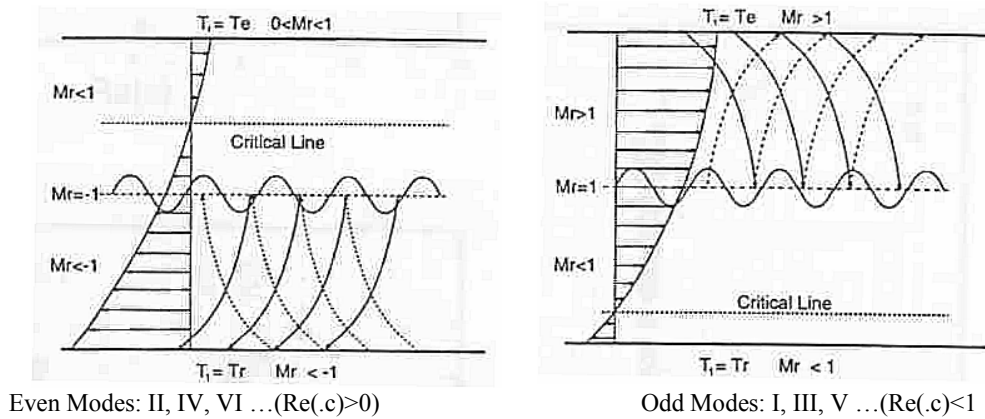
Figure 4.7. Schematic of Mach waves and the two families of wave modes in supersonic Couette flow in reference frames moving at the velocity of the disturbance waves. (Hu & Zhong [17])

M_r is the relative Mach number at the two walls and defined as $M_r = \dfrac{U_o(y) - c}{(T_o(y))^{1/2}} M_w$. Hu and Zhong [17] specified that acoustic wave modes are formed by substained wave reflections between the walls and the relative sonic line. There are two families of acoustic wave modes for the bounded Couette flow

compared to the single family of unbounded compressible boundary layer. The reason for this is there is one family for each boundary.

Figure 4.7 shows the schematic representation of the two families of acoustic modes in compressible Couette flow in reference frame moving with the waves. Odd modes are formed by the acoustic reflections in between critical line (relative sonic line) and upper boundary while even modes are formed in between critical line (relative sonic line) and lower boundary.

Duck et al. [16] found that for the case of adibatic lower wall for inviscid flow limit of $0 < c_r < 1$, in general odd modes are stable with finite damping and even modes are unstable. When the lower and upper wall are at the same temperature, the phase speed is $c_r = 0.5$. It is shown that top boundary is relatively supersonic $|M_r| > 1$ when $c > 1 + \dfrac{1}{M_w}$ or $c < 1 - \dfrac{1}{M_w}$. The bottom boundary is assumed adiabatic with a wall temperature, T_w, is relatively supersonic when the phase velocity approximately $c < -T_w^{1/2}/M_w$ or $c > -T_w^{1/2}/M_w$.

4.1.3. Eigenmode Spectra

Global method is used for the eigenvalues of systems of equations for compressible Couette flow. Mode II is the most unstable mode among the viscous unstable modes and all investigations are based on the Mode II. Although Mode I which was found to be stable by Duck et al. [13] among the inviscid solutions, also found to be unstable at finite Reynolds number indicating that viscosity plays destabilizing role.

Figure 4.8 shows the phase velocity eigenvalue spectrum for Re=5x10^5 and $M_w = 5$ at a small wave number, $\alpha = 0.1$. Spurious modes are present place in the numerical viscous modes.
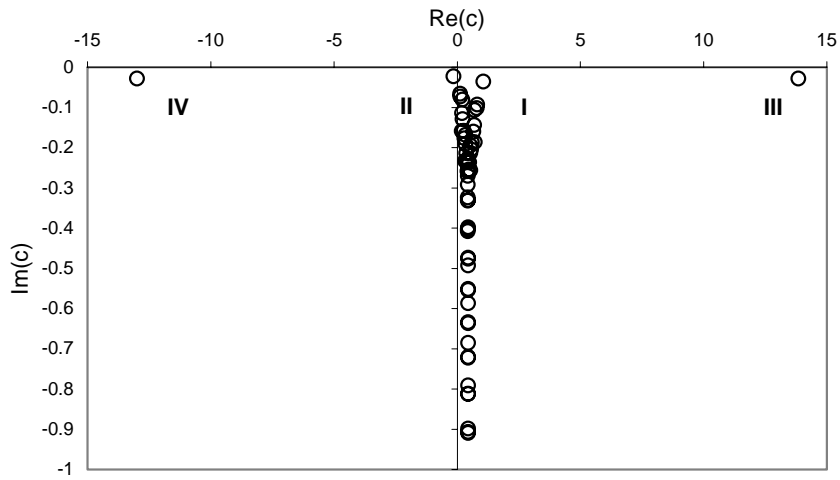
(a)
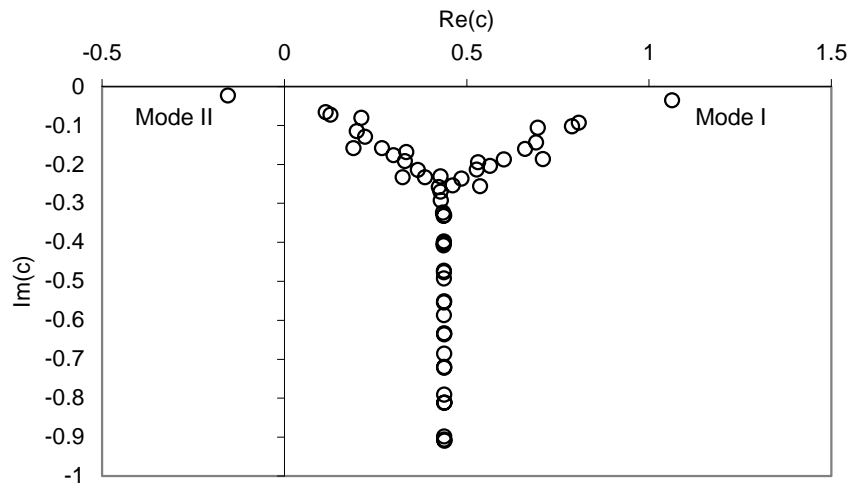
(b)

(a) shows the wide spectrum

(b) local spectrum concentrated on Mode I and Mode II.

Figure 4.8. Phase velocity spectrum for compressible Couette flow at $M_w = 5$, Re=5x10^5 and α=0.1

The eigenvalue spectrum of $M_w = 5$ is consist of "Y" shaped structure and located around the region of c_r between 0 and 1. Two families of inviscid acoustic modes are located at $c_r < 0$ for the even modes and $c_r > 1$ for the odd modes. Those acoustic modes are the results of acoustic wave reflections.

Acoustic wave modes are located close to the $c_i = 0$ line and marked as I, II, III etc. Wave velocities of even modes (Modes II, IV..) satisfy $c_r < 0$ and odd modes (Modes I, III, etc) also satify $c_r > 1$. All those acoustics modes are all stable due to the effect of viscosity.

4.1.4. Effect of Viscosity on Stability

The effect of viscosity on the stability of supersonic Couette flow was investigated by Duck et al. comparing the inviscid flow cases for $M_w = 2$ and $M_w = 5$. Modes I and II are the most unstable modes and are taken into consideration during the study.
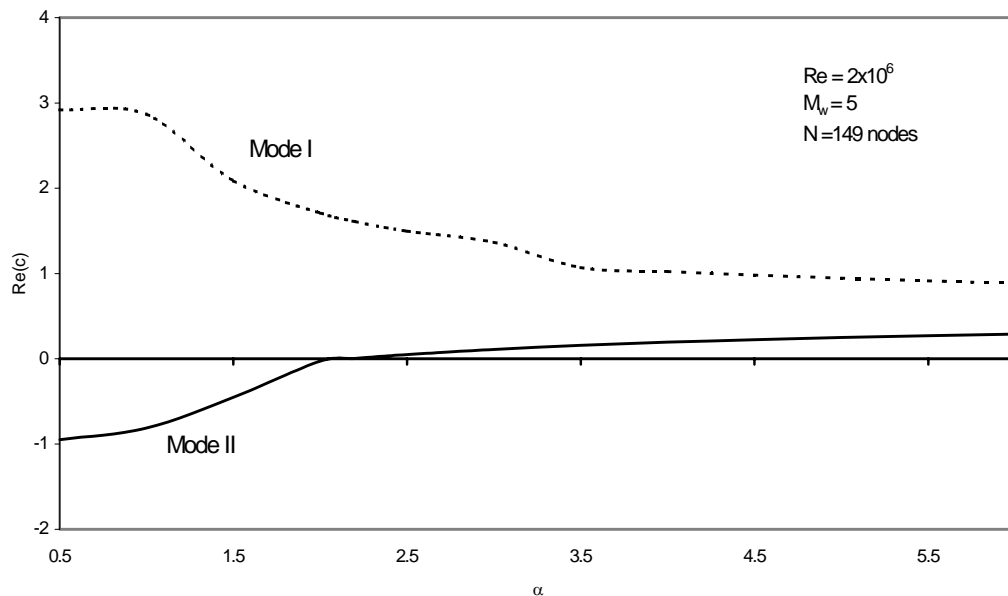

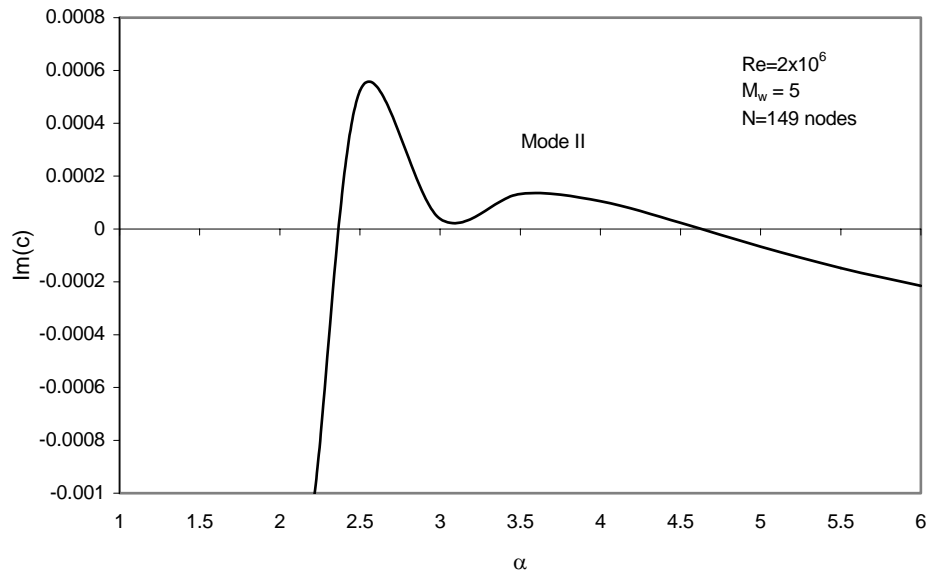Figure 4.9. Phase speed, c_r, of Modes I and II as function of α at a Re=2x10^6, $M_w = 5$

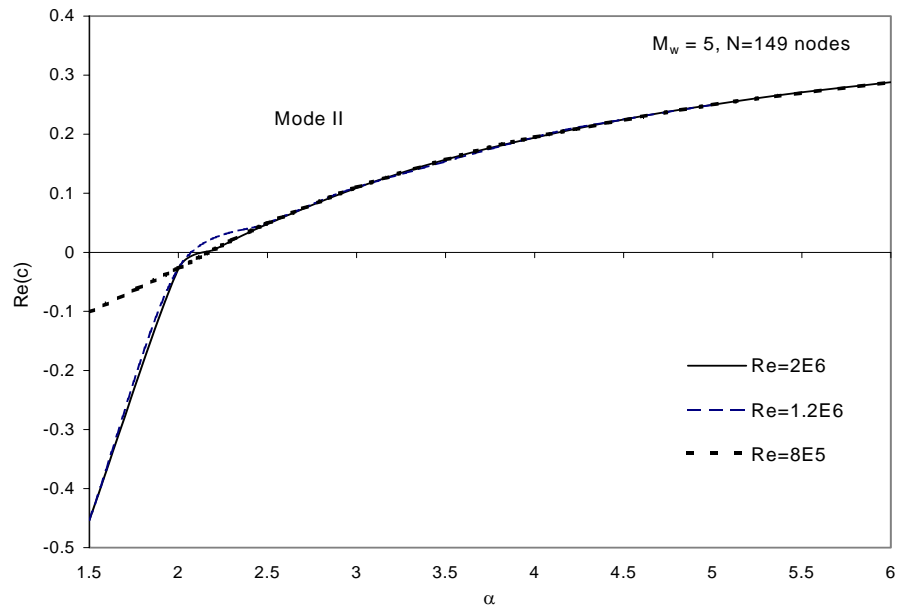Figure 4.10. c_i of Mode II as a function of α at $M_w = 5$ at $Re = 2x10^6$

Figure 4.11. c_r of Mode II as a function of α at $M_w = 5$ at various Reynolds numbers

c_r of modes I and II are shown in Figure 4.9 for $M_w = 5$ at Re=2x10^6 as a function of α. Figure shows that as the α increases c_r of even mode (Mode II) increase while c_r of odd mode (Mode I) decreases.

The two modes intersects the $c_i = 0$ around $\alpha = 3.4$ and for high wave numbers these two modes are unstable (no longer neutrally stable). The c_i of Modes I and II as a function of α for $M_w = 2$ at various Reynolds numbers are shown in Figure 4.12. From the inviscid limit Mode I becomes stable with finite damping when $c_r < 1$ but Mode II becomes unstable when $c_r > 0$. Viscosity has destabilizing effect on the stability of supersonic Couette flow.
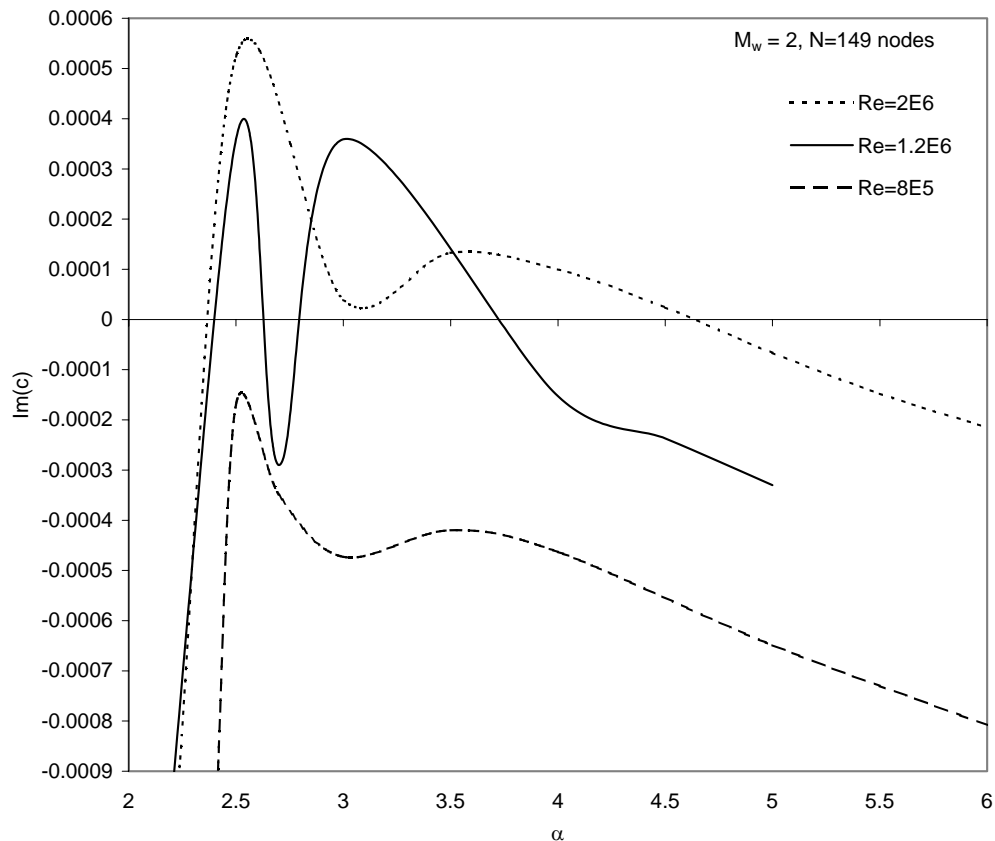

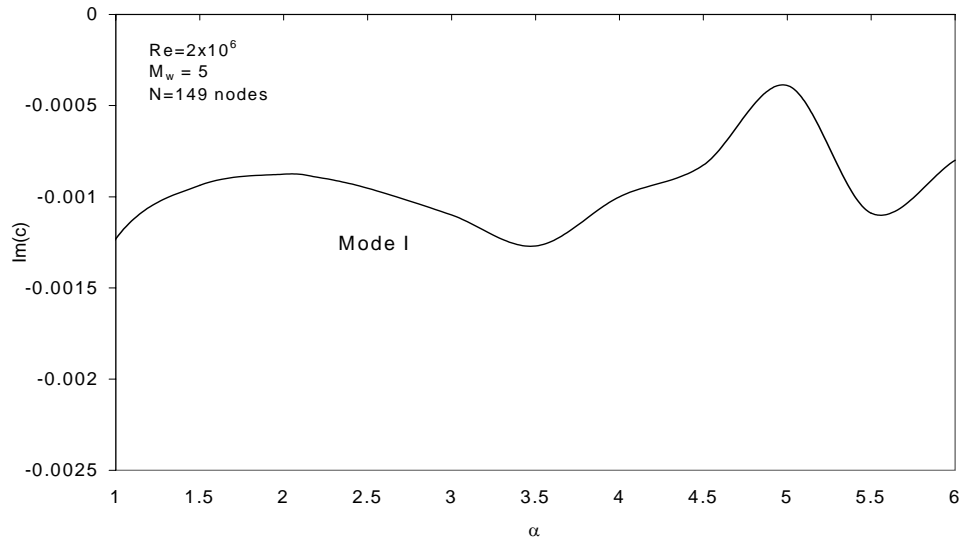Figure 4.12. c_i of Mode II as a function α at $M_w = 2$ at various Reynolds numbers

Figure 4.13. c_i of Mode I as a function of α at Mach 5

In Figures 4.10 and 4.11, c_i and c_r of Mode II at $M_w = 5$ and $\mathrm{Re} = 2x10^6$ are represented. Figure 4.11 also shows the behaviour of the flow for various Reynolds number. Finally, the trend of imaginary part of the eigenvalues of Mode I as a function of wave number, α, is shown Figure 4.13. The value of the c_i is always less than zero then the flow is always stable.

4.1.5. Neutral Stability Contours

Neutral stability contours are generated as a function of Reynolds number and wave numbers. Mode II is the most unstable mode among the others and dominates the instability of the compressible Couette flow.

Neutral stability contours of temporal amplification factors of Mode II is drawn at $M_w = 5$. Neutral stability curve represented as a line with $c_i = 0$. Figure 4.15 shows that there are two peaks and narrow peak is located around $\alpha = 2.5$ and wide peak is around $\alpha = 4$. Critical Reynolds number is around 780000 for $M_w = 5$.
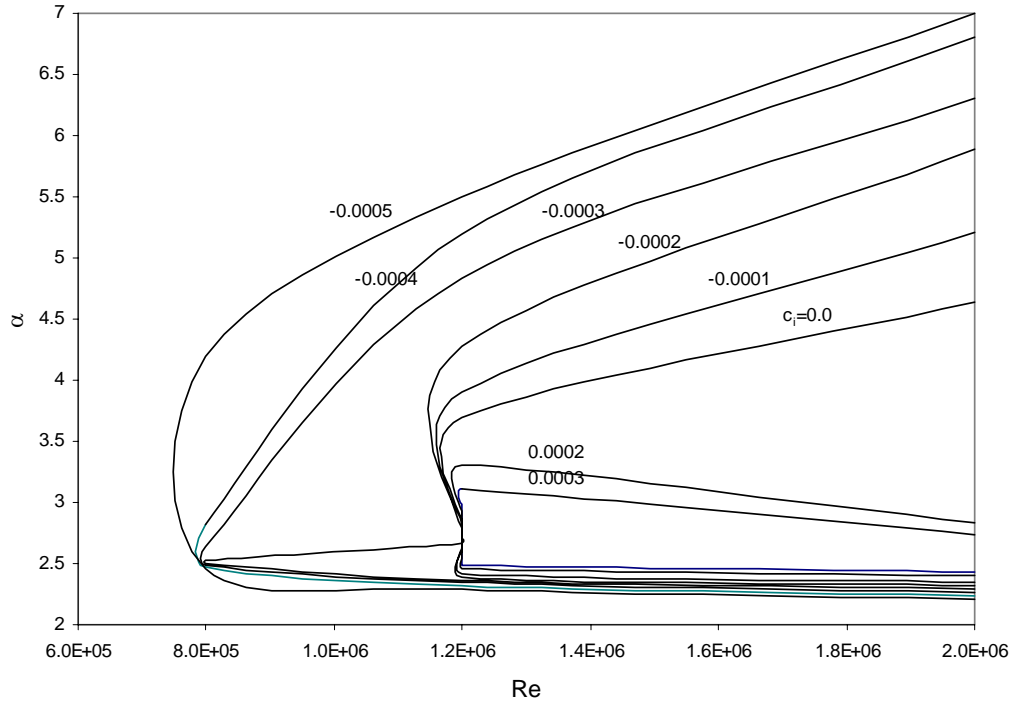
Figure 4.14. The contours of amplification factor for Mode II as a function of Reynolds number and wave numbers at $M_w = 5$
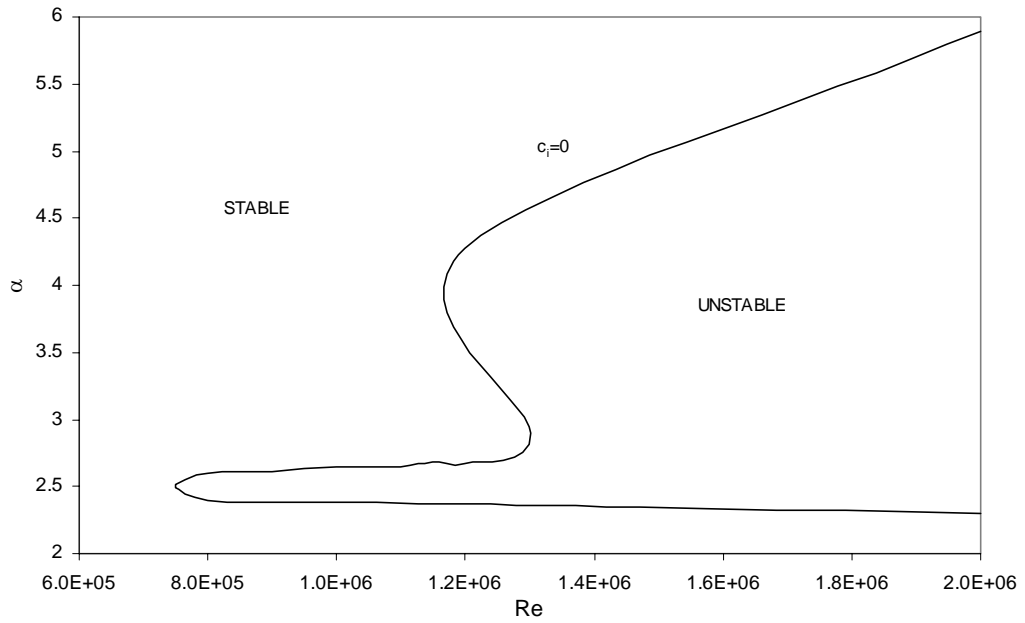

Figure 4.15. Neutral stability curve of Mode II as a function of Reynolds number and wave numbers at $M_w = 5$

Narrow peak at smaller α is due to viscous instability where as wide peak at larger α is due to the inviscid instability for acoustic wave modes. As the Reynolds number increases, the amplification factor of first peak extends to the maximum value and then decreases as a result of viscous instability.

4.2. High Speed Plane Poiseuille Flow

Orzsag [24] has solved the Orr-Sommerfeld equation numerically using the expansions in Chebyshev polynomials and QR matrix eigenvalue algorithm. He applied the method to the stability of plane Poiseuille flow and found the critical Reynolds number. The stability problem they studied is that of plane Poiseuille flow in a channel and measured all lengths in units of the half-width of the channel and velocities in units of the undisturbed stream velocity at the centre of the channel. The flow is incompressible and the flow Mach number is close to zero.

The Orr-Sommerfeld equation employed for stability analysis is the 4th order viscous incompressible analogy of our set of equations used. It is convenient to make comparison for the most unstable mode of plane Poiseuille flow with $\alpha = 1$ and $\mathrm{Re} = 10000$. Orszag found the most unstable eigenvalue as

$$c = c_r + ic_i == 0.23752649 + i0.00373967$$

and the critical Reynolds number and wave numbers are found as

$$\mathrm{Re}_{cr} = 5772,22$$
$$\alpha_{cr} = 1.02056$$

The critical Reynolds number that Orszag [24] found is based on the maximum channel velocity and half of the channel height. The critical Reynolds number, Re_{cr}, is defined as the smallest value of Re for which an unstable eigenmode exists.

64

In this study, the critical Reynolds number has been determined for instability of plane Couette-Poiseuille flow using the second order finite difference method. To simulate the plane Poiseuille flow, upper wall Mach number is taken close to the zero, $M_w = 0.0001$ and the flow is fully developed. The most unstable mode for $\alpha = 1.02056$ and $Re = 10000$ is shown on the Figure 4. 16 and numerical values are
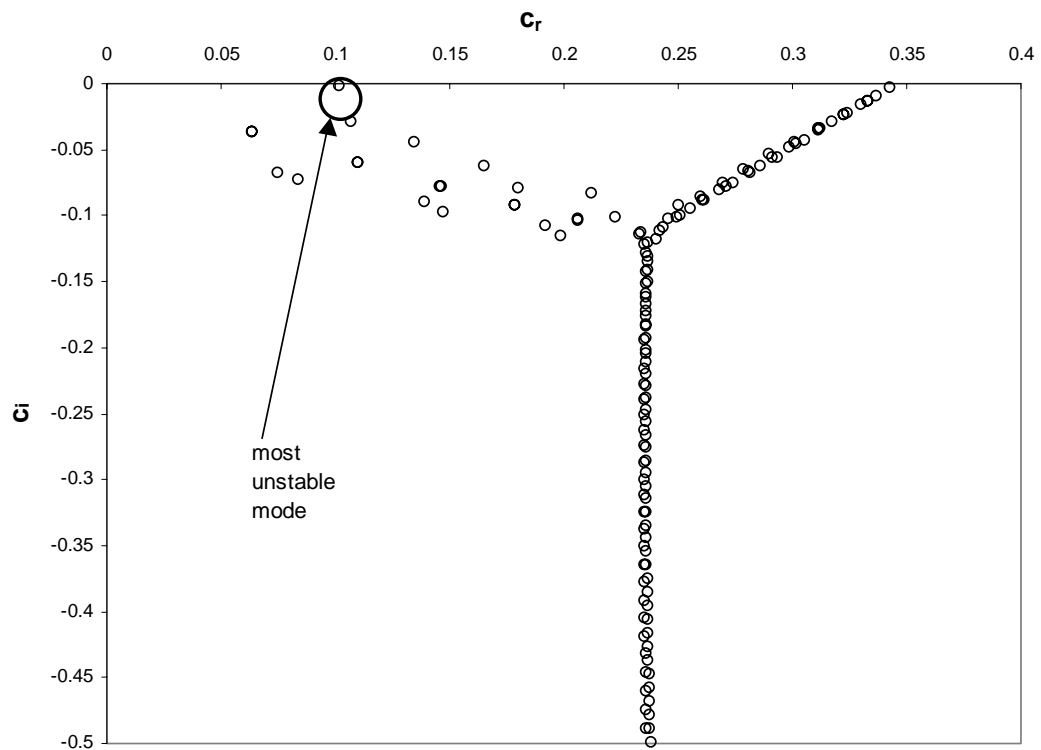
$$c = c_r + ic_i == 0,1017976 - i0,0018456$$

Figure 4.16. The most unstable eigenvalue for $M_w = 0.0001$, $Re = 10000$ and $\alpha_{cr} = 1.02056$ based on the maximum channel velocity and half width.

Compared to the Orzsag's value, the most unstable eigenvalue for that case is not same but the order of magnitude is same. The reason of having not exactly the same value is equations used to solve the problem for both basic flow and stability analysis.

There is a 12% difference of basic velocity and temperature profile in a channel compared to the incompressible situation. This difference makes the most unstable eigenvalue vary. The most interesting thing is the critical Reynolds number which is obtained through high speed equations nearly the same.

In Figure 4.17, the dispersion of critical Re numbers according to the wall Mach numbers is shown for various grid sizes. Results of grids of 249 and 299 are nearly the same and find that the critical Reynolds number is $\text{Re}_{cr} = 5718.338$ for the 249 computational grids throughout the channel height.
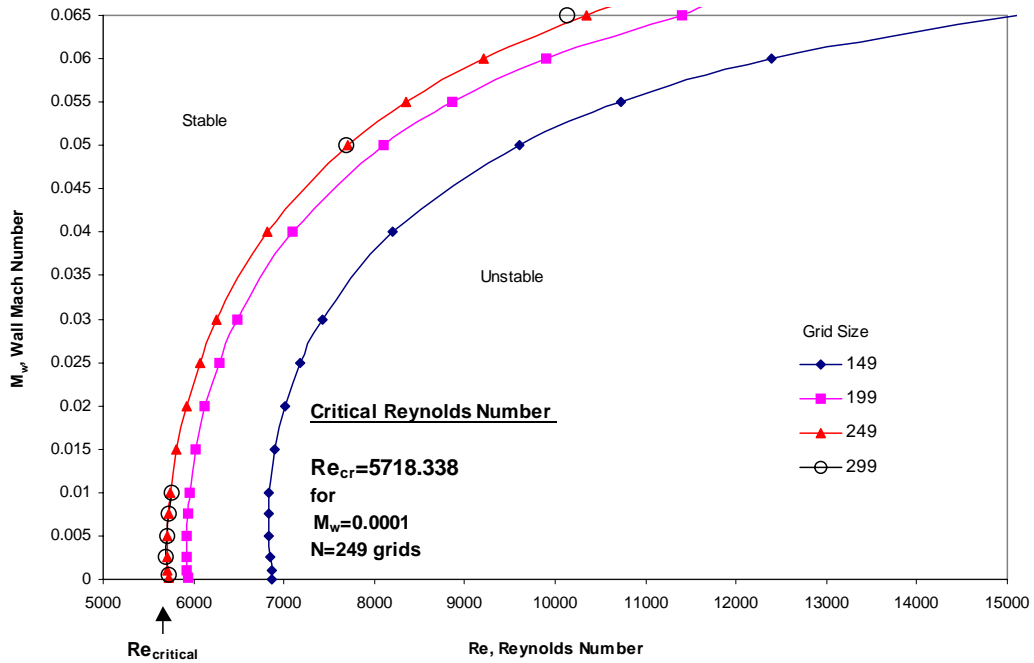

Figure 4. 17 Critical Reynolds numbers for wall Mach numbers for various grid sizes

The grids of 149 and 199 show the poor convergence to the results and that shows the code developed is grid sensitive. For high speed plane Poiseuille flow, the limit of the wall Mach number employed is $M_w < 0.065$.

CHAPTER 5

COMBINED PLANE COUETTE-POISEUILLE FLOW

5.1. General Description of Basic Flow

The flow geometry of the problem is the piston ring end gap and is simplified to Cartesian 2-D coordinates. The dimensions of the gap is 500 microns in height and 2 mm in length and shown in Figure 5.1. The depth of the gap is not taken into account for 2-D problem. The pressure inside the combustion chamber while compression cycle is approximately 50 bars and the pressure other side, crankcase is 3 bars. The pressure difference coupled with the high speed gas flow constitute the Couette-Poiseuille flow inside the gap. The flow is named as "high speed" flow not categorized as "compressible" since the effect of compressibility in the flow is not dominant.
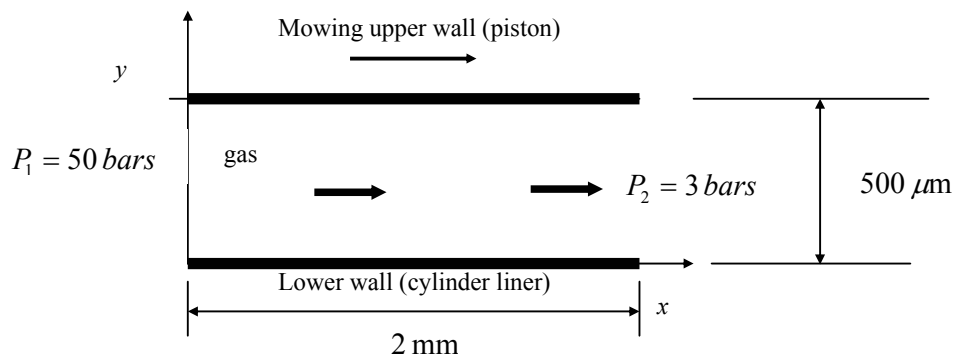

Figure 5.1.Geometry, dimensions and pressure values at channel inlet and outlet

The maximum speed of the piston is $15 \, m/s$ (average is $8 \, m/s$) in an ICE and the speed of gas particles is zero at stationary wall which is the cylinder liner in the current problem. Then the piston speed is not employed as a scaling velocity for the nondimensionalisation of the problem. The flow is to be choked due to high pressure ratio across the channel. Therefore, the appropriate scaling velocity is the sonic velocity encountered in the middle of the channel.

Flow passage has a rectangular cross-section and for a gas flow, the maximum flow rate per unit area has importance for the effect of "choking". Choking of the flow is not required but temperature and velocity of the gas coupled with a pressure gradient makes the choking is inevitable. The various effects causing choking are presence of heat transfer from the boundaries, adiabatic wall condition, channel width and high pressure ratio across the flow passage. In Figure 5.2 the schematic representation of the gas flow path and the geometry thereof are shown. The pressure of the gas is decreasing along the axial direction. All the mean flow calculations are based on the sonic velocity encountered in the middle of the channel.
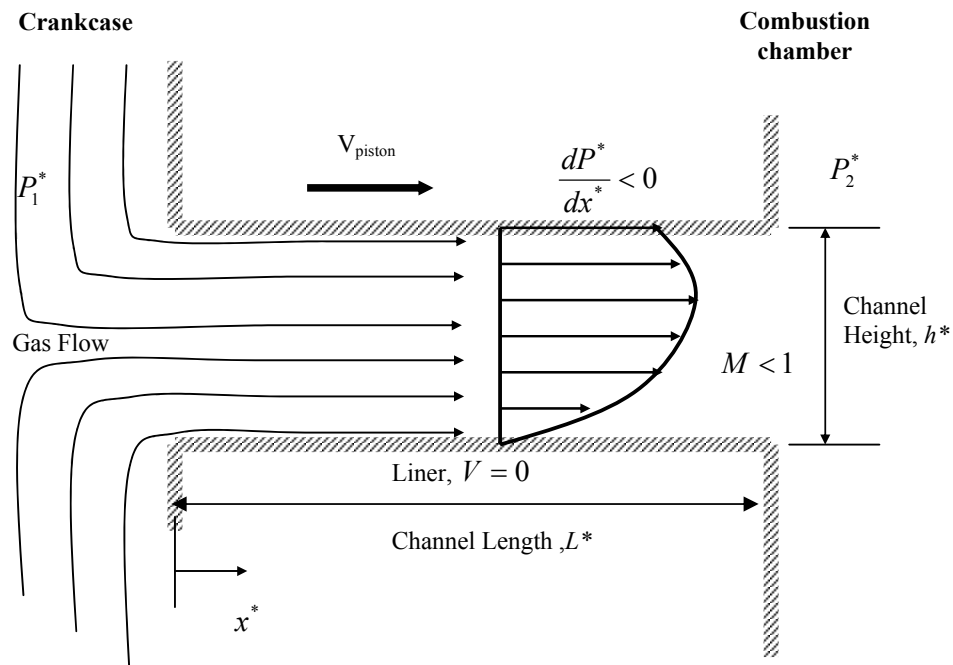

Figure 5.2. Motion of gas through the ring gap

For the Re number across the channel mean velocity is to be used. One has to integrate the mean mass flow rate passing through the flow crossection per unit depth and obtain the value of $\overline{\rho_o^* U_o^*}$ to be used for the Re number as

$$\overline{\dot{m}} = \overline{\rho_o^* U_o^*} A_{ch}^* = \int_0^{h^*} (\rho_o^* U_o^* dy^*) W_{ch}^* \qquad (5.1)$$

$$\frac{\overline{\dot{m}}}{W_{ch}^*} = \overline{\rho_o^* U_o^*} h^* = \int_0^{h^*} \rho_o^* U_o^* dy^* \qquad (5.2)$$

$$\overline{\rho_o^* U_o^*} = \frac{\displaystyle\int_0^{h^*} \rho_o^* U_o^* dy^*}{h^*} \qquad (5.3)$$

$$Re = \frac{\overline{\rho_o^* U_o^*} h^*}{\mu_\infty^*} = \frac{\displaystyle\int_0^{h^*} \rho_o^* U_o^* dy^*}{\mu_\infty^*} \qquad (5.4)$$

5.2. Basic Flow Solutions

The code developed for the basic flow solutions calculates the channel height and pressure gradient across the channel for a given upper wall Mach number and Reynolds number to reach the sonic velocity in the middle of the channel. The convergence to the sonic velocity requires hundreds to thousands of iterations.

While calculating the sonic velocity in the middle of the channel; temperature, kinematic viscosity and thermal conductivity are solved simultaneously with the velocity due to compressible and viscous mean flow equations employed. Pressure across the channel is decreasing, $\frac{dP}{dx} < 0$ and recalculated at every step of mean flow solution to satisfy the sonic velocity in the channel.
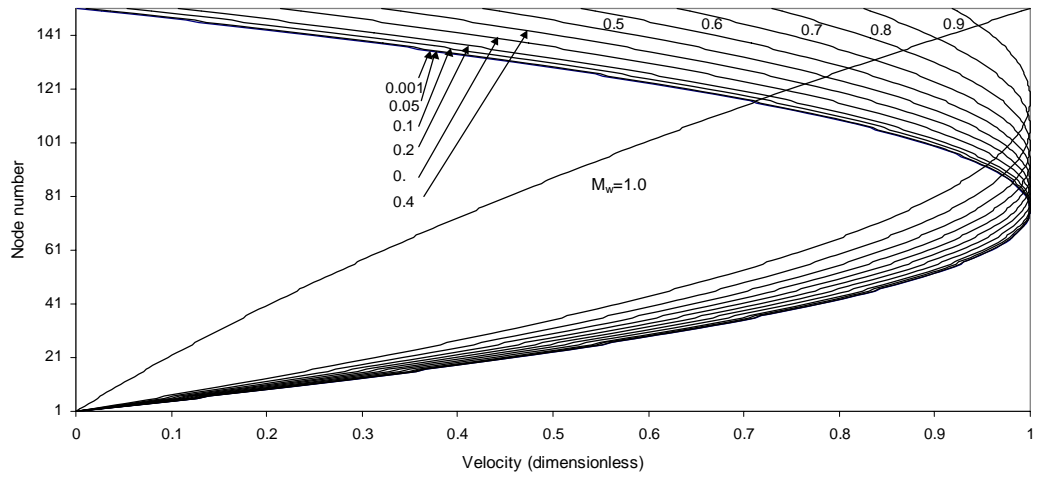
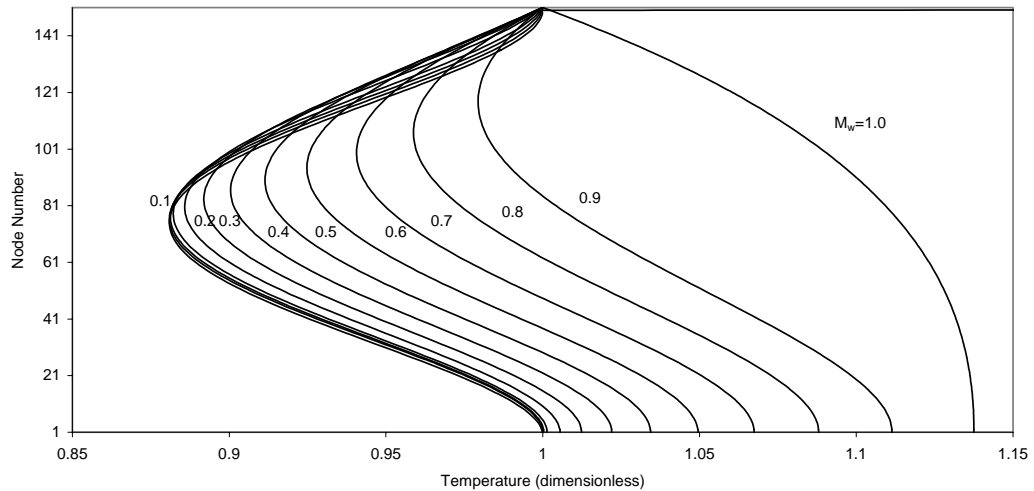Figure 5.3. Couette-Poiseuille velocity profile in the channel for various upper wall velocities at Re=125000

Figure 5.4. Couette-Poiseuille temperature profile in the channel for various upper wall velocities at Re=125000

Figures 5.3 to 5.5 show the mean flow solutions for the upper wall Mach numbers of $M_w = 0.001, 0.01, 0.05, 0.1$ and 1.0 at Re=125000. In these figures, it is seen that at

$M_w = 1.0$, mean flow resembles plane Couette flow. For $M_w = 0.001$, flow is Poiseuille and the velocity profile is parabolic. Both upper and lower walls are equal to the adiabatic lower wall temperature.
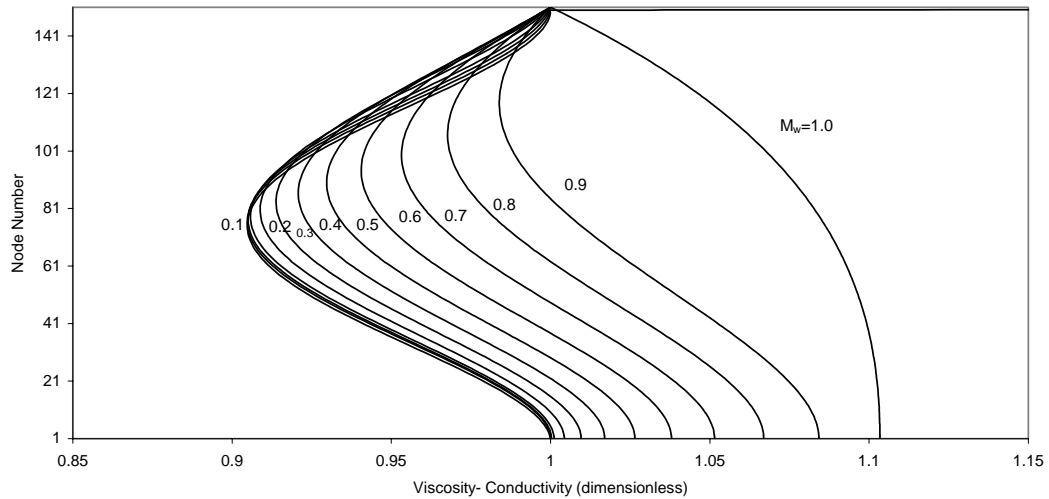

Figure 5.5. Couette-Poiseuille viscosity and conductivity profile in the channel for various upper wall velocities at Re = 125000

Across the 2 mm. gap length, the pressure ratio is approximately $235x10^7 \, Pa/m$ concerning the pressure in crankcase and behind the gap as 50 bars and 3 bars, respectively. This amount of pressure drop is not permitted across the channel as it is seen from the Figure 5.7 for the Reynolds number at 125000.

For the mean flow thermal conductivity of the gas in the flow field taken as equal to the reference kinematic viscosity. Prandtl number is evaluated at the reference upper wall conditions and $Pr \leq 1$ for gas. Then dimensionless mean specific heat at constant pressure, c_p, is constant for gas. The equality, $k_o = \mu_o$, is assumed in mean flow calculations.

Figure 5.6 shows the channel height calculated after satisfying the sonic velocity encountered in the middle of channel according to the given wall Mach numbers for upper wall.
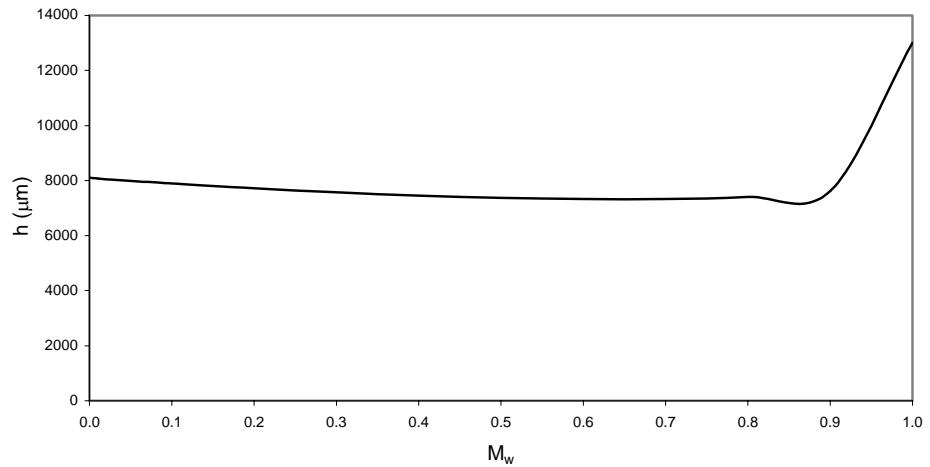

Figure 5.6. The calculated channel height for maximum Mach number for choked flow in according to upper wall Mach number given for Re = 125000.

Figure 5.7 shows the Reynolds number with respect to wall Mach number. The calculated Re number is substituted into the eigenvalue solution matrices.
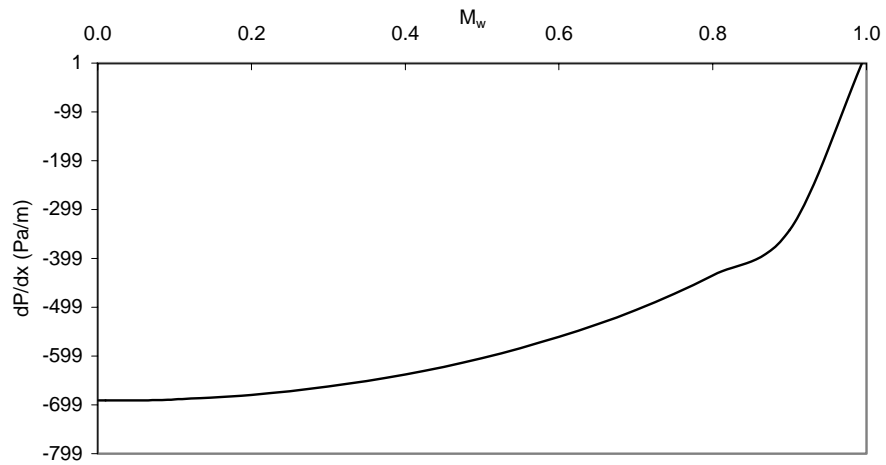

Figure 5.7. The calculated pressure drop in the channel for maximum Mach number for choked flow according to upper wall Mach number given for Re = 125.000
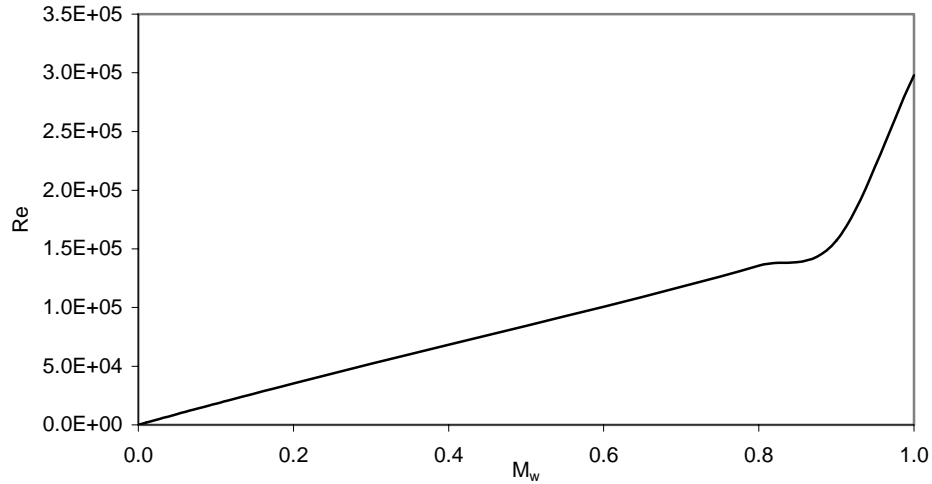
Figure 5.8. The Re number extracted after the calculation of the flow and used in stability equations according to upper wall Mach number given for Re = 125000

5.3. Eigenvalue Spectra and Neutral Stability for Plane Couette-Poiseuille Flow

Generating the mean solution for a plane Couette-Poiseuille flow and fixing the flow parameters which are the basis for the stability analysis such as channel height, Reynolds number, pressure drop across the channel, the generalized eigenvalue problem is solved using the method previously described.

An incompressible plane Poiseuille flow in the literature is to be validated by employing the upper wall Mach number in the incompressible limit for the present plane Couette-Poiseuille flow.

The dominant variable that determines and controls the flow stability is the wave number in streamwise direction, α and wavenumber in spanwise direction, β. The term β is zero for two-dimensional flows. The QZ algorithm is employed as a solution method of generalized matrix eigenvalue problem for determination of eigenvalues as functions of Reynolds number, wave number, and wall Mach number.
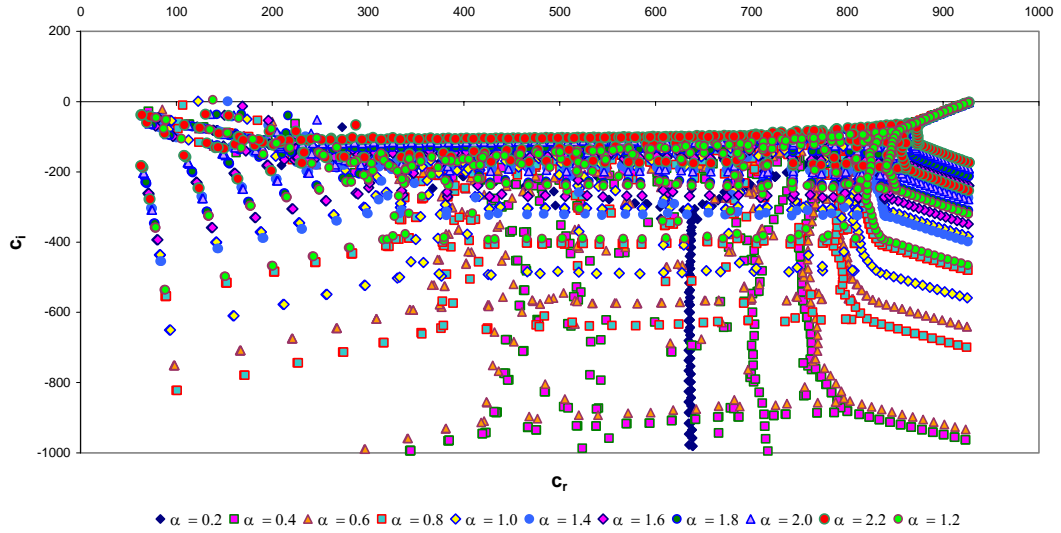
Figure 5.9. Eigenvalue spectra for M_w=0.001 and Re=125000 for a range of α=0.2-2.0

Figure 5.9 indicates the whole eigenvalue spectra for real and imaginary parts of c_r and c_i, respectively. The eigenvalues located in the circle in Figure 5.9 are the most unstable eigenvalues that dominates the behaviour of the flow stability and moving by wave number changes.

The eigenvalues circled in Figure 5.9 are shown in Figure 5.10 in enlarged view moving as the wave number changes and reveals the characteristics of the most unstable mode and the flow stability according to wave number. In Couette-Poiseuille flow, there are no acoustics modes as in the plane Couette flow which exhibits high flow speed at supersonic ranges.

The most unstable mode followed in Figure 5.10 is distinct from the odd (Mode I, III, V..) and even (Mode II, IV, VI...) modes for supersonic plane Couette flows. The most unstable mode followed lies always in a region of $c_r > 0$ enhancing the flow instability.
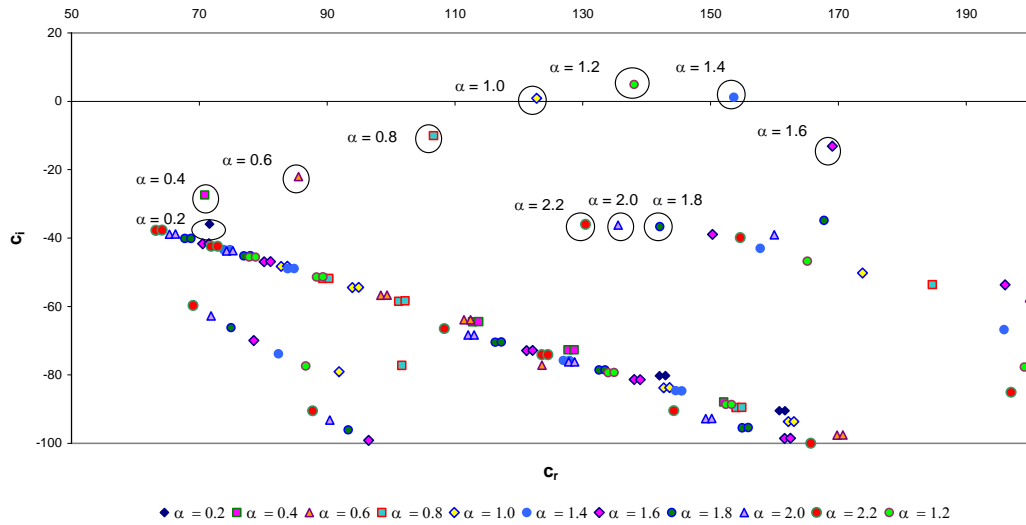
Figure 5.10. Local eigenvalue spectra near the neutral stability line for $M_w=0.001$ and Re=125000 for a range of α=0.2-2.0

In general, when it is inspected there are four branches on "Y" shaped distributions in the Figure 5.9. Those are due to viscous effects of the momentum (3 off) and energy equations. For the wave numbers around 0.2, the eigenvalue spectra is in "Y" shape and while the wave number increases the shape of eigenvalue spectra changes to "H" shape producing more spurious eigenvalues located at the lower braches.

5.4. Critical Reynolds Number Search

The global QZ algorithm is used for searching the eigenvalues. Global eigenvalue searching is an expensive method of computation. In addition to the global method, the local method determines the most unstable mode and finds the initial neutral point on the stability contour at any branch. The calculations are then followed on the neutral contour until the gradient of the curve changes sign through the nose. At the tip, there is a smallest Reynolds number for which an unstable eigenvalue exists.

The most unstable mode is the mode that gives valuable information about the flow characteristics and stability condition. Figure 5.10 shows the behaviour of the most unstable mode that is followed as a function of wave number, α, while keeping the upper wall Mach number, M_w and Reynolds number, Re, as constant.

The most unstable eigenvalue is located on the $c_r - c_i$ map and its c_i value is closest the c_r axis. The location of the eigenvalue and the value of the closeness to the c_r axis only changes with wavenumber and Reynolds number, Re, at a fixed upper wall Mach number, M_w

The procedure is based on the secant method for finding the root of an equation and sketched in Figure 5.11. It starts with the solution of the generalized eigenvalue problem employing the initially estimated Re number generating the most unstable eigenvalue for a constant wave number and Mach number.

In the second step, initially estimated Reynolds number is infinitesimally perturbed keeping the wave number and the Mach numbers are as constant and the most unstable mode is evaluated.

At that point, the Secant method is used between the two sets of Reynolds number being estimated and perturbed and their calculated c_i values of the most unstable modes to find the an improved estimate for the Re number at the root. The improved estimate for the Reynolds number is then substituted as the initial estimate in the following iterative step and the same procedure continues until the convergence of the c_i value is established. The c_i lines are set to $c_i = 0$, $c_i > 0$ and $c_i < 0$, for the neutral, unstable and stable regions to fix on the $\alpha - $ Re map at the interior or exterior of the contours at any constant c_i.
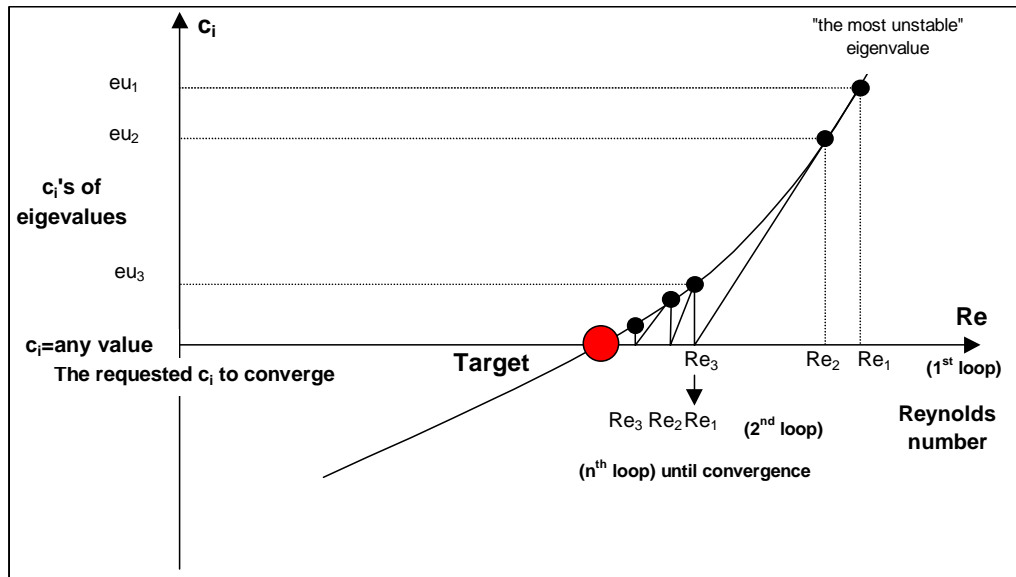
Figure 5.11. Secant method used finding the root of function

At that point, the Secant method is used between the two sets of Reynolds number being estimated and perturbed and their calculated c_i values of the most unstable modes to find the an improved estimate for the Re number at the root. The improved estimate for the Reynolds number is then substituted as the initial estimate in the following iterative step and the same procedure continues until the convergence of the c_i value is established. The c_i lines are set to $c_i = 0$, $c_i > 0$ and $c_i < 0$, for the neutral, unstable and stable regions to fix on the $\alpha - \mathrm{Re}$ map at the interior or exterior of the contours at any constant c_i.

Stability contours are based on the variation of Reynolds number, Re, and α, wave number, at a constant c_i. A scheme is developed to find the path of converged eigenvalues at constant c_i's on the $\alpha - \mathrm{Re}$ map at a fixed wall Mach number.

The stability contour has two branches, upper and lower, and their connection is at the tip of the contour line. The Reynolds number at the tip of the contour yields the

smallest and critical Reynolds number beyond which the flow is unconditionally stable.
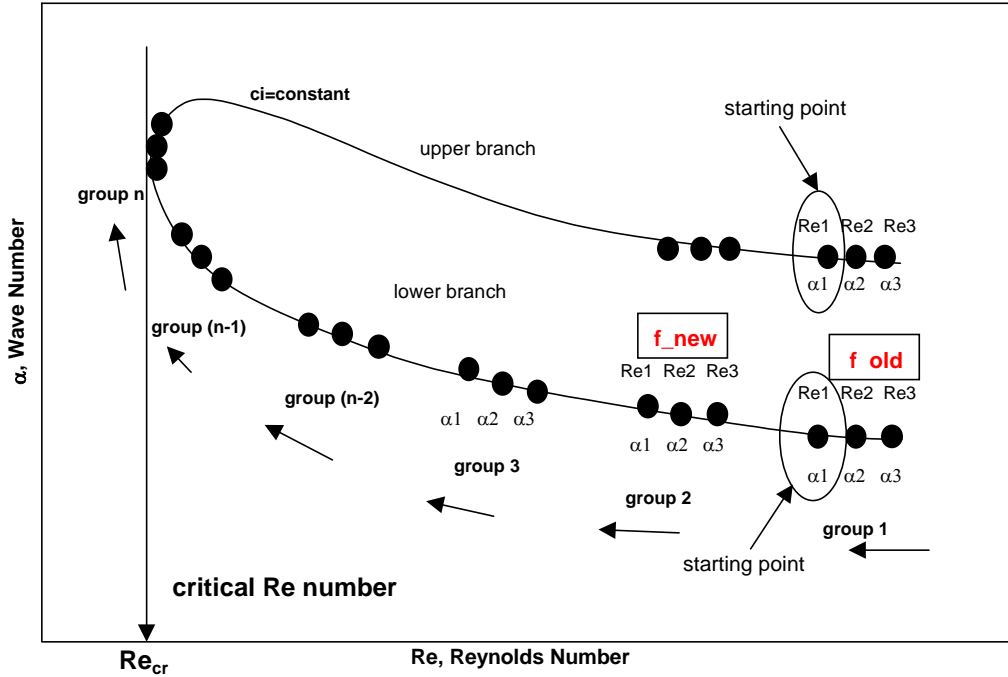

Figure 5.12. Schematic representation of stability contour search technique

Figure 5.12 exhibits the method to find the critical Reynolds number following the lower branch contour. At every point determination Secant root finding procedure is employed for Reynolds and wave numbers in the group. In every group, successive Reynolds and wave numbers are perturbed infinitesimally to obtain the local gradients between the $Re-\alpha$ pairs to reach $f(\alpha) = \dfrac{d\,\mathrm{Re}}{d\alpha} = 0$ at the tip of the contour. The local gradients, $f(\alpha)_{1-2} = \dfrac{d\,\mathrm{Re}}{d\alpha}|_{1-2}$ and $f(\alpha)_{2-3} = \dfrac{d\,\mathrm{Re}}{d\alpha}|_{2-3}$, of every successive points located in the same group are used to evaluate the overall group's gradient as

$$f(\alpha) = \frac{d\,\text{Re}}{d\alpha} = \frac{f(\alpha)_{1-2} - f(\alpha)_{2-3}}{\alpha_1 - \alpha_2} \qquad (5.5)$$

"group 1" gradient is employed in estimating the first point's wave number, α_{new}, in "group 2" in Equation (5.6) and "group 1" is then classified as "old".

$$\alpha_{new} = \alpha_{2_{old}} - \frac{f(\alpha)_{1-2}}{f(\alpha)} \qquad (5.6)$$

The term $\dfrac{(\alpha_{new} - \alpha_1)}{\alpha_1}$ is always checked after every group to continue or to stop the iteration for the evaluation of critical Reynolds number.

CHAPTER 6

RESULTS AND DISCUSSION

In this study of linear viscous stability characteristic of high speed Couette and combined Couette – Poiseuille flows have been investigated numerically. The effects of variable viscosity, temperature and density on the stability of Modes I and II for Couette flow and Mode 0 for Couette – Poiseuille flow were studied comparing the viscous results at finite Reynolds numbers with the results of Hu and Zhong [17] for plane Couette flow.

The physical problem is the instability of gas flow over a thin oil layer present in the internal combustion engine piston ring end gap. Although the flow across the end gap is the combined plane Couette – Poiseuille type, the plane Couette flow instability has already been studied for the code validation in Chapter IV. Plane Couette flow was found to be stable unconditionally for all Reynolds numbers under the sonic flow conditions, and the stability of the combined plane Coutte – Poiseuille flow is as a function of the Reynolds and wall Mach numbers is studied in the current Chapter.

6.1. Eigenmode Spectra

Using the global method, the unstable modes have been obtained for high speed Couette and combined plane Couette – Poiseuille flows. Among the unstable viscous modes, Mode II was found to be the dominant instability for high speed Couette flow.

The family of the most unstable eigenvalues are labeled as the odd modes (Modes I, III, V, etc) and the even modes (Modes II, IV, VI, etc) according to symmetric arrangement on the $c_r - c_i$ eigenvalue spectra for a plane Couette flow. These modes are acoustic instability modes and formed by sustained wave reflections between the walls and the relative sonic line for the supersonic flows (Hu and Zhong [17]).

Same labels are valid for the combined Couette – Poiseuille flow but those have no dominance on the instability of the flow. There is a dominant mode, labeled as "Mode 0" determining the instability of the flow. At first, Mode 0 seems to be a member of even modes. However, while the even modes are always stable at a wide range of flow parameters, Mode 0 varies between the stable and unstable regions under the same conditions. This inference makes the Mode 0 different than the even modes.

Although the flow that is investigated in the current study is a combined Couette-Poiseuille flow where the maximum Mach number in the flow field is unity, a similar pattern for the eigenvalue families were observed for the $c_r - c_i$ distribution. Figure 6.1 shows the distribution of all the eigenvalues for a given wave number $\alpha = 0.2$ and Reynolds number, Re=125.000. The even modes are located on the left side and the odd modes are located on the right side, in a symmetrical manner. Figures 6.2 and 6.3 also give a close up view of both modes. Mode II is the dominant mode in high speed Couette flow but for high speed Couette – Poiseuille flow the dominance of Mode II is not observed. As can be seen from Figures 6.1 - 6.3, Mode I and Mode II are always stable and no significant shift of those modes occurs while varying the wave number, α, as will be shown below.

The mode that is traced in the plane Couette-Poiseuille flow is named "Mode 0" and distinct from other known odd and even modes. Figure 6.3 shows Mode I, Mode II and Mode 0 on the eigenvalue spectra.

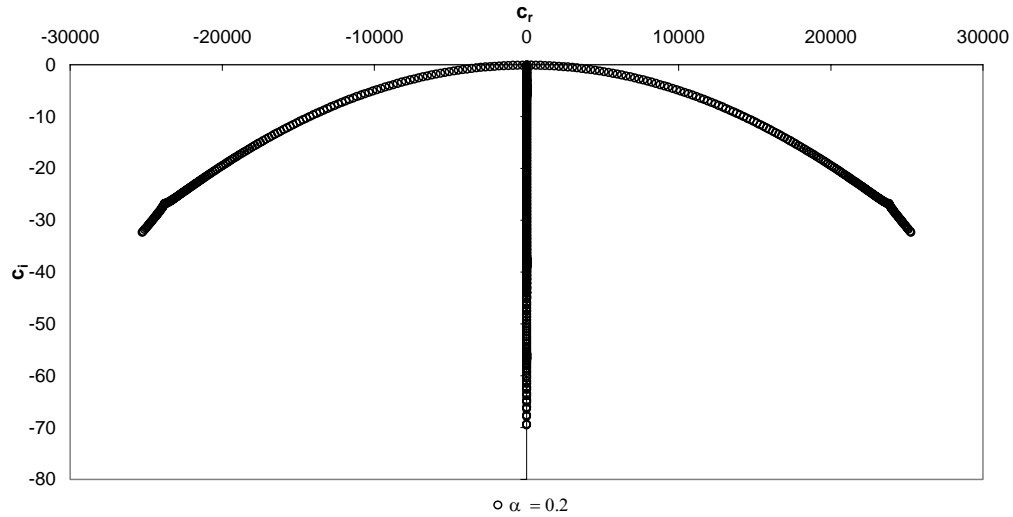Figure 6.1. Eigenvalue spectra at $M_w = 0.05$ for Re=125000 and $\alpha = 0.2$

Figure 6.4 shows the variation of Mode 0 as a function of wave number while Mode I and Mode II remain nearly stationary compared to Mode 0. This shows that Mode II is not the dominant mode that determines the stability characteristics of the flow in plane Couette – Poiseuille flow. Since both Modes I and II are acoustic modes, which are dominant for supersonic flows only, they are not dominant in case of the current study where the maximum velocity in the flow field is sonic.

The eigenvalue spectrum of $M_w = 0.1$ for Re= 15625000 and α=0.2, 1.0 and 2.6 displays an unexpected behavior especially at high wave numbers. At high Reynolds numbers and wave numbers, one of the branches of Mode I or Mode II eigenvalue spectrum overshoots in positive and negative directions in a symmetrical manner while Mode 0 remains at small wave numbers, $\alpha = 0.2$ and 1.0, and close to or above the c_r. This is given in Figure 6.5. At α=2.6 scattered eigenvalues above the $c_i = 0$ axis exhibits a behavior that seems spurious. If these modes are purely spurious a poıssibility exists that they may be cured by grid refinement. However, if these modes are genuine, then the eigenvalue which exhibits the highest c_i value is chosen as the most unstable eigenmode, *i.e.,* Mode 0.
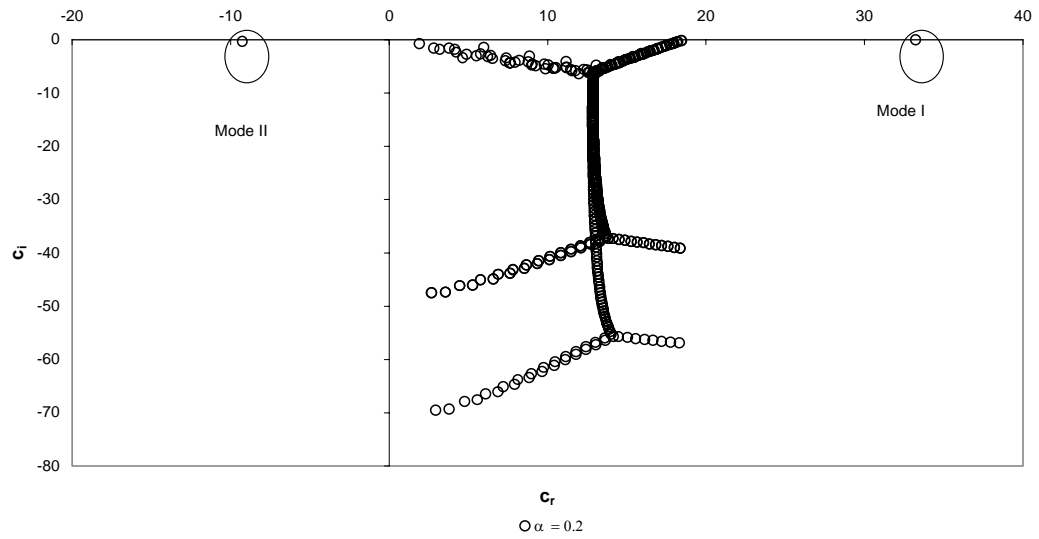
Figure 6.2. Eigenvalue spectra at $M_w = 0.05$ for Re=125000 and $\alpha = 0.2$ showing the odd and even modes

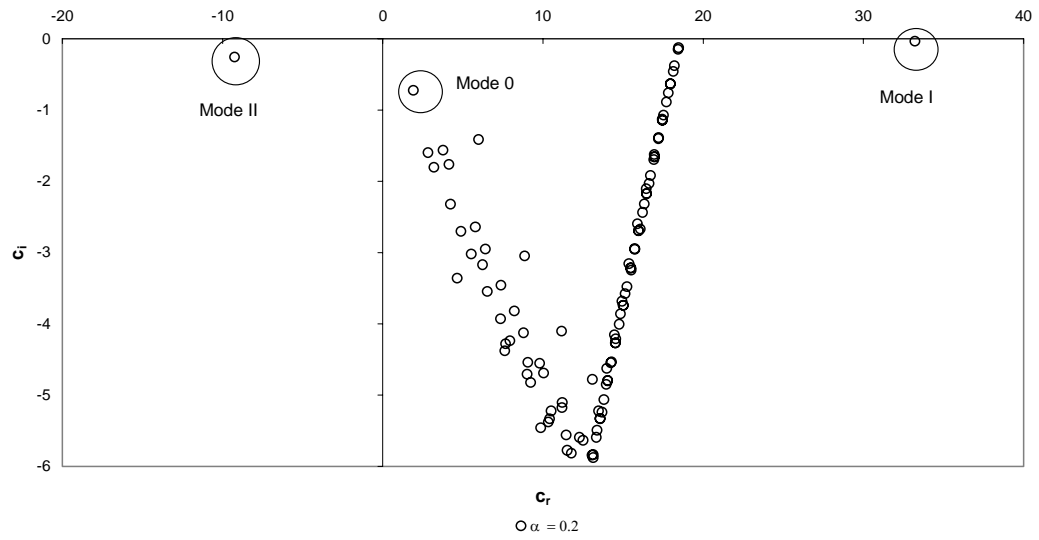
Figure 6.3. Eigenvalue spectra at $M_w = 0.05$ for Re=125000 and $\alpha = 0.2$ showing Mode I, Mode II and Mode 0

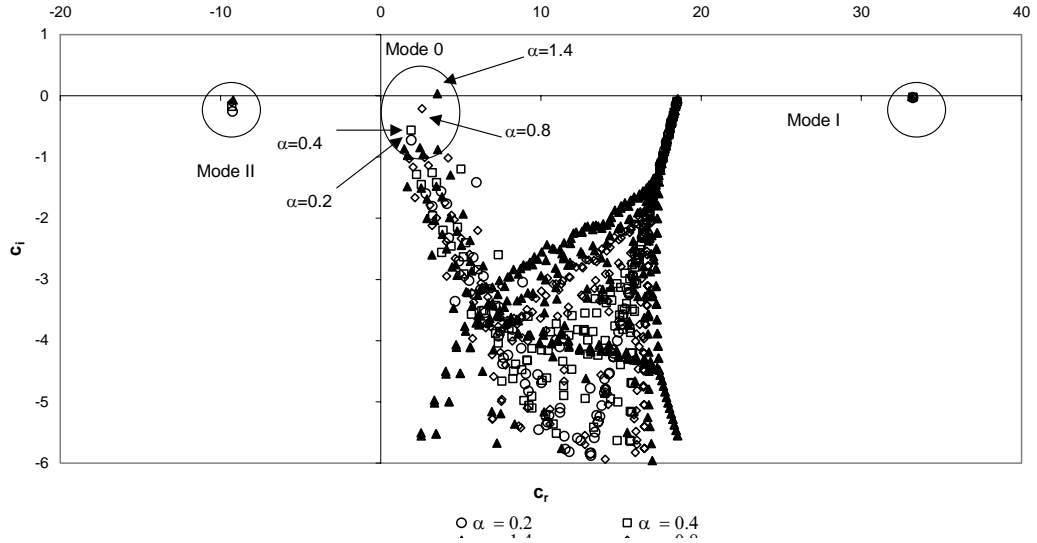Figure 6.4. Eigenvalue spectra at M_w = 0.05 for Re=125000 and α = 0.2, 0.4,0.8,1.4 showing Mode I, Mode II and Mode 0

In this study the global eigenvalue solution method, QZ algorithm, was used without employing any local method for higher accuracy. During code validation, high speed plane Couette flow was examined in the channel. Numerical code works at any Mach and Reynolds number.

In reference to Hu and Zhong [17] with supersonic flow conditions, the results are in good agreement with others as stated in Table 4.1 and 4.2 (Hu and Zhong [17] and Malik [14]). The difference of the results comes from the methods used for higher accuracy. Malik [14], Duck et al. [16] and Hu and Zhong [17] all use local methods in addition to the global methods to improve the results. For the subsonic flows treated here, the grid number was increased from 49 to 499 nodes which is the limitation of the memory of the currently used Fortran compiler. Increasing the grid number decreases the gap between the eigenvalue curves obtained for low grid numbers. But the convergence criteria of 10^{-10} has never been achieved between different grid numbers.
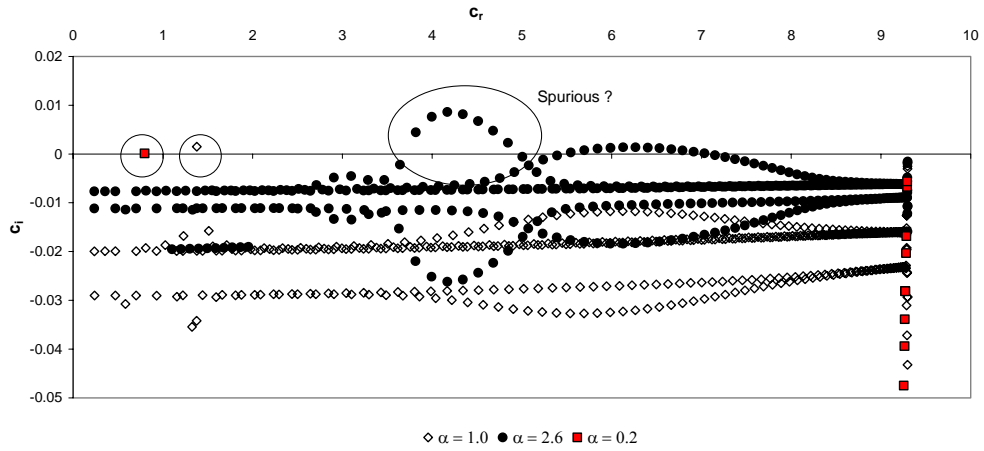
Figure 6.5. Eigenvalue spectra at $M_w = 0.1$ for Re=15 625 000 and $\alpha = 0.2, 1.0$ and 2.6

6.2. Critical Reynolds Number

The critical Reynolds number was determined for plane Couette-Poiseuille flow using the second order finite difference method. The critical Reynolds number, Re_{cr} is defined as the smallest value of Reynolds number for which an unstable eigenmode exists. The investigation of critical Reynolds numbers and determination of the stable – unstable regions on the $M_w - Re$ map were generated working on a range of Mach numbers between 0.0001 to 1.0.

Figure 6.6 shows that the critical Reynolds number converges to a value of $Re_{cr} = 5718.338$ for $M_w = 0.0001$ using the 249 interior grid points. This corresponds to the fully Poiseuille case.
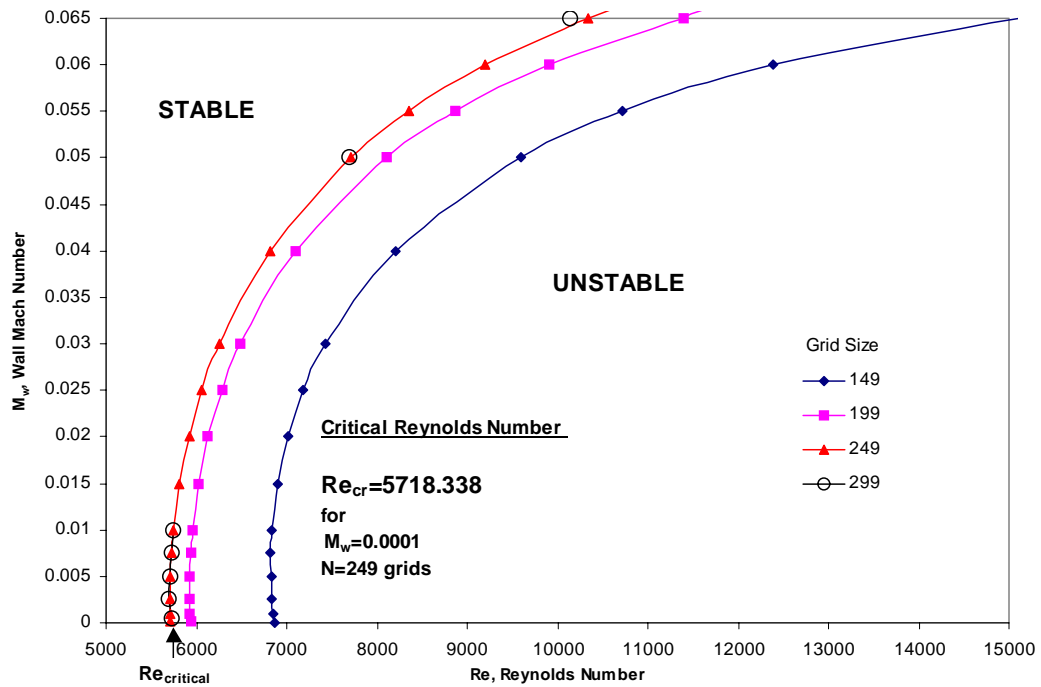
Figure 6.6. $M_w - \mathrm{Re}$ contours showing the grid sensitivity and the critical Re number at low wall Mach numbers

The effect of the grid points on the results is that increasing the number of grid points beyond 249 has no significant effect on the critical Reynolds number. Therefore, the number of the grid points used for the neutral stability contour analysis was taken as 249. The wall Mach number shown in Figure 6.6 is 0.065 and the trend of the curves at various grid points is consistent. In Figures 6.7 and 6.8, for wall Mach numbers greater than 0.065, there exist an overshooting of the critical Reynolds number. The value of the Reynolds number at $M_w = 0.1$ is around $\mathrm{Re} = 35\,000\,000$ for 249 grid points.

The behavior of the results in the region of $M_w = 0.065 - 0.3$ is not meaningful. The results show a lot of scatter for all grid points used. It is not known if there are unexplained physical events or there exist a computational inadequacy within that Mach number range. When the Mach number is greater than 0.3, the behavior of the results on the map is more coherent for various grid points.

Figure 6.6 also shows the boundaries of the stable and unstable regions at a small range of Mach and Reynolds numbers. The curves shown correspond to neutrally stable conditions, i.e. $c_i = 0$. The regions remaining within the neutral curve show unstable configurations, while regions exterior to the curve are stable. Figures 6.7 and 6.8 display the general overview of the stability condition of the flow according to the grid points for Mach numbers up to, $M_w = 1.0$ investigated in this study for a plane Couette-Poiseuille flow.
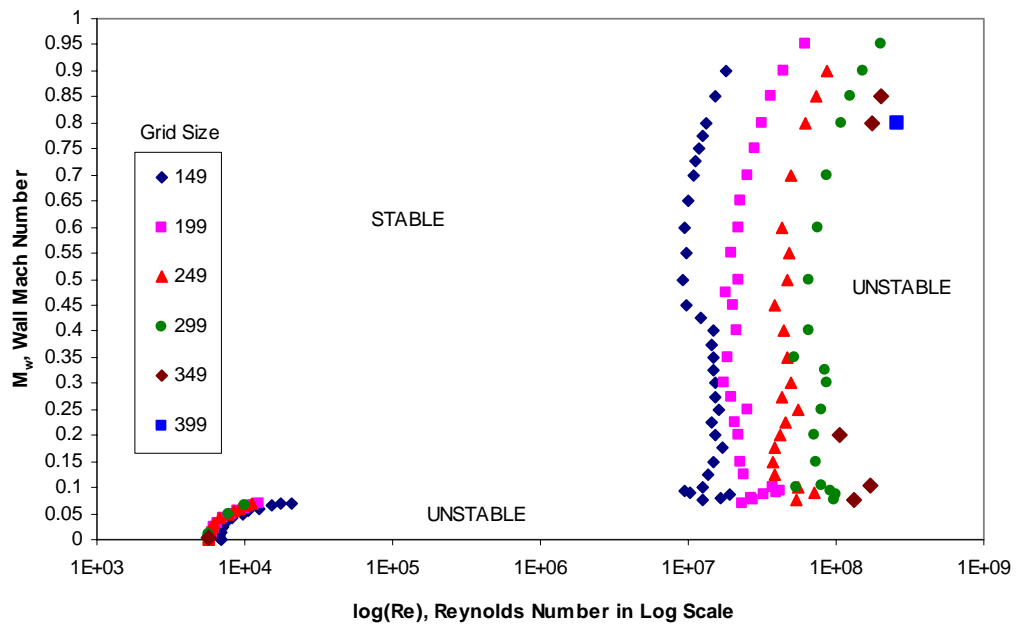

Figure 6.7. Stable and unstable regions for a wide range of M_w and Re for various grid points. (Re axis is in logarithmic scale)

Orszag [24] found the critical Reynolds number as 5772.22 for instability of incompressible viscous plane Poiseuille flow using Chebyshev Polynomials method for Orr – Sommerfeld equation.
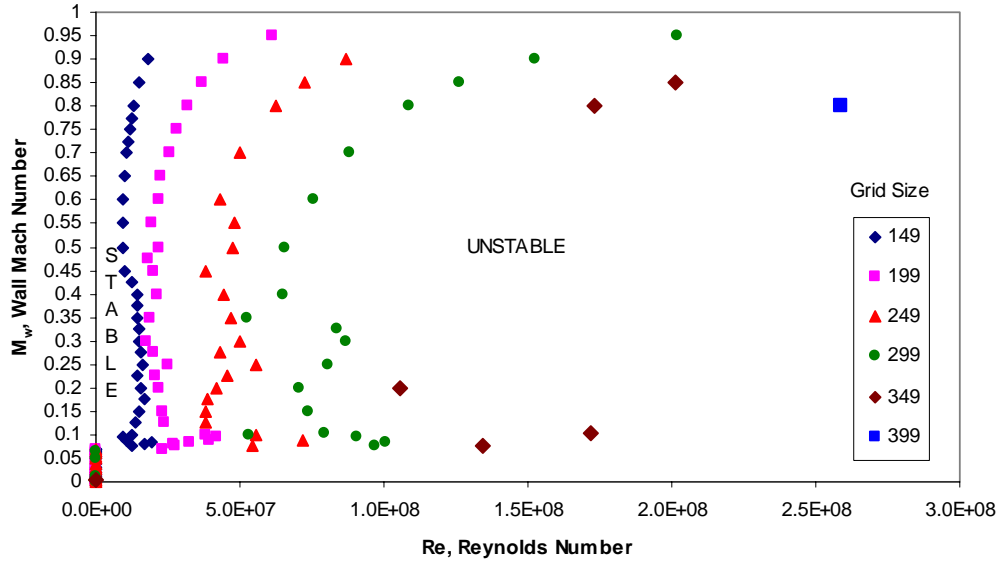

Figure 6.8. Stable and unstable regions for a wide range of M_w and Re for various grid points

Our result is in agreement with the result obtained by Orszag. Possible minor differences are due to solution method used and the differential equation solved. Remember that in this study, a set of high speed governing equations are solved simultaneously instead of Orr – Sommerfeld equation and $M_w = 0.0001$ is employed as an incompressible limit to validate the results.

6.3. Neutral Stability Contours

Inside the channel the maximum gas velocity is 400 m/s taking the gas temperature as 100^oC and the channel height as 500 μm. Using the velocity calculated and taking the dynamic viscosity of gas as 2.3x10^{-5}. m^2/s, the Reynolds number in the channel was calculated as 5000.

The rated average piston speed is 8 m/s and the speed of sound at the reference temperature is 340 m/s. Practically, upper wall velocity is the average piston speed which is basis for the upper wall Mach number and is approximately 0.0235.

Both the Reynolds and the upper wall Mach numbers draw the boundaries of the analysis for the instability analysis of the flow through the piston ring end gap. The Reynolds and the wall Mach number limits are extended widely to get more information although the flow conditions are around $Re = 5000$ and $M_w = 0.0235$.

Then, the flow was investigated and the stability contours were determined for a range of wall Mach numbers, $M_w \leq 0.065$, specifically at $M_w = 0.005$, 0.035 and 0.065. Similary, the range of Reynolds number is extended to $Re = 5000 - 70000$.

It is traditional to represent the eigenvalues by drawing contours in diagrams of wave number versus Reynolds number, $\alpha - Re$, and phase velocity versus Reynolds number, $c_r - Re$. Each contour represents a constant rate of amplification or a imaginary part of the complex wave velocity.

In this study neutral stability contours have been generated as functions of Reynolds number and wavenumbers, $\alpha - Re$. In these diagrams c_i is taken as constant equal to 0. The conditions where $c_i = 0$, $c_i < 0$ and $c_i > 0$ represent neutrally stable, stable with finite damping and unstable with finite amplification conditions, respectively. In general, the disturbance waves are three dimensional and two dimensional disturbance modes correspond to a special case of spanwise wave number as $\beta = 0$ due to Squirre transformation. In this study, the stability contours for dimensionless temporal amplification factor of $c_i = 0.0$, 0.0005, 0.0010, 0.0015, 0.0020, 0.0025 and 0.0030 are determined for defined sets of M_w and Re.
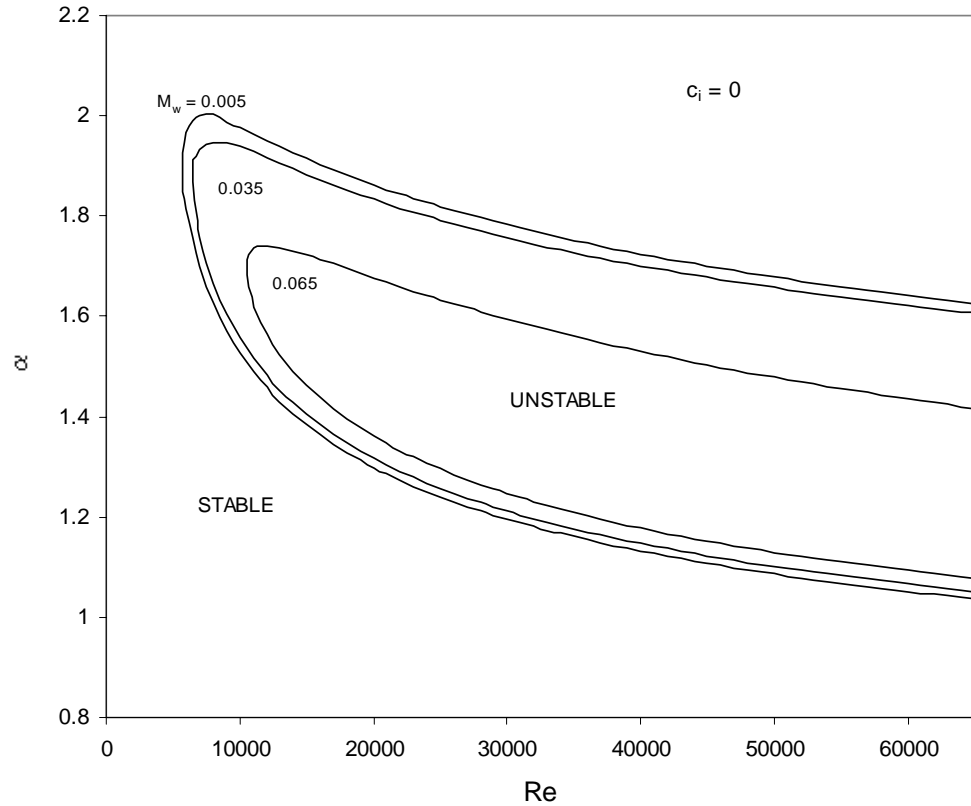
Figure 6.9. The neutral stability contours for mode 0 as functions of wavenumbers and Reynolds numbers at various M_w.

Figure 6.9 shows the neutral stability contours for a range of Mach numbers from 0.005 to 0.065. As the Mach number increases the upper branch of the contours move towards lower wave numbers while the lower branch stays nearly stationary. Also, the critical Reynolds numbers increase as the wall Mach number increases, hence the flow becomes more stable. Figure 6.9 indicates that there is a peak in c_i curves and this peak is located at $\alpha = 1.7$ for $M_w = 0.065$ and $\alpha = 2.0$ for $M_w = 0.005$. The curves are characteristic of viscous instability where the unstable wave numbers become less and less as the Reynolds number increases. There is no threshold value of the wavenumber at the upper branch below which all wavenumbers are unstable which is a characteristic of inviscid instability. This shows that the instability modes observed in this study are the viscous instability modes and not the acoustic or inviscid instability modes which are typically present in supersonic flows.

Figures 6.10 and 6.16 – 6.17 show the neutral stability contours for Mach numbers of 0.005, 0.035 and 0.065, respectively. In addition to the neutral stability contours, the contours at constant c_i are also indicated. As can be seen the maximum amplification factor decreases as M_w increase, where maximum c_i for $M_w = 0.065$ is only 1/3 of the maximum c_i for $M_w = 0.005$.
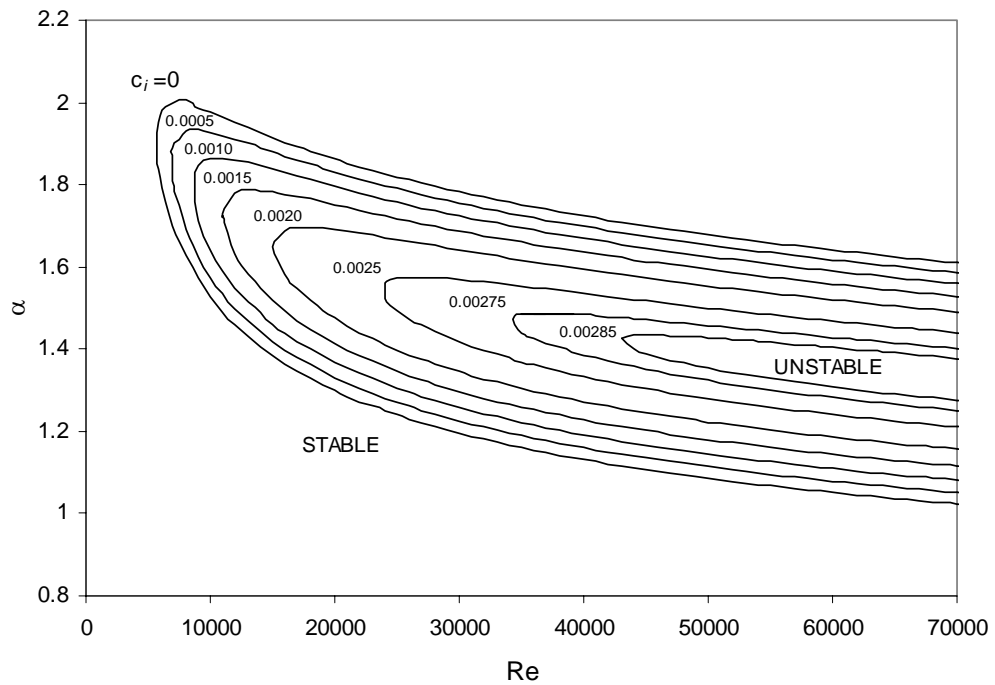

Figure 6.10. The contours of amplification factor, c_i, for Mode 0 as functions of wavenumbers and Reynolds numbers at $M_w = 0.005$

Figure 6.11 shows the distribution of amplification factor as a function of Reynolds numbers of fixed wavenumbers at $M_w = 0.005$. It indicates that the peaks would vanish as the Reynolds number increases. Figure 6.12 indicates the amplification factor distribution and the peaks disappear increasing the Reynolds numbers.
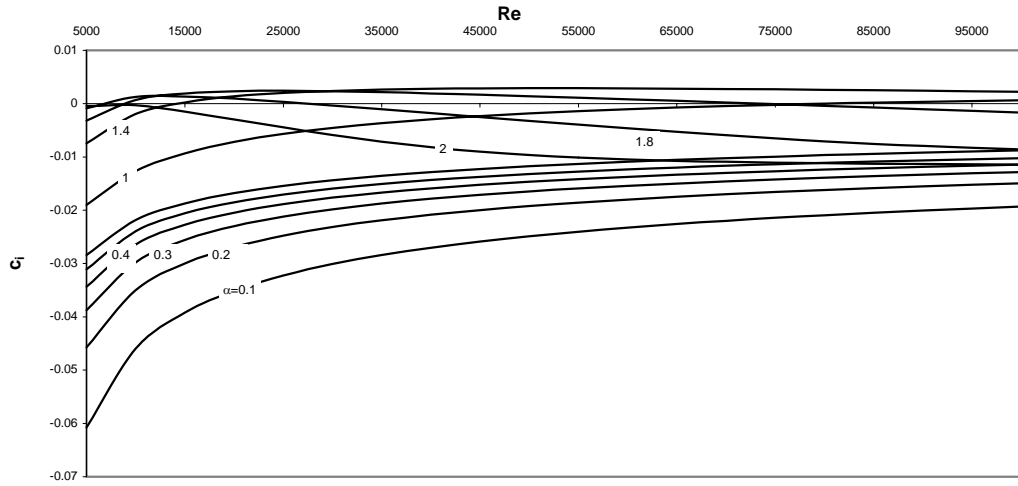
Figure 6.11. The distribution of amplification factor of Mode 0 as functions of Reynolds numbers at fixed wavenumbers for the case of $M_w = 0.005$
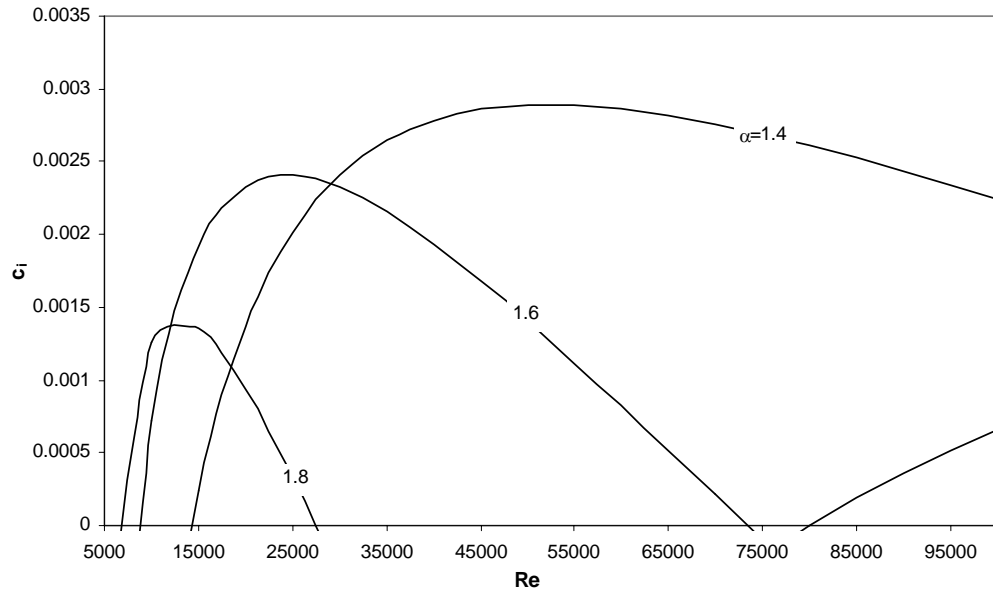

Figure 6.12. The distribution of amplification factor of Mode 0 as a function of Reynolds numbers at fixed wavenumbers for the case of $M_w = 0.005$
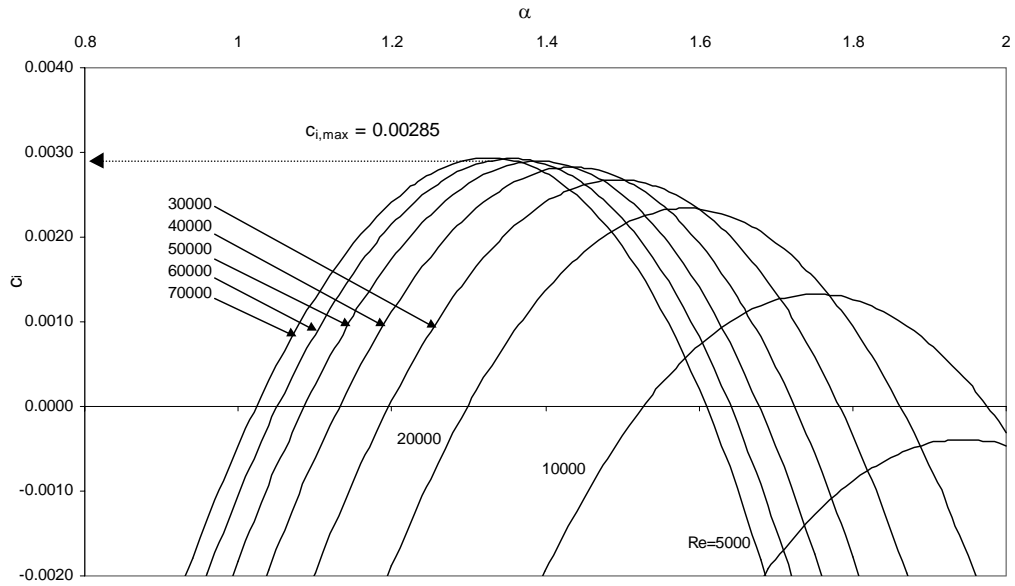
0.0040

$c_{i,max} = 0.00285$

0.0030

30000
40000
50000
60000
70000

0.0020

Ci

0.0010

0.0000

20000

10000

-0.0010

Re=5000

-0.0020

Figure 6.13 Amplification factor of Mode 0 as a function α at M_w = 0.005 for various Reynolds numbers

Figure 6.13 illustrates the distribution of amplification factor as a function of α at M_w = 0.005 for a range of Reynolds numbers. It indicates that increasing the Reynolds number further, amplification factor stays at around peak value of c_i =0.00285. At that c_i as seen in Figure 6.10, there is a stability contour line in the form of nearly closed curve if we further increase the Reynolds number range determining that viscous instability is dominant in the flow. In Figures 6.18 and 6.19, the behavior of amplification factor as functions of Reynolds and wave numbers at wall Mach numbers 0.035 and 0.065, respectively. At wall Mach number 0.065 for the amplification factor of c_i = 0.0009, there is a closed stability contour and if it is further increased to 0.000925, it results in wavy closed loop. Flow is unconditionally unstable for the values of c_i more than the peak value of 0.000925 at M_w = 0.065.

As the wall Mach number increases, the amplification factor, c_i, decreases concluding that there are no stability contours for the wall Mach numbers higher than 0.065 in a range of wave numbers, 0.1-2.0. The whole range of c_i including the stable phases, $c_i < 0$, can be seen in Figure 6.14 for $M_w = 0.005$ and Figures 6.22 and 6.23 for $M_w = 0.035$ and 0.065, respectively.

The distribution of wave speed, c_r, which is the real part of the eigenvalue of Mode 0 is seen in the Figure 6.15 for different Reynolds numbers. As the wavenumber increases first the wave speed decreases until $\alpha = 0.4$ then it increases until $\alpha = 0.9$ for Re = 95 000 and $\alpha = 1.6$ for Re = 5000. Then sudden and continuous decrease of the wave speeds with increasing wave number occurs for all Reynolds numbers. Figures 6.22 and 6.23 show the behavior of wave speed, c_r, for wall Mach numbers of 0.035 and 0.065 as functions of wave and Reynolds numbers.
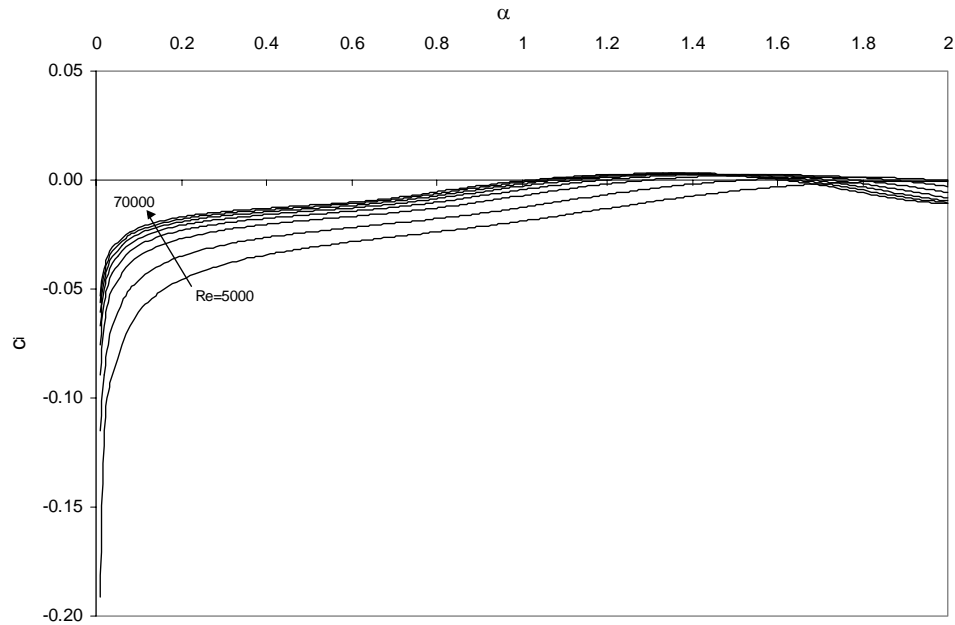

Figure 6.14. All ranges of temporal amplification factor of Mode 0 as a function α at $M_w = 0.005$ for various Reynolds numbers
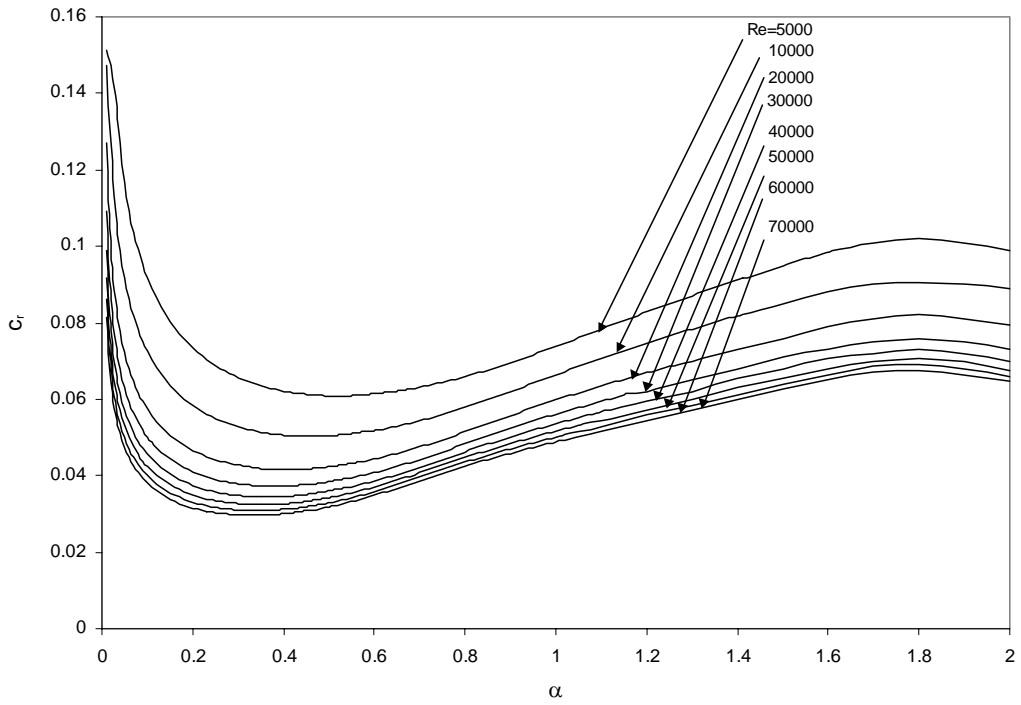
Figure 6.15. Wave speed, c_r, of Mode 0 as a function of α at M_w =0.005 for different Reynolds numbers.
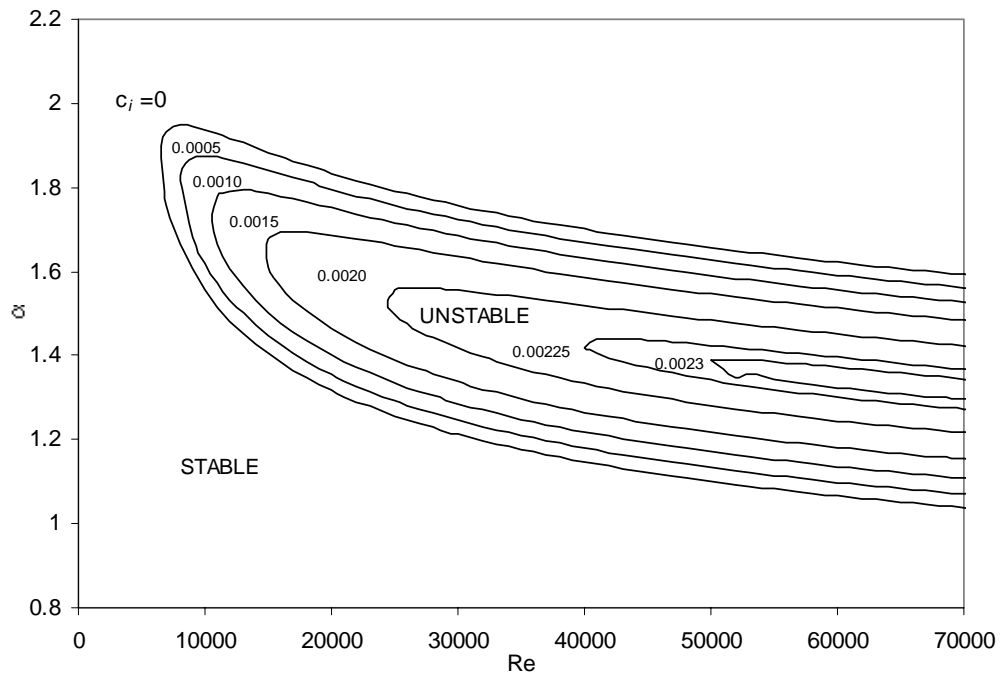

Figure 6.16. The contours of amplification factor, c_i, for Mode 0 as functions of wavenumbers and Reynolds numbers at M_w =0.035
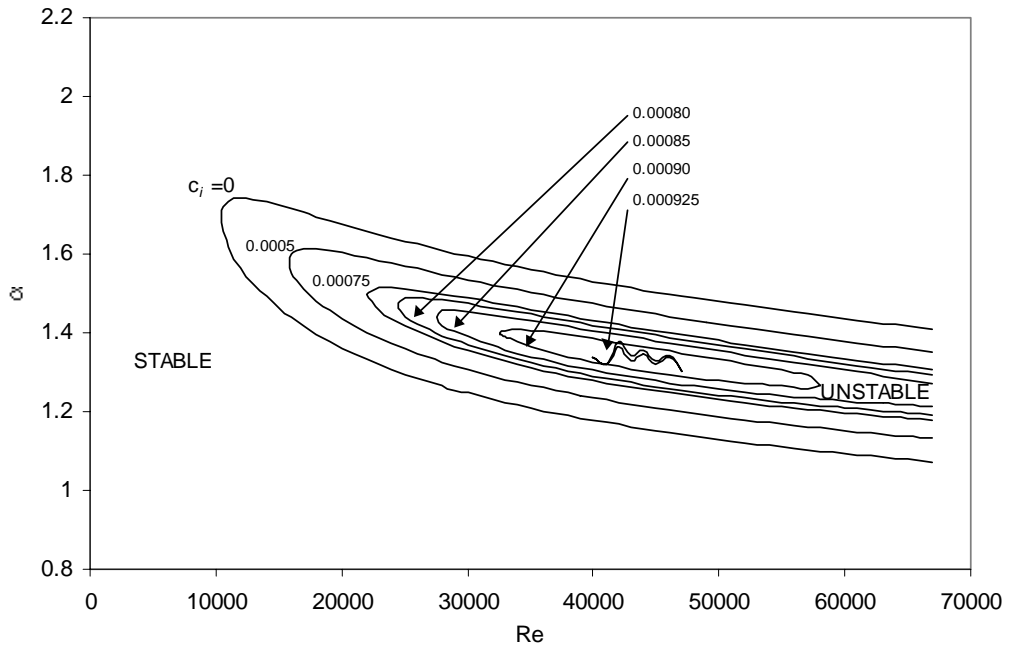
Figure 6.17. The contours of amplification factor, c_i, for Mode 0 as functions of wavenumbers and Reynolds numbers at $M_w = 0.065$
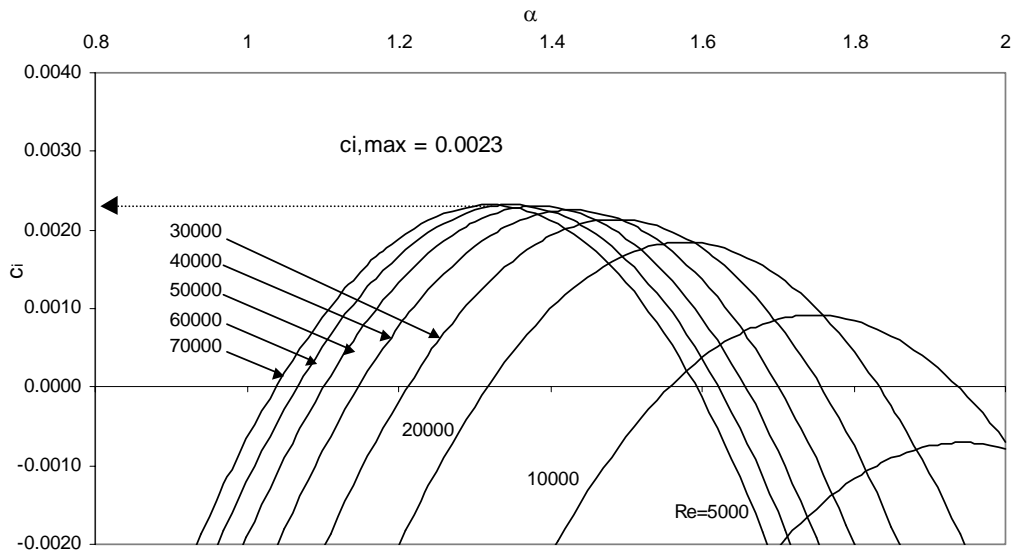

Figure 6.18. Amplification factor of Mode 0 as a function α at $M_w = 0.035$ for various Reynolds numbers
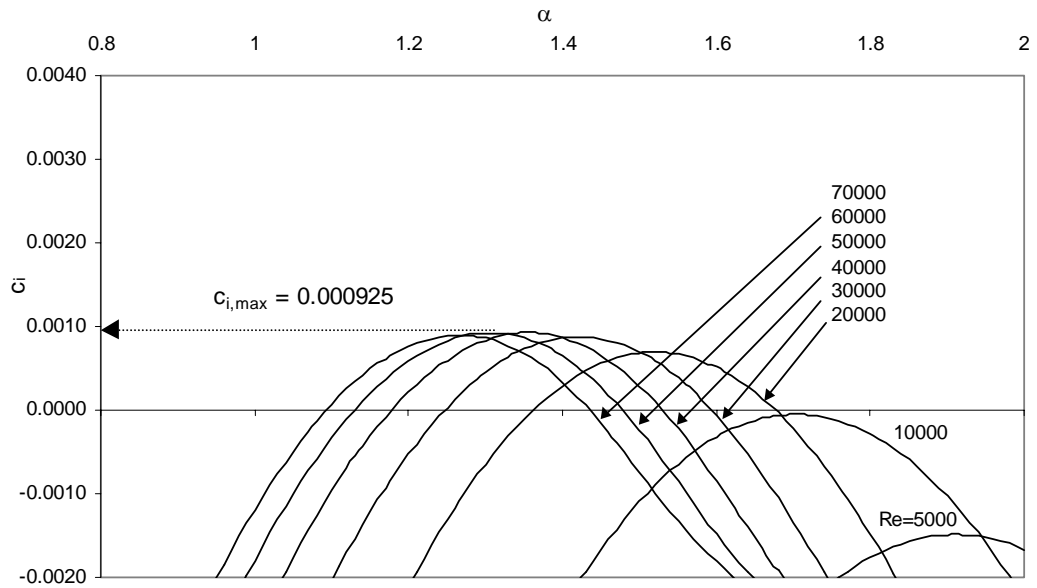
Figure 6.19. Amplification factor of Mode 0 as a function α at $M_w = 0.065$ for various Reynolds numbers
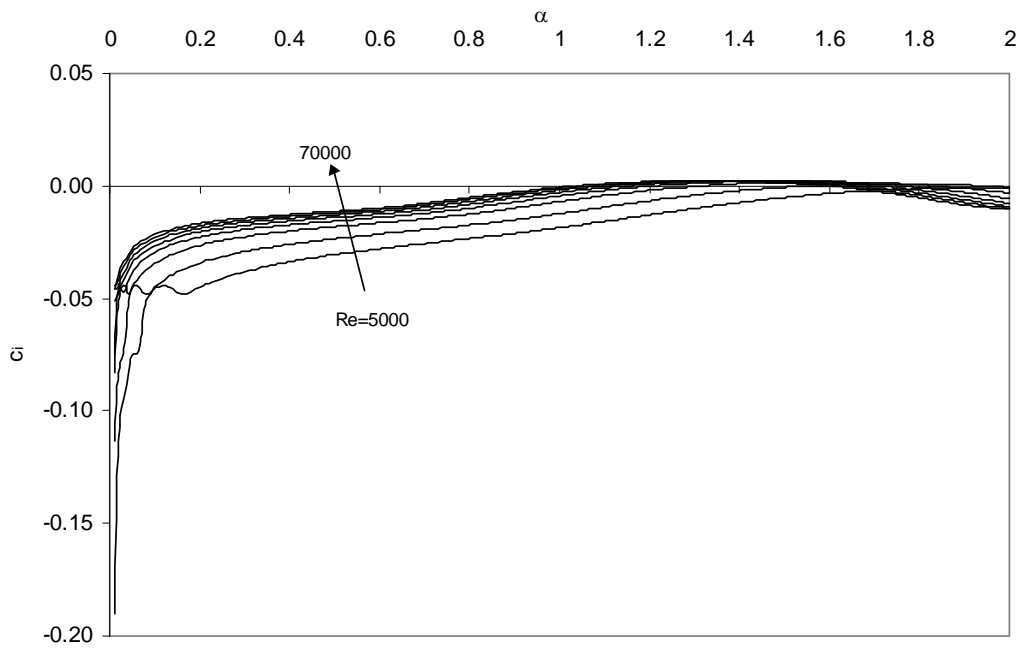

Figure 6.20. All ranges of amplification factor of Mode 0 as a function α at $M_w = 0.035$ for various Reynolds numbers
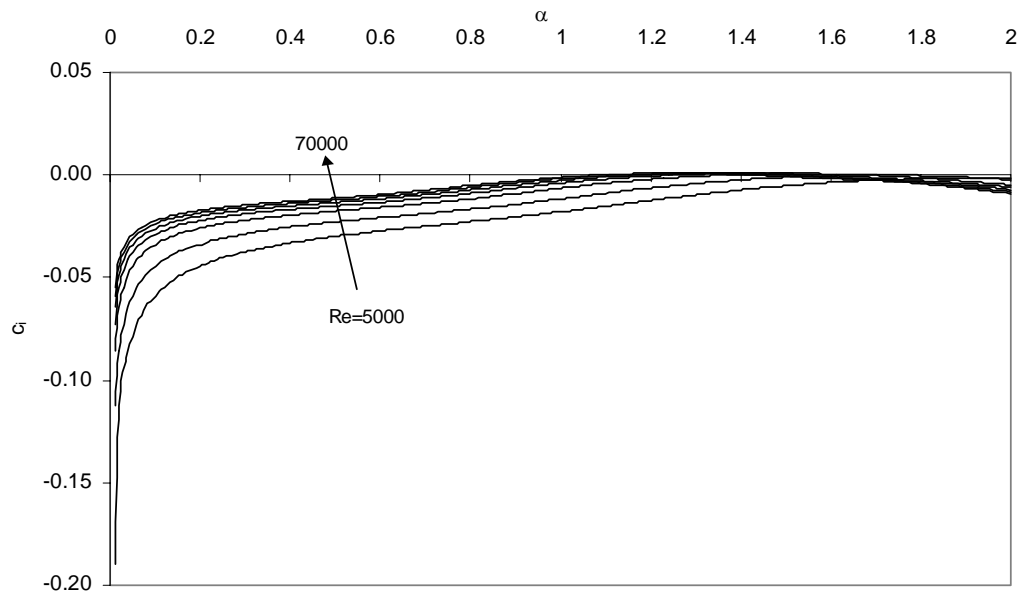
Figure 6.21. All ranges of amplification factor of Mode 0 as a function α at $M_w = 0.065$ for various Reynolds numbers
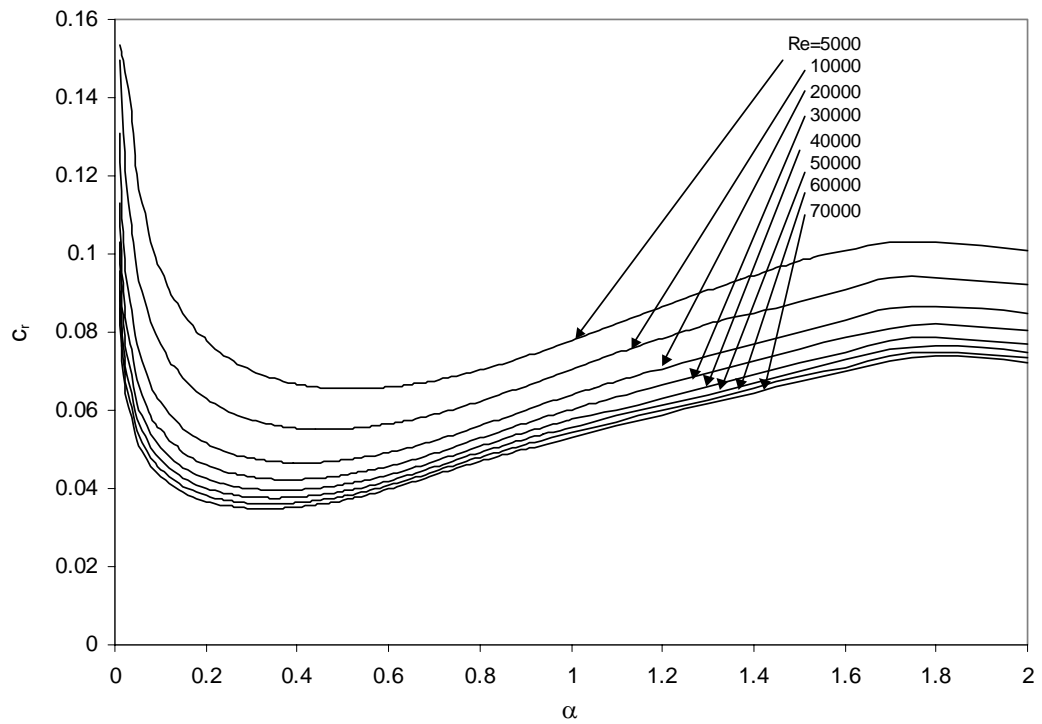

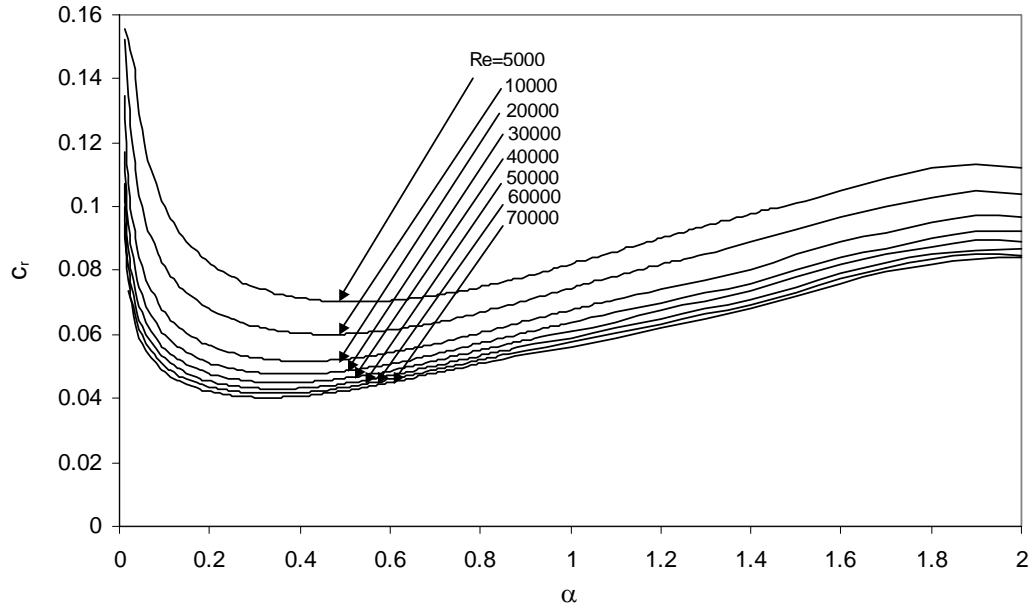Figure 6.22. Wave speed, c_r, of Mode 0 as a function of α at $M_w = 0.035$ for different Reynolds numbers

Figure 6.23. Wave speed, c_r, of Mode 0 as a function of α at $M_w = 0.065$ for different Reynolds numbers

6.4. Effect of Mach Number

Figure 6.24 shows the contours of amplification factor, c_i for the most unstable mode 0 for a range of Mach numbers and wave numbers while fixing Reynolds number at $Re = 30000$.

The unstable range for α decreases as the Mach number increases. The figure shows that, for a fixed Reynolds number, there is a Mach number which corresponds to the maximum amplification rate for mode 0. For a fixed Reynolds number at 30000, the most unstable Mach number is around 0.010.

Figure 6.25 shows mode 0 temporal amplification factor at $Re = 30000$ as a function of α for various Mach numbers. For a fixed Reynolds number at $Re = 30000$, as Mach number increases, the c_i first increases, reaches a maximum at certain Mach number, and then decreases. The Mach number corresponding to the maximum c_i at $Re = 30000$ is 0.005 which is in agreement with the above observations.
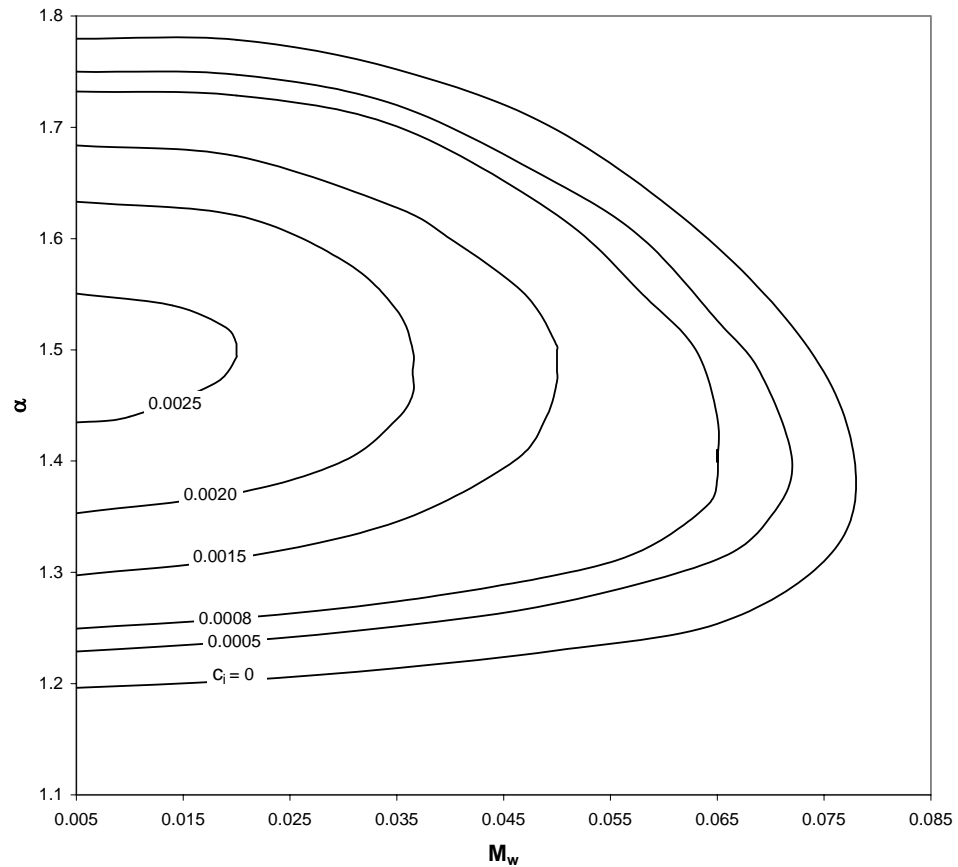
Figure 6.24. The contours of temporal amplification factor for most unstable Mode 0 as a function of α and M_w for Re = 30000.

Figure 6.26 shows the maximum phase velocity over a range of wavenumbers for a range of Mach numbers corresponding to mode 0 at Re = 30000. Same figure shows that Mode 0 instability is weakening as the Mach number increases. Increasing Reynolds number amplifies the instability and phase velocity increases. Mode 0 instability is the highest at $M_w = 0.005$. The curves indicate that before the Re=6000 regardless of M_w the flow is stable for every wavenumber.
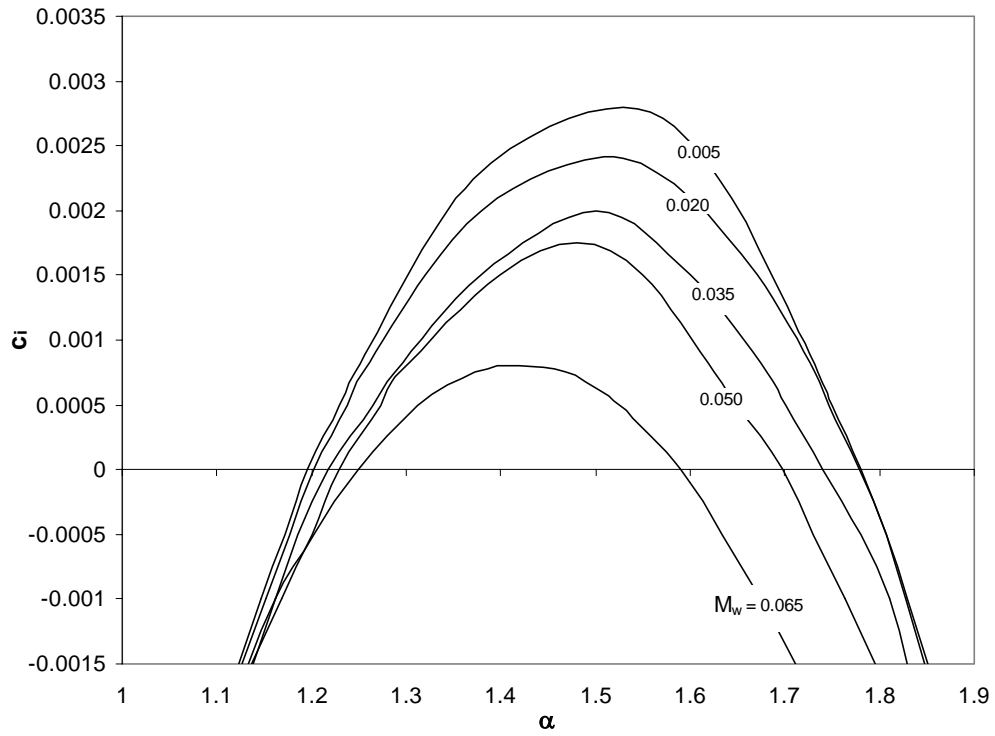
Figure 6.25. Mode 0 temporal amplification factor as a function of α at different Mach numbers for the case of $Re = 30000$
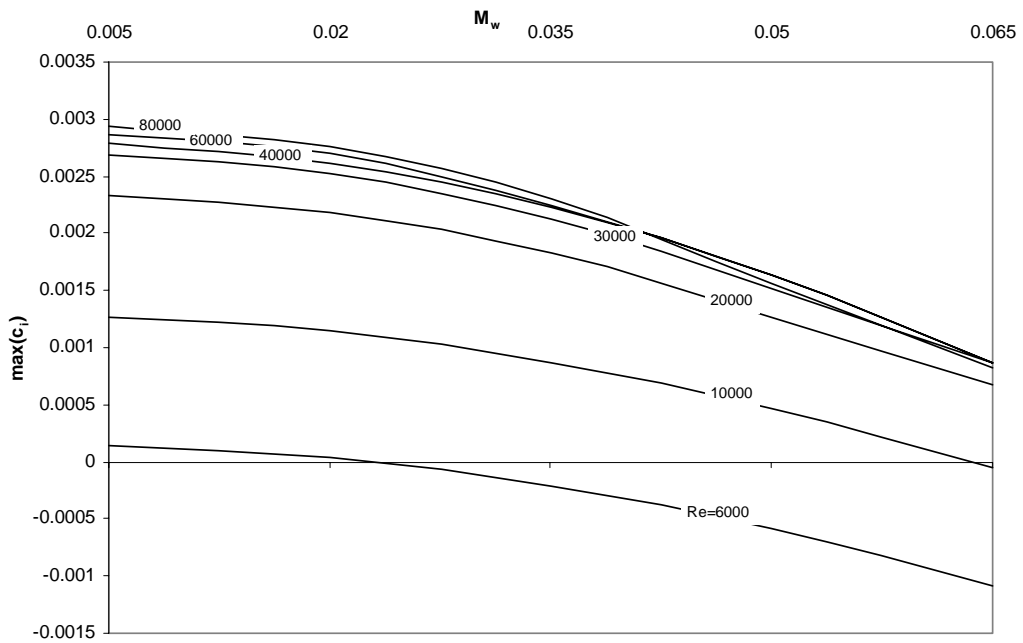

Figure 6.26. Maximum c_i of Mode 0 for different Mach numbers at fixed Reynolds numbers.

CHAPTER 7

CONCLUSIONS

In this study the linear viscous stability characteristics of high speed Couette and combined Couette – Poiseuille flows have been investigated numerically. A computer program was developed for the solution of the instability equations derived from compressible Navier – Stokes equations. The governing equations were discretized using a second order finite difference scheme resulting in a generalized eigenvalue problem for the temporal amplification factor. The temporal stability of the problem was analyzed to obtain the eigenvalue spectrum. The numerical method used was the global method which requires more grid points for improved accuracy, and validation was achieved by comparing the results of plane hypersonic Couette flow with that of Malik [14] and Hu and Zhong [17]. The effects of viscosity, temperature, density and compressibility on the stability of Modes I and II for Couette flow, and Mode 0 for Couette – Poiseuille flow were studied. It was seen that viscosity plays a destabilizing role in both Mode I and Mode II instability for supersonic Couette flow for a range of Reynolds number and wavenumbers. Both of these modes originate from the wave reflections in a supersonic region near the upper or lower wall.

Mode I and Mode II, in general, are the most unstable modes for supersonic plane Couette flow. But they were not dominant in the combined plane Couette – Poiseuille flow and the new mode which seemed to be a member of even modes such as Mode II was the most unstable mode and was labeled as Mode 0. As for the Mach number effects, Mode 0 was destabilized first and then stabilized as Mach number

increased. The range of Mach numbers which has Mode 0 instability expanded with Reynolds number but remained finite. In general, the stability of the bounded plane Coutte – Poiseuille flow was different from that of the unbounded high speed boundary layers in many aspects due to the presence of the upper wall.

Although z – momentum equation was solved together with the set of equations for stability analysis for plane Couette flow, the same equation was not included for plane combined Couette – Poiseuille flow stability analysis to economize the computational effort. Two-dimensional linear stability eigenvalue spectrum contained less modes than three-dimensional spectra but the most unstable eigenmode, Mode 0, for two dimensional stability was numerically the same for plane Couette – Poiseuille flow with that of three dimensional.

The results were presented using the boundary condition of $\hat{T}(0) = 0$ in computation instead of $\dfrac{d\hat{T}}{dy}(0) = 0$ for the temperature fluctuation at the lower wall even when the basic flow was adiabatic. The use of $\hat{T}(0) = 0$ instead of $\dfrac{d\hat{T}}{dy}(0) = 0$ did not make a significant difference on the results when compared to Hu and Zhong [17].

The critical Reynolds number was found to be Re_{cr} = 5718.338 for M_w = 0.0001 using 249 interior grid points for combined plane Couette – Poiseuille flow. This correspond to the fully Poiseuille case, as the Couette component is negligibly small. That means the flow is uncondionally stable for the Reynolds number less than Re_{cr} regardless of Mach number. The effect of the number of grid points used on the critical Reynolds number after 249 grids was not noteworthy and neutral stability contours calculated using that number of nodes. Orszag [24] found the critical Reynolds number as Re_{cr} = 5772.22 for instability of incompressible viscous plane Poiseuille flow using the Chebyshev method.

Both the Reynolds number and the upper wall Mach numbers draw the boundaries for the instability analysis of the flow through the piston ring end gap. Although Reynolds number and wall Mach number in the piston ring end gap were calculated as $Re = 5000$ and $M_w = 0.0235$ for plane Couette – Poiseuille flow, the flow was investigated and stability contours were determined for a range of wall Mach numbers, $M_w \leq 0.065$, and a range of Reynolds numbers, $Re = 5000 - 100000$ extending the investigation to get more about the behavior of the flow. If the upper wall Mach number increases more than $M_w > 0.065$, Reynolds numbers jump to high values. While the Reynolds number is 15000 for $M_w = 0.065$, that value jumped to $35x10^6$ for $M_w = 0.01$. It was difficult to explain physically the current situation of Reynolds number jump for that small increase of Mach number. The reasons would be the physics of the problem studied and most probably the solution method and more grid requirement for improved solution and better accuracy. At the range of Mach numbers between 0.065 and 0.3, there was a complex trend of Reynolds numbers. The number of grid points used in discretization did not make any difference on the dispersion of the Reynolds numbers on $M_w - Re$ map at a range of $0.065 < M_w < 0.3$ and the spectra of Reynolds number was unsteady to the grid points. For $M_w > 0.3$, behavior of the Reynolds numbers according to Mach numbers were much steady than the previous Mach number range.

The thin layer of oil film and on which gas layer was confined between two parallel plates simply represents the basic geometry of the problem. The thickness and the velocity of the oil film moving on the stationary plate were so small compared to the high-speed gas flow occurring above the oil film that the oil layer behaves like a solid wall and only the stability of gas phase was concerned. There was no expectation for the magnitude of the critical Reynolds number to be affected due to the omission of the oil layer in the analysis. This was confirmed by Özgen [3] who studied the characteristics of the instability of Newtonian and non-Newtonian fluid – air systems and concluded that for the air flowing over a thin layer of liquid, the effect of the thin layer was negligible on the two-phase flow instability.

REFERENCES

[1]   ''Backflow Oil Transfer in Internal Combustion Engines" A.Karkaç, M.S. Thesis, (2002), Department of Mechanical Engineering, METU

[2]   ''Experimental Investigation of Oil Accumulation in The Inter Ring Volumes in Internal Combustion Engines ,'' T.İçöz, M.S. Thesis,(2001), Department of Mechanical Engineering, METU

[3]   "Two-Layer Flow Stability in Newtonian and Non-Newtonian Fluids", S.Özgen, Ph/D. Thesis, Universite Libré De Bruxelles and Von Karman Institute for Fluid Dynamics,September (1999)

[4]   "Stability of the Compressible Laminar Boundary Layer", L.Lees, E. Reshotko, J. Fluid Mechanics, (1961), Vol.12, pp.555-591.

[5]   "On the Inviscid Stability of the Laminar Mixing of Two Parallel Streams of a Compressible Fluid" M. Lessen, J.A.Fox, H.M.Zien, J.Fluid Mechanics, (1965), Vol.23, No:2, pp.355-367.

[6]   "Stability of Compressible Boundary Layers", W.B.Brown, AIAA Journal, (1967), Vol.33, No:10, pp.1753-1759.

[7]   "Instability due to Viscosity Stratification", C.S.Yih, J. Fluid Mechanics, (1967), Vol.67, No:2, pp.337-352.

[8]   "Shear Layer Instability of an Inviscid Compressible Fluid. Part 2", W. Blumen, P.G.Drazin, D.F.Billings, J.Fluid Mechanics, (1975), Vol.71, No:2, pp.305-316

[9]   "Shear Layer Instability of an Inviscid Compressible Fluid", W.Blumen, J.Fluid Mechanics, (1970), Vol.40, No:4, pp.769-781.

[10]   "Linear Stability Theory and the Problem for Supersonic Boundary-Layer Transition", L.M.Mack, AIAA Journal, (1974), Vol.13, No:3, pp.278-289.

[11]   "Linear Stability Analysis of Nonhomentropic, Inviscidi Compressible Flows" V.D.Djordjevic, L.G.Redekopp, Physics of Fluids, (1988) Vol.31, No:11, pp.3239-3245.

[12]   "Two Linear Stability of Viscous Compressible Plane Couette Flow", W.Glatzel, J. Fluid Mechanics, (1989), Vol.202, pp.515-541.

[13]   "The Effects of Walls on a Spatially Growing Supersonic Shear Layer", M.Zhuang, P.E.Dimotakis, T.Kubota, Physics of Fluids, (1990), A 2 No:4, pp.599-604

[14]   "Numerical Methods for Hypersonic Boundary Layer Stability", M.R.Malik, J.Computational Physics, (1990),Vol.86, pp.376-413

[15]   "Wave Formation on a Liquid Layer for De-Icing Airplane Wings" C.S.Yih, J. Fluid Mechanics, (1990), Vol.76, No:2, pp.337-352.

[16]   "On The Linear Stability of Compressible Plane Couette Flow", P.M.Duck, G.Erlebacher, M.Y.Hussaini, J.Fluid Mechanics, (1994), Vol.258, pp.131-165

[17]   "Linear Stability of Viscous Supersonic Plane Couette Flow" S.Hu, X.Zhong, Physics of Fluids, (1998), Vol.10, No:3, pp.709-740

[18]   "Linear Growth in Two-Fluid Plane Poiseuille Flow", M.J.South, A.P.Hooper, J.Fluid Mechanics, (1999), Vol.381, pp.121-139.

[19]   "Two Fluid Boundary Layer Stability", S.Özgen, G.Degrez, G.S.R.Sarma, Physics of Fluids, (1998), Vol.10, No:11, pp. 2746-2757

[20]   "Computation of the Stability of the Laminar Compressible Boundary Layer", L.M.Mack,

[21]   "Stability of Parallel Flows", R.Betchov, W.O.Criminale, Academic Press, 1967.

[22]   "Boundary Layer Theory", H.Schlichting, McGraw-Hill Book Company, 1979.

[23]   "An Algorithm for Generalized Matrix Eigenvalue Problems"C.B.Moler and G.W.Stewart, SIAM J.Numer.Anal., (1973), Vol. 10 No.2 , pp. 241-256

[24]   "Accurate Solution of the Orr-Sommerfeld Equation", S.A.Orszag, J.Fluid Mechanics, (1971), Vol. 50, Part 4, pp.689-702

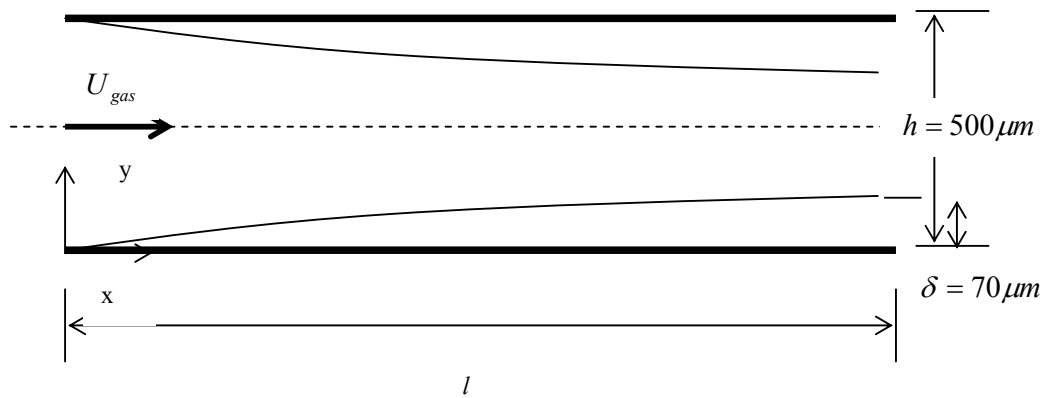# APPENDIX A

DEVELOPMENT OF FLOW IN A CHANNEL

Figure A.1. Basic flow representation of parallel flow

Figure A.1. shows developing Poiseuille flow in a channel for air as the fluid:

$$U_{gas} = 400 \text{ m/s}$$
$$x = l = 3 \text{x} 10^{-3} \text{ m}$$
$$h = 0.5 \text{x} 10^{-3} \text{ m}$$
$$v = 26.41 \text{x} 10^{-6} \text{ m}^2 / s$$
$$\text{at } T_{gas} = 400 \text{ K}$$

therefore

$$\text{Re}_x = \frac{U_\infty l}{v} = \frac{400 x 3 x 10^{-3}}{26.41 x 10^{-6}} = 45 * 10^3$$

which is laminar gas flow.

Boundary layer thickness for flow over flat plate for Re_x is

$$\frac{\delta}{x} \cong \frac{5}{\sqrt{Re_x}} \Rightarrow \delta \cong \frac{5x}{\sqrt{Re_x}} = \frac{5*3*10^{-3}}{\sqrt{45*10^3}} = 0.07071*10^{-3} m. \text{ or } \delta \cong 70 \ \mu m.$$

where

$$Re_{x,critical} = 3*10^5$$

At 500K gas velocity assuming perfect gas

$$U_{gas} = a = \sqrt{\gamma RT}$$

where

$$\gamma = 1.4$$
$$R = 287 \text{ J/kg.K}$$

For

$$T_{gas} = 500 \ K \ \ \nu = 36*10^{-6} \ m^2/s$$

$$U_{gas} = \sqrt{1.4*287*500} = 448.21 \text{ m/s} = 450 \text{ m/s}$$

$$Re_\infty = \frac{U_\infty l}{\nu} = \frac{450*3*10^{-3}}{36*10^{-6}} = 37.5*10^3 \ \langle \ 3*10^5$$

Therefore flow is laminar for the gas temperature of 500 K.

Convection time scale:

$$x = U_{gas}.t \Rightarrow t = \frac{x}{U_{gas}} = \frac{3*10^{-3}}{400} = 10^{-5} \sec \ \ t = 0.01 \text{ miliseconds}$$

Therefore, for the above condition, flow over the oil layer, gas flow is laminar and it takes about 0.01 millisecond for the flow fully develop in the channel.

APPENDIX B

VELOCITY AND TEMPERATURE PROFILES
IN PLANE POISEUILLE FLOW

B.1. General

For the case of compressible and viscous two-dimensional flow with constant properties the system of equations for the velocity and the temperature distribution in steady flow along $x - y$ plane, obtain from the equations in dimensional form:

Continuity:

$$(\frac{\partial \rho}{\partial t} + \frac{\partial(\rho u)}{\partial x} + \frac{\partial(\rho v)}{\partial y}) = 0 \tag{B.1}$$

$x -$ momentum:

$$\rho\left[\frac{\partial u}{\partial t} + u\frac{\partial u}{\partial x} + v\frac{\partial u}{\partial y} + w\frac{\partial u}{\partial z}\right] =$$
$$-\frac{\partial P}{\partial x} + \frac{\partial}{\partial x}\left[\mu(2\frac{\partial u}{\partial x} - \frac{2}{3}(\frac{\partial u}{\partial x} + \frac{\partial v}{\partial y} + \frac{\partial w}{\partial z}))\right] + \frac{\partial}{\partial y}\left[\mu(\frac{\partial v}{\partial x} + \frac{\partial u}{\partial y})\right] + \frac{\partial}{\partial z}\left[\mu(\frac{\partial w}{\partial x} + \frac{\partial u}{\partial z})\right] \tag{B.2}$$

$y -$ momentum:

$$\rho\left[\frac{\partial v}{\partial t} + u\frac{\partial v}{\partial x} + v\frac{\partial v}{\partial y} + w\frac{\partial v}{\partial z}\right] =$$
$$-\frac{\partial P}{\partial y} + \frac{\partial}{\partial x}\left[\mu(\frac{\partial v}{\partial x} + \frac{\partial u}{\partial y})\right] + \frac{\partial}{\partial y}\left[\mu(2\frac{\partial v}{\partial y} - \frac{2}{3}(\frac{\partial u}{\partial x} + \frac{\partial v}{\partial y} + \frac{\partial w}{\partial z}))\right] + \frac{\partial}{\partial z}\left[\mu(\frac{\partial w}{\partial y} + \frac{\partial v}{\partial z})\right] \tag{B.3}$$

energy :

$$\rho c_p \left[\frac{\partial T}{\partial t} + u \frac{\partial T}{\partial x} + v \frac{\partial T}{\partial y} + w \frac{\partial T}{\partial z} \right] =$$

$$\frac{\partial}{\partial x}(k\frac{\partial T}{\partial x}) + \frac{\partial}{\partial y}(k\frac{\partial T}{\partial y}) + \frac{\partial}{\partial z}(k\frac{\partial T}{\partial z}) + \frac{\partial P}{\partial t} + u\frac{\partial P}{\partial x} + v\frac{\partial P}{\partial y} + w\frac{\partial P}{\partial z} + \Phi$$

(B.4)

where

$$\Phi = 2\mu \left[(\frac{\partial u}{\partial x})^2 + (\frac{\partial v}{\partial y})^2 + (\frac{\partial w}{\partial z})^2 + \frac{1}{2}(\frac{\partial v}{\partial x} + \frac{\partial u}{\partial y})^2 + \frac{1}{2}(\frac{\partial w}{\partial y} + \frac{\partial v}{\partial z})^2 + \frac{1}{2}(\frac{\partial u}{\partial z} + \frac{\partial w}{\partial x})^2 - \frac{1}{3}(\nabla.V) \right]$$

assuming:

$u=u(y)$, $v=0$, $T=T(y)$ (also $T=T(u)$), $P=P(x)$, $\frac{dP}{dx} = cons\tan t$, $\frac{dP}{dy} = 0$

c_p=constant, $\mu = \mu(T)$, $k = k(T)$, $\Pr = \mu c_p / k$

Simplifying both x – momentum and energy equations, one can get the fictitious equality to the unsteady velocity and temperature terms to solve the coupled equations using explicit finite difference method.

In reality both $\frac{du}{dt} = \frac{u_j^{k+1} - u_j^k}{\Delta t}$ and $\frac{dT}{dt} = \frac{T_j^{k+1} - T_j^k}{\Delta t}$ are equal to zero and this feature is used for explicit formulation of the equations.

B.1.1. x – Momentum Equation:

$$\frac{du}{dt} = -\frac{1}{\gamma M_w^2}\frac{dP}{dx} + \frac{1}{Re}\frac{\partial}{\partial y}(\mu\frac{\partial u}{\partial y})$$

(B.5)

$$\frac{du}{dt} = -\frac{1}{\gamma M_w^2}\frac{dP}{dx} + \frac{1}{Re}\frac{\partial \mu}{\partial y}\frac{\partial u}{\partial y} + \frac{1}{Re}(\mu(\frac{\partial^2 u}{\partial y^2}))$$

(B.6)

110

$$\frac{u_i^{j+1} - u_i^j}{\Delta t} = -\frac{1}{\gamma M_w^2}\frac{dP}{dx} + \frac{1}{Re}\frac{\mu_i^j - \mu_{i-1}^j}{\Delta y}\frac{u_i^j - u_{i-1}^j}{\Delta y} + \frac{1}{Re}(\mu_i^j(\frac{u_{i+1}^j - 2u_i^j + u_{i-1}^j}{(\Delta y)^2})) \quad \text{(B.7)}$$

$$u_i^{j+1} = u_i^j + \frac{\Delta t}{(\Delta y)^2}\left(\begin{array}{c} -\dfrac{1}{\gamma M_w^2}\dfrac{dP}{dx}(\Delta y)^2 + \dfrac{1}{Re}(\mu_i^j - \mu_{i-1}^j)(u_i^j - u_{i-1}^j) \\[2ex] + \dfrac{1}{Re}\mu_i^j(u_{i+1}^j - 2u_i^j + u_{i-1}^j) \end{array} \right) \quad \text{(B.8)}$$

B.1.2. Energy Equation:

$$\frac{dT}{dt} = \frac{(\gamma-1)}{\gamma}u\frac{dP}{dx} + \frac{1}{Re\,Pr}\frac{\partial}{\partial y}(k\frac{\partial T}{\partial y}) + \frac{(\gamma-1)}{Re}M_w^2\mu(\frac{\partial u}{\partial y})^2 \quad \text{(B.9)}$$

$$\frac{dT}{dt} = \frac{(\gamma-1)}{\gamma}u\frac{dP}{dx} + \frac{1}{Re\,Pr}(\frac{\partial k}{\partial y}\frac{\partial T}{\partial y} + k\frac{\partial^2 T}{\partial y^2}) + \frac{(\gamma-1)}{Re}M_w^2\mu(\frac{\partial u}{\partial y})^2 \quad \text{(B.10)}$$

$$\frac{dT}{dt} = \frac{(\gamma-1)}{\gamma}u\frac{dP}{dx} + \frac{1}{Re\,Pr}\frac{cp}{Pr}(\frac{\partial \mu}{\partial y}\frac{\partial T}{\partial y} + \mu\frac{\partial^2 T}{\partial y^2}) + \frac{(\gamma-1)}{Re}M_w^2\mu(\frac{\partial u}{\partial y})^2 \quad \text{(B.11)}$$

$$\frac{T_i^{j+1} - T_i^j}{\Delta t} = \frac{(\gamma-1)}{\gamma}\frac{dP}{dx}u_i^j + \frac{1}{Re\,Pr}\frac{cp}{Pr}(\frac{\mu_{i+1}^j - \mu_i^j}{\Delta y}\frac{T_{i+1}^j - T_i^j}{\Delta y})$$
$$+ \mu_i^j\frac{T_{i+1}^j - 2T_i^j + T_{i-1}^j}{(\Delta y)^2}) + \frac{(\gamma-1)}{Re}M_w^2\mu_i^j(\frac{u_{i+1}^j - u_i^j}{\Delta y})^2 \quad \text{(B.12)}$$

$$T_i^{j+1} = T_i^j + \frac{\Delta t}{(\Delta y)^2}\left(\begin{array}{c} \dfrac{(\gamma-1)}{\gamma}\dfrac{dP}{dx}(\Delta y)^2 u_i^j \\[2ex] + \dfrac{1}{Re\,Pr}\dfrac{cp}{Pr}(\mu_{i+1}^j - \mu_i^j)(T_{i+1}^j - T_i^j) \\[2ex] + \dfrac{1}{Re\,Pr}\dfrac{cp}{Pr}\mu_i^j(T_{i+1}^j - 2T_i^j + T_{i-1}^j) \\[2ex] + \dfrac{(\gamma-1)}{Re}M_w^2\mu_i^j(u_{i+1}^j - u_i^j)^2 \end{array} \right) \quad \text{(B.13)}$$

B.1.3. Sutherland's Viscosity Law:

Viscosity is a function of temperature from Sutherland's law and temperature is also a function of velocity which is to be solved simultaneously.

$$\frac{\mu_i^j}{\mu_\infty} = (\frac{T_i^j}{T_\infty})^{3/2} \left(\frac{\frac{T_\infty}{T_\infty} + \frac{S_1}{T_\infty}}{\frac{T_i^j}{T_\infty} + \frac{S_1}{T_\infty}} \right) = (\frac{T_i^j}{T_\infty})^{3/2} \left(\frac{1 + \frac{S_1}{T_\infty}}{\frac{T_i^j}{T_\infty} + \frac{S_1}{T_\infty}} \right) \qquad \text{(B.14)}$$

or in dimensionless form

$$\mu_i^j = (T_i^j)^{3/2} \left(\frac{1 + \frac{S_1}{T_\infty}}{T_i^j + \frac{S_1}{T_\infty}} \right) \quad S_1 = 110K \qquad \text{(B.15)}$$

B.1.4. Boundary & Initial Conditions:

For the initial velocity and temperature profile for the explicit solution of the coupled equations linear velocity profile is taken as starting profile.

$$u(y) = \frac{y}{h} U_\infty \quad \& \quad T(y) = T_w - y \frac{(T_w - T_\infty)}{h} \qquad \text{(B.16)}$$

Since the method is explicit the following inequality must hold for the numerical stability, assuming $\text{Pr} < 1$, that is, a gas:

$$1 - 2 \frac{\Delta t}{\Delta y^2} \frac{\mu_i^j}{\rho_i^j} \frac{1}{\text{Re}\,\text{Pr}} \frac{c_p}{\text{Pr}} \geq 0 \qquad \text{(B.17)}$$

this parameter should be monitored during the computation.

APPENDIX C

COEFFICIENT MATRICES OF GENERALIZED EIGENVALUE PROBLEM

$$B_{11} = (\frac{1}{\mu}\frac{d\mu}{dT}\frac{dT}{dy})$$

$$B_{12} = (i\alpha)l_1$$

$$B_{13} = 0$$

$$B_{14} = (\frac{1}{\mu}\frac{d\mu}{dT}\frac{d^2u}{dy^2} + \frac{1}{\mu}\frac{d\mu}{dT}\frac{du}{dy})$$

$$B_{15} = 0$$

$$B_{21} = (i\alpha)l_1$$

$$B_{22} = \frac{1}{\mu}\frac{d\mu}{dT}\frac{dT}{dy}l_2$$

$$B_{23} = -\frac{Re}{\mu}\frac{1}{l}$$

$$B_{24} = 0$$

$$B_{25} = i\beta$$

$$B_{31} = 0$$

$$B_{32} = (i\beta)l_1$$

$$B_{33} = 0$$

$$B_{34} = \frac{1}{\mu}\frac{d\mu}{dT}\frac{dw}{dy}$$

$$B_{35} = \frac{1}{\mu}\frac{d\mu}{dT}\frac{dT}{dy}$$

$$B_{41} = 0$$

$$B_{42} = \frac{1}{T}$$

$$B_{43} = B_{44} = B_{45} = 0$$

$$B_{51} = 2(\gamma - 1)M^2 \frac{\mu \operatorname{Pr}}{k}\frac{du}{dy}$$

$$B_{52} = B_{53} = 0$$

$$B_{54} = 2\frac{1}{k}\frac{dk}{dT}\frac{dT}{dy}$$

$$B_{55} = 2\frac{\operatorname{Re}\operatorname{Pr}}{k}\frac{dw}{dy}$$

$$C_{11} = -\frac{\mathrm{Re}}{\mu}\frac{1}{T}(-i\varpi + i\alpha u + i\beta w) + (i\alpha)^2 l_2 + (i\beta)^2$$

$$C_{12} = -\frac{\mathrm{Re}}{\mu}\frac{1}{T}u' + \frac{1}{\mu}\frac{dT}{dy}(i\alpha)$$

$$C_{13} = -\frac{\mathrm{Re}}{\mu}(i\alpha)$$

$$C_{14} = \frac{1}{\mu}\frac{d\mu}{dT}\frac{d\,u}{dy} + \frac{1}{\mu}\frac{d^2\mu}{dT^2}\frac{dT}{dy}\frac{du}{dy}$$

$$C_{15} = (i\alpha)(i\beta)$$

$$C_{21} = \frac{l_0}{l_2}\frac{1}{\mu}\frac{d\mu}{dT}\frac{dT}{dy}(i\alpha)$$

$$C_{22} = -\frac{\mathrm{Re}}{\mu}\frac{1}{l_2}\frac{1}{T}(-i\varpi + (i\alpha)u + (i\beta)w) + (i\alpha)^2 + (i\beta)^2$$

$$C_{23} = 0$$

$$C_{24} = \frac{1}{l_2} - \frac{1}{\mu}\frac{d\mu}{dT}\frac{du}{dy}(i\alpha) + \frac{1}{l_2}\frac{1}{\mu}\frac{d\mu}{dT}\frac{dw}{dy}(i\beta)$$

$$C_{25} = \frac{1}{l_2}\frac{1}{\mu}\frac{d\mu}{dT}\frac{dT}{dy}(i\beta)$$

$$C_{31} = (i\alpha)(i\beta)l_1$$

$$C_{32} = -\frac{\mathrm{Re}}{\mu}\frac{1}{T}\frac{\partial w}{\partial y} + \frac{1}{\mu}\frac{d\mu}{dT}\frac{dT}{dy}(i\beta)$$

$$C_{33} = -(i\beta)\frac{\mathrm{Re}}{\mu}$$

$$C_{34} = \frac{1}{\mu}\frac{d\mu}{dT}\frac{d^2w}{dy^2} + \frac{1}{\mu}\frac{d^2\mu}{dT^2}\frac{dT}{dy}\frac{dw}{dy}$$

$$C_{35} = -\frac{\mathrm{Re}}{\mu}\frac{1}{T}(-i\varpi + (i\alpha)u + (i\beta)w + l_2(i\beta)^2 + (i\alpha)^2$$

$$C_{41} = \frac{1}{T}(i\alpha)$$

$$C_{42} = -\frac{1}{T^2}\frac{dT}{dy}$$

$$C_{43} = \frac{\gamma M^2}{T}(-i\varpi) + u\frac{\gamma M^2}{T}(i\alpha) + w\frac{\gamma M^2}{T}(i\beta)$$

$$C_{44} = -\frac{1}{T^2}(-i\varpi) - \frac{u}{T^2}(i\alpha) - \frac{w}{T^2}(i\beta)$$

$$C_{45} = \frac{1}{T}(i\beta)$$

$$C_{51} = 0$$

$$C_{52} = -\frac{\mathrm{Re}\,\mathrm{Pr}}{k}(\frac{1}{T}\frac{\partial T}{\partial y} - (\gamma-1)M^2\frac{\mu}{\mathrm{Re}}(i\alpha) - 2\frac{dw}{dy}(i\beta))$$

$$C_{53} = C_{54} = 0$$

$$C_{54} = -\frac{\mathrm{Re}\,\mathrm{Pr}}{k}\frac{1}{T}(-i\varpi + u(i\alpha) + w(i\beta)) + \left[(i\alpha)^{2+} + (i\beta)^2 + \frac{1}{k}\frac{dk}{dT}\frac{d^2T}{dy^2} + \frac{1}{k}\frac{d^2k}{dT^2}(\frac{dT}{dy})^2\right]$$

APPENDIX D

EIGENVALUE SPECTRA
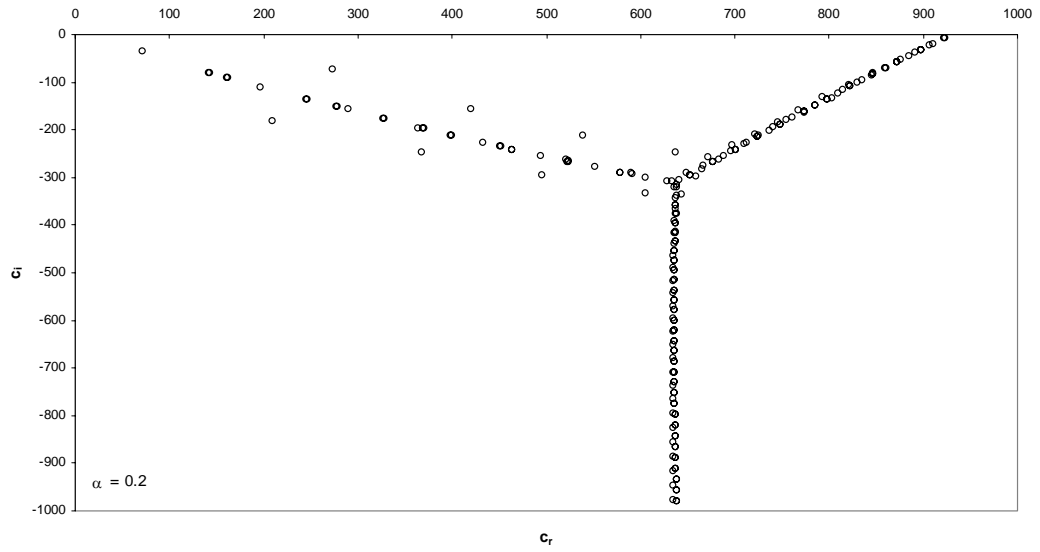
Figure D.1. Eigenvalue spectra for $M_w = 0.001$ at Re $=125000$ for $\alpha =0.2$
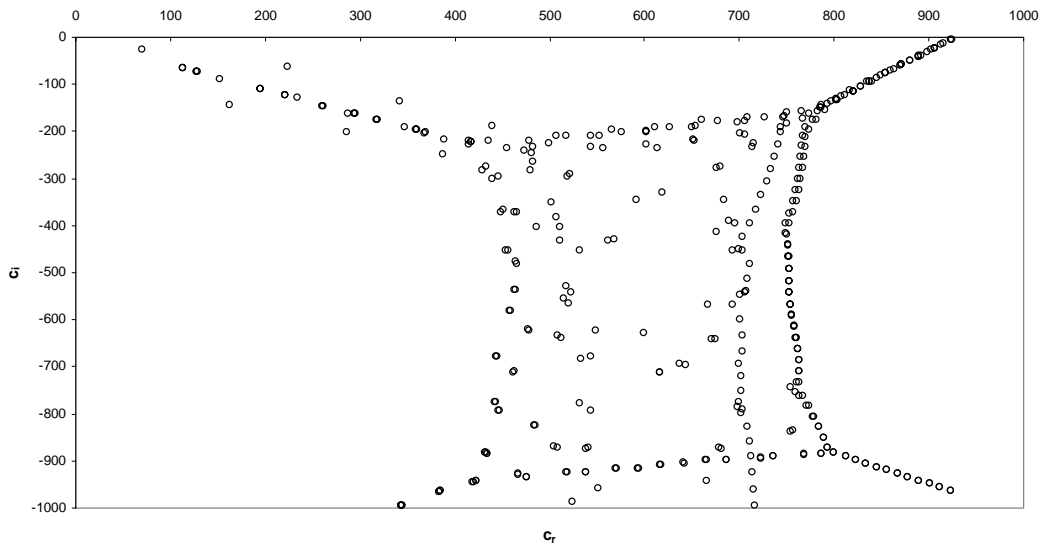
Figure D.2. Eigenvalue spectra for $M_w = 0.001$ at Re $=125000$ for $\alpha =0.4$
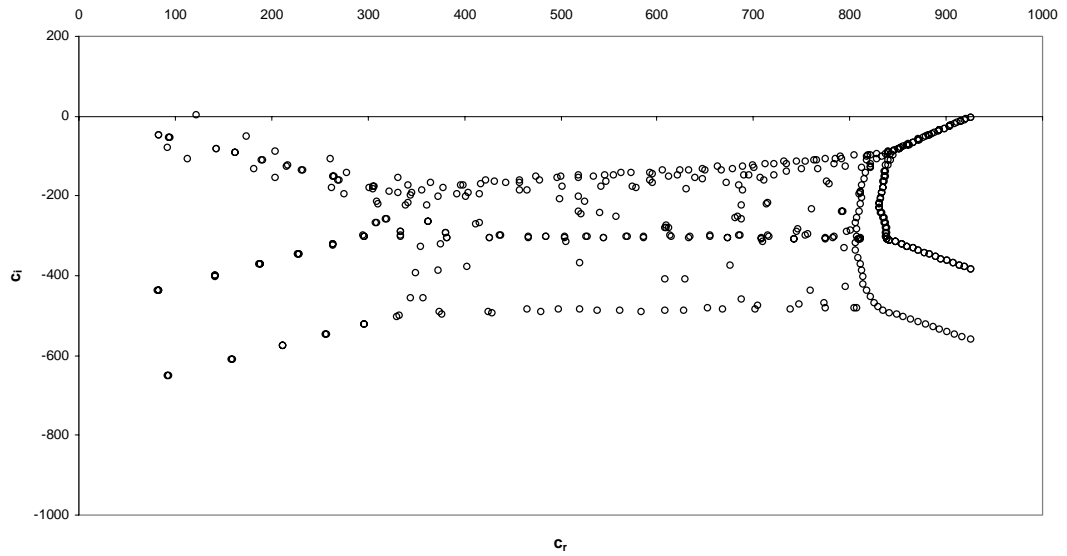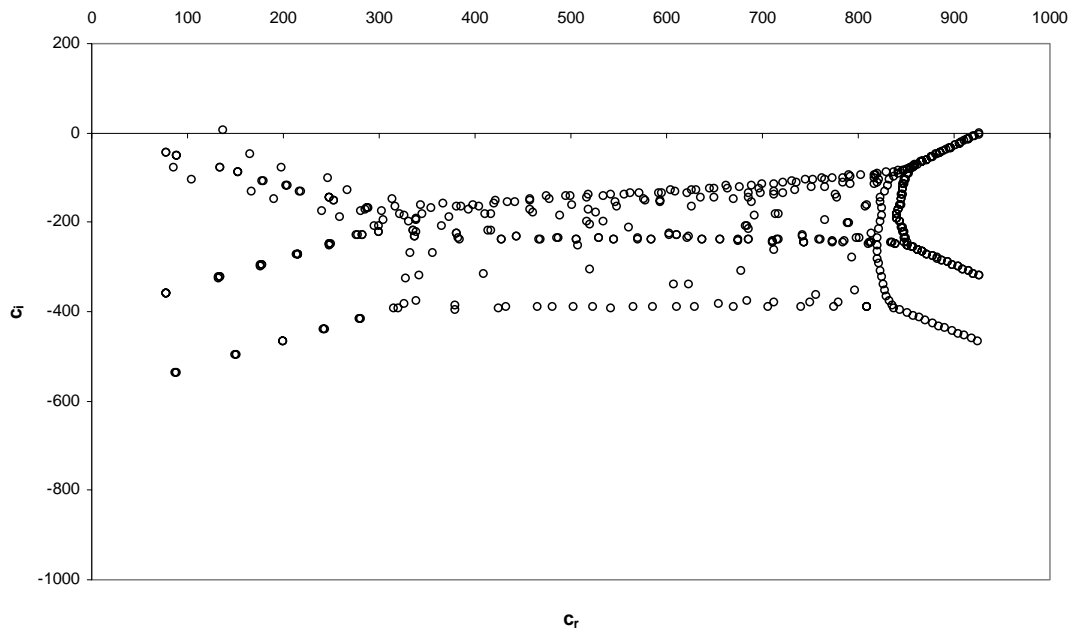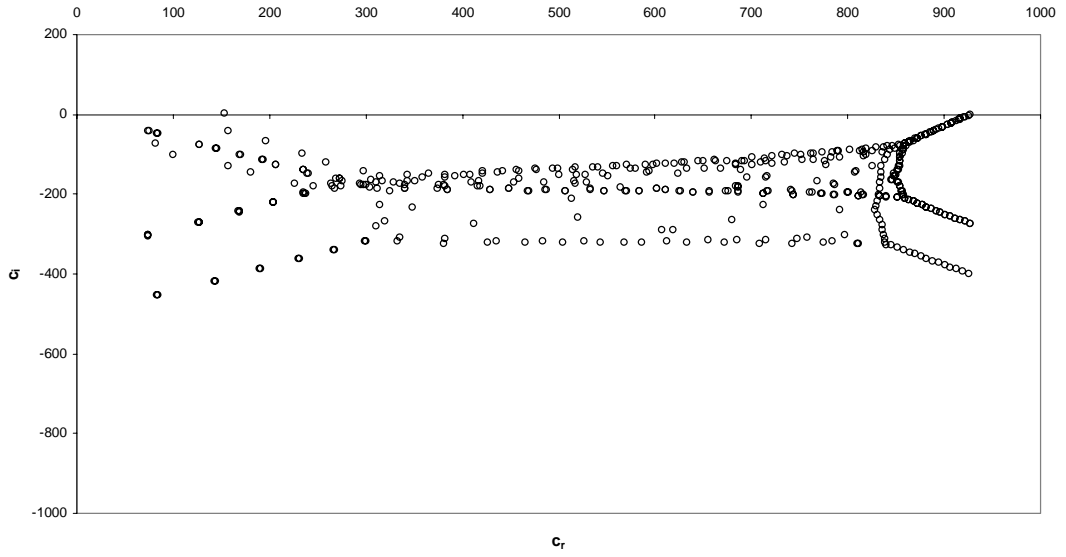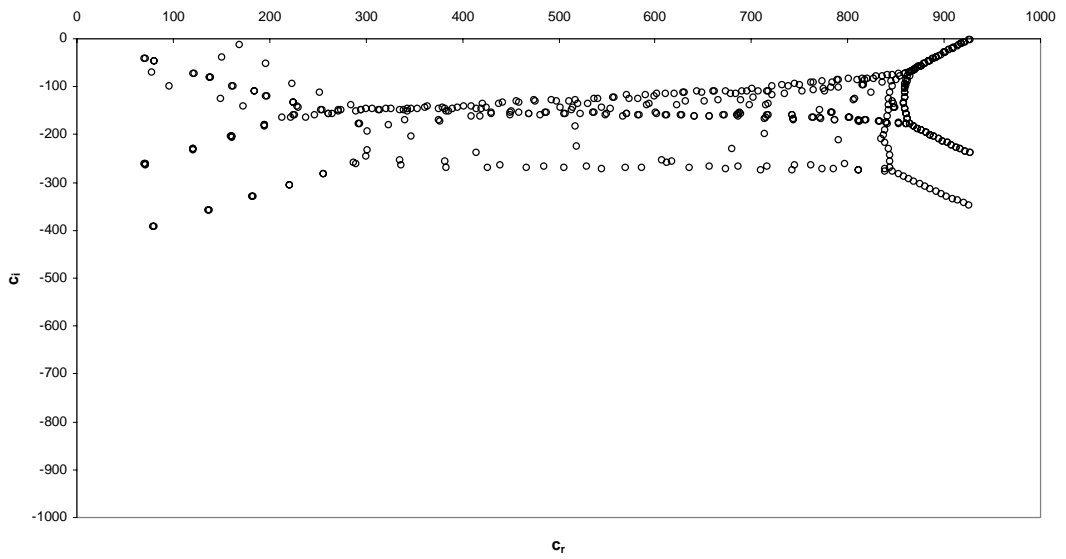
117
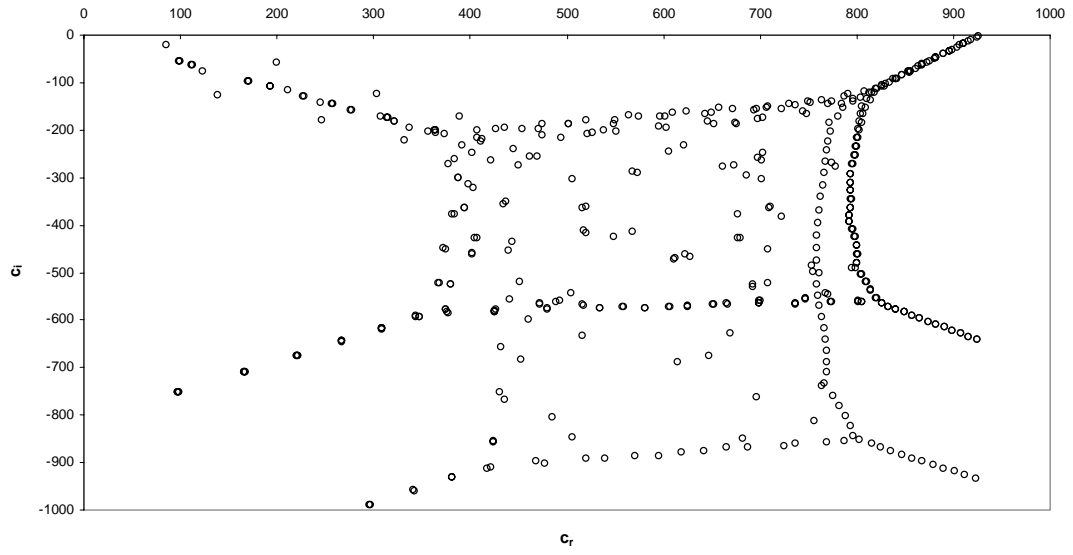
Figure D.3. Eigenvalue spectra for $M_w = 0.001$ at Re $= 125000$ for $\alpha = 0.6$
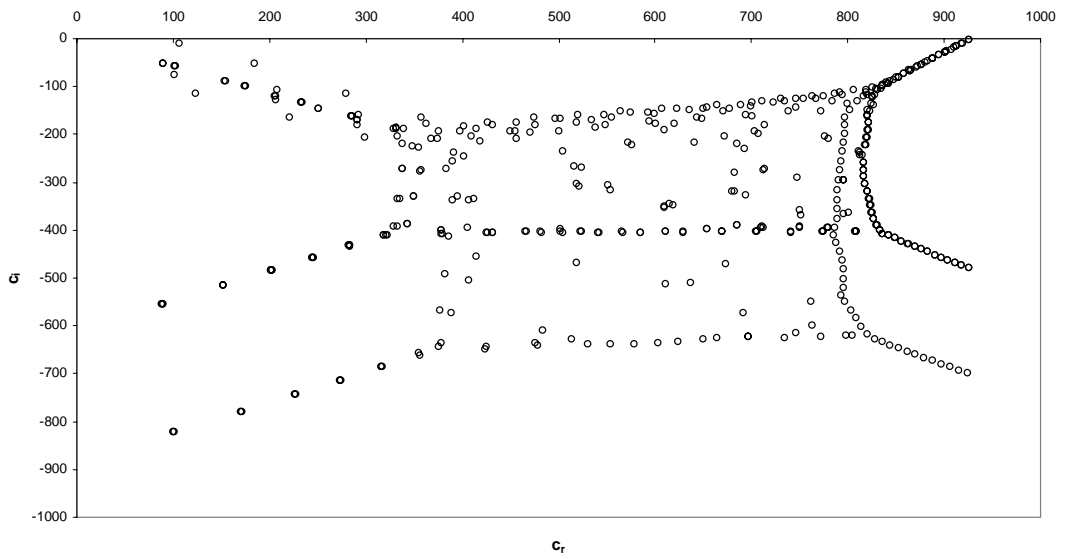
Figure D.4. Eigenvalue spectra for $M_w = 0.001$ at Re $= 125000$ for $\alpha = 0.8$

118

Figure D.5. Eigenvalue spectra for $M_w = 0.001$ at Re $=125000$ for $\alpha = 1.0$

Figure D.6. Eigenvalue spectra for $M_w = 0.001$ at Re $=125000$ for $\alpha = 1.2$
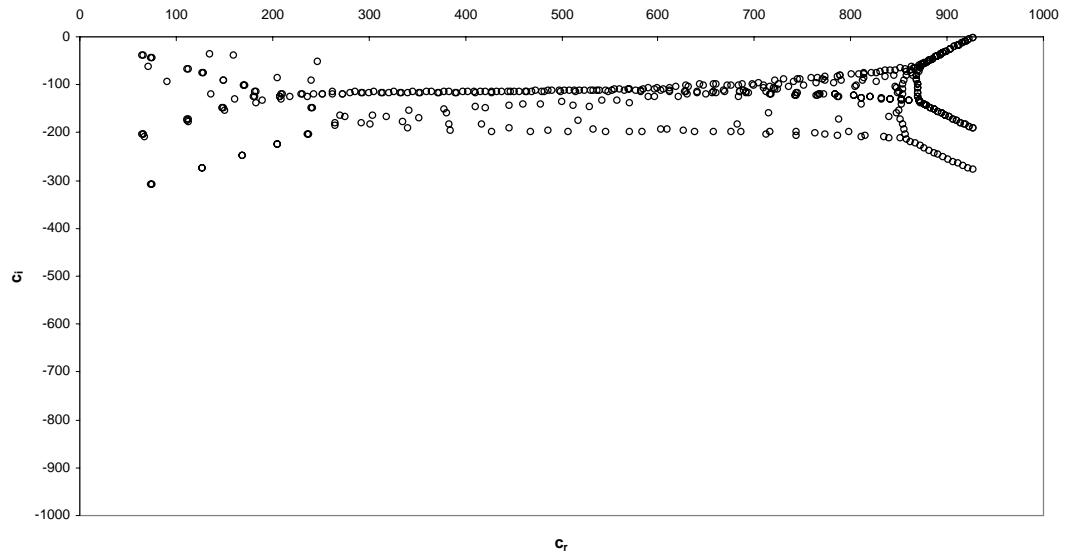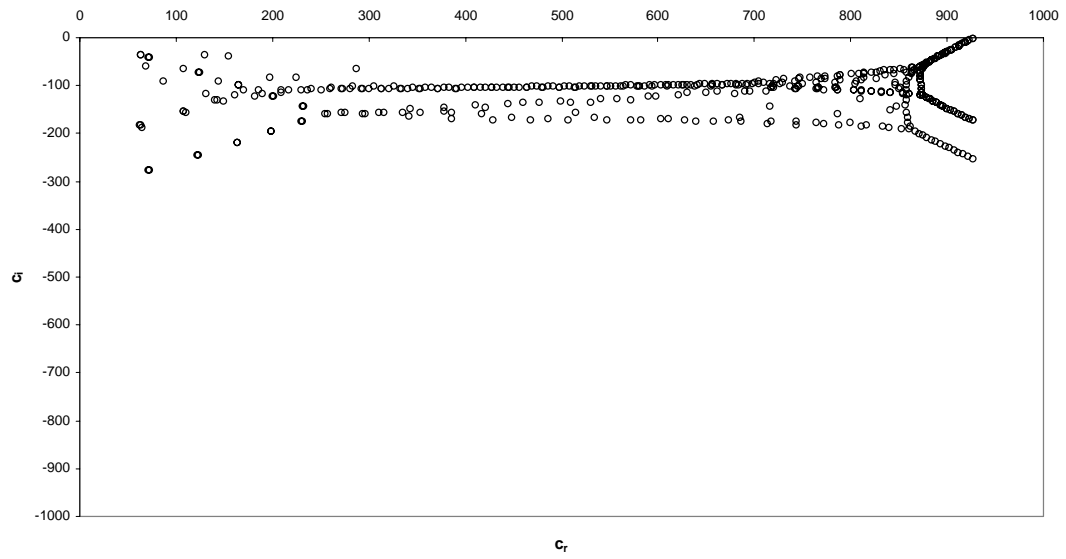
Figure D.7. Eigenvalue spectra for $M_w = 0.001$ at Re $=125000$ for $\alpha =1.4$

Figure D.8. Eigenvalue spectra for $M_w = 0.001$ at Re $=125000$ for $\alpha =1.6$

Figure D.9. Eigenvalue spectra for $M_w = 0.001$ at Re $=125000$ for $\alpha = 1.8$

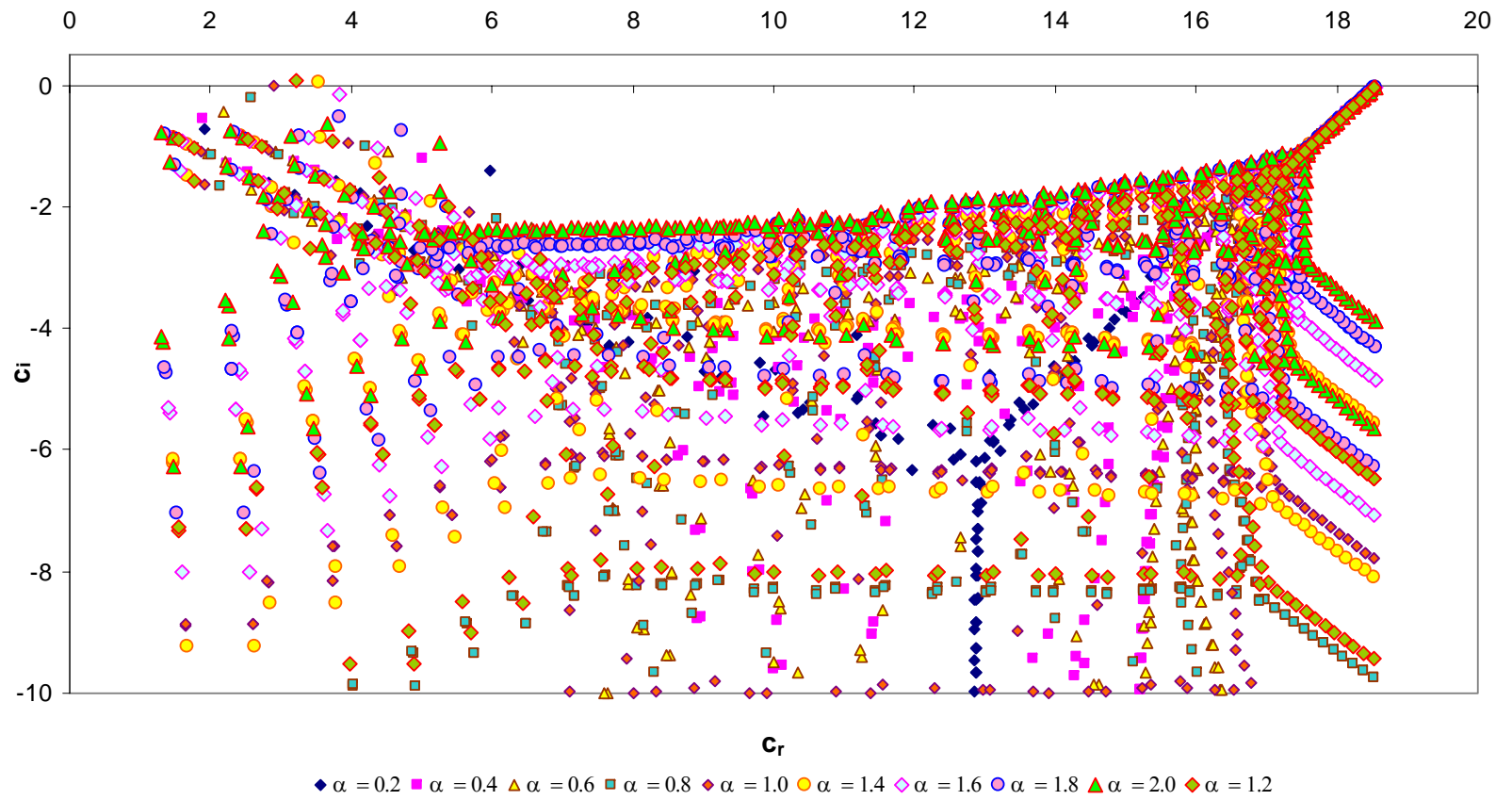Figure D.10. Eigenvalue spectra for $M_w = 0.001$ at Re $=125000$ for $\alpha = 2.0$

Figure D. 11 Eigenvalue spectra for $M_w = 0.001$ at Re=125000 for α=0.2 – 2.0

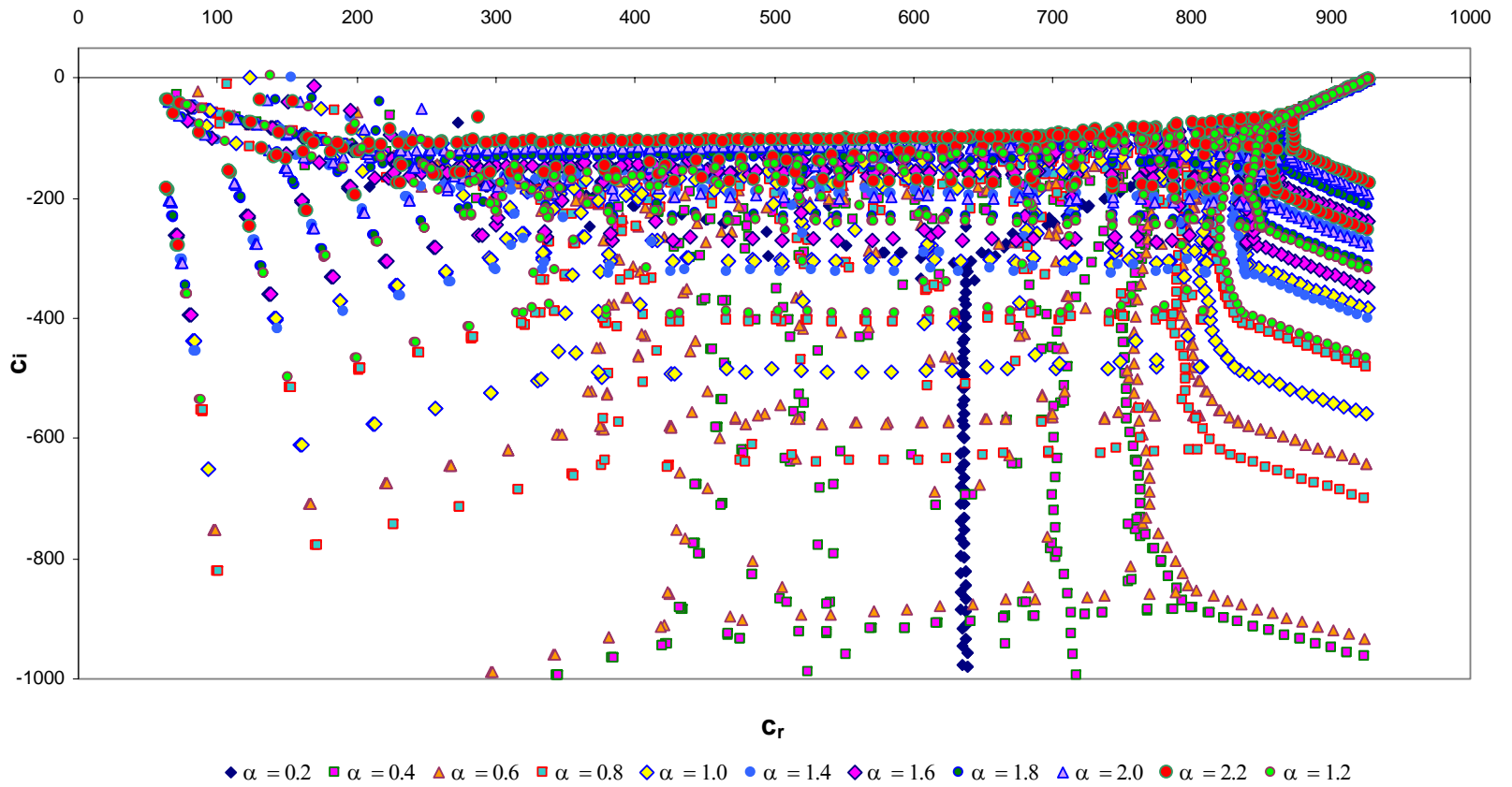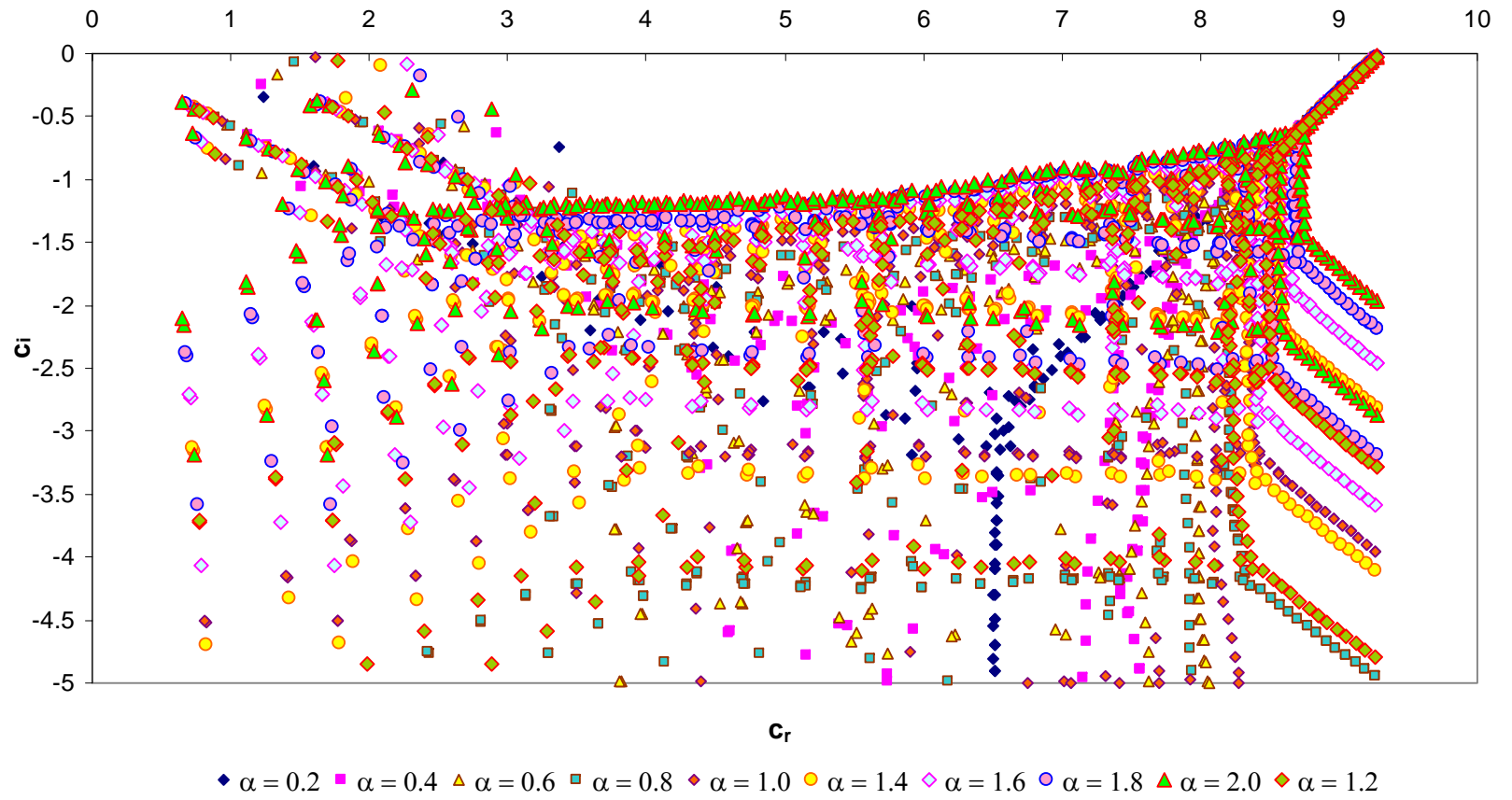Figure D. 12 Eigenvalue spectra for $M_w = 0.05$ at Re=125000 for α=0.2 – 2.0

Figure D. 13 Eigenvalue spectra for $M_w = 0.1$ at Re=125000 for α=0.2 – 2.0

124

VITA

Ali Aslan Ebrinç was born in Tavas, Denizli on December 27, 1969. He received his B.S. degree in Mechanical Engineering Department from the Middle East Technical University in September 1992. He worked as research and teaching assistant at Mechanical Engineering Department for 4 years and during this time he received his M.S. degree in Mechanical Engineering Department from the Middle East Technical University. The topic of thesis work was heat pipe application to parabolic solar collectors. He started graduate study for Doctor of Philosophy at 1996. He worked in Aselsan at Ankara as a product development engineer for electro-optic devices between the years 1996-1997 and after military service at 1998 he started working in Ford Otosan. He is already working in Ford Otosan as product development engineer for heavy duty diesel engine development project. His main areas of interest are HVAC-R, design, development and analysis of internal combustion engines and systems.